Surveys of Young Stars: Variability and Binarity

Marcelo Medeiros Guimarães

September 2008

MARCELO MEDEIROS GUIMARÃES

Surveys of Young Stars: Variability and Binarity

Tese apresentada à UNIVERSIDADE FEDERAL DE MINAS GERAIS
como requisito parcial para obtenção do grau de DOUTOR EM FÍSICA

Orientador: Prof. Luiz Paulo Ribeiro Vaz
Co-orientador: Prof. Bo Reipurth

Departamento de Física - ICEx - UFMG

Setembro de 2008

Agradecimentos

A ciência exige dedicação exclusiva daquele que a estuda. Por vezes o cientista sai de seu laboratório e leva consigo os problemas que ainda teimam em não ser solucionados. Dorme pensando neles, algumas vezes esses problemas são resolvidos em sonhos, outras vezes eles requerem anos de intenso e árduo trabalho. Por isso é necessário ter paixão pelo que se faz. Por isso fazemos ciência, porque depois de longas horas, às vezes dias, semanas, o resultado nos salta aos olhos e um sorriso nos vem ao rosto.

Eu tive a sorte de ter trabalhado, durante o meu doutorado, com dois exemplos claros de dedicação à ciência. Luiz Paulo e Bo, cada um à sua maneira, dedicam suas carreiras em prol do avanço da ciência. Com Luiz Paulo aprendi a ter muito cuidado com os detalhes do trabalho. Sempre ter certeza de como as coisas funcionam, nunca confiar em "caixas pretas". Bo me mostrou o lado apaixonante da ciência, me mostrou que é necessário ter força de vontade para seguir em frente. Espero ter aprendido o suficiente com eles para poder também fazer contribuições relevantes para o avanço da astronomia. Sou muito grato a eles por tudo que me ensinaram e por seus exemplos.

Uma vida dedicada à ciência requer sacrifícios, que seriam muito piores não fosse o apoio constante da família, da namorada e dos amigos. Felizmente sempre recebi muito apoio das pessoas a minha volta e sou muito grato a vocês por todo o amor, carinho, atenção, amizade e respeito. Muitas pessoas passaram pela minha vida ao longo desses anos, algumas partiram, outras ficaram, mas todas deixaram marcas que me fazem o que sou hoje. A todas elas, muito obrigado.

Só com sacrifício não se faz ciência, é necessário financiamento. Agradeço às agências financiadoras, CNPq e Capes, pelas bolsas de doutorado e doutorado sanduíche, que me permitiram realizar essa tese. Agradeço novamente ao meu co-orientador, Bo, pelo financiamento que me permitiu passar um ano trabalhando ao seu lado no Havaí e por ter me fornecido as observações que são essenciais para essa tese. Também agradeço Andy Adamson por coordenar as observações com o UKIRT e pelo seu apoio incansável a esse projeto.

Um longo caminho foi trilhado até aqui. Esse é um marco que separa duas etapas. Finalizo a primeira etapa com essa tese, que apesar de não ser capaz de conter todo o conhecimento adquirido ao longo desses anos, certamente exemplifica o que sou capaz de fazer. A segunda etapa se aproxima no horizonte, com boas expectativas.

Acknowledgements

Science demands exclusive dedication from those who study it. Many times the scientist leaves his laboratory and takes with him the problems that still insist not to be solved. He sleeps thinking about them, sometimes they are solved in his dreams, sometimes the problems require years of intense, hard work. That is why it is necessary to have passion for what one does. That is why we do science, because after long hours, sometimes days, weeks, the result jumps before our eyes and a smile comes to our face.

I was lucky I had the chance, during my PhD, to work with two clear examples of dedication to science. Luiz Paulo and Bo, each in his own way, dedicate their career to the development of science. I learned from Luiz Paulo to be careful about the details, to always be sure how things work and never trust "black boxes". Bo showed me the passionate side of science and how it is necessary to have will power to keep going. I hope a have learned enough with them to also be able to make relevant contributions to the development of astronomy. I am very grateful to them for all they have taught me and their examples.

A life dedicated to science requires sacrifices, which would be worst if it were not for the constant support of the family, girlfriend and friends. Fortunately I have always received much support from the people around me and I am very grateful to you all for all the love, care, attention, friendship and respect. A lot of people were part of my life along these years, some have gone by, others remained, but all of them left marks which made me what I am today. To all of you, thank you very much.

Only sacrifice does not do science, financial support is necessary. I thank the supporting agencies, CNPq and Capes, for the fellowships that allowed me to develop this thesis. I thank again my co-advisor, Bo, for his financial support which allowed me to spent one year working by his side in Hawaii and also for providing the observations which are essential for this thesis. I also thank Andy Adamson for coordinating the UKIRT observations and for his tireless support of this project.

I have come a long way until here. This is a mark that separates two periods. I end the first one with this thesis, which although it is not able to contain all the knowledge acquired along all these years, certainly examplifies what I am capable of doing. The second period approachs in the horizon, with good expectations.

Content

List of Figures

List of Tables

Resumo

Com o intuito de aumentar nosso conhecimento sobre estrelas jovens, realizamos três levantamentos de larga escala, em duas regiões de formação estelar, a Nebulosa de Órion e a associação de estrelas OB conhecida como Cygnus OB2.

O primeiro levantamento foi feito com a "Advanced Camera for Surveys - ACS" a bordo do telescópio espacial Hubble. Utilizamos um filtro estreito, centrado no comprimento de onda da linha Hα, para mapear a região ao redor do centro da Nebulosa de Órion. Nosso principal objetivo é utilizar a alta resolução da ACS ($0\farcs05$ por pixel) para detectar novos sistemas binários visuais. Estabelecemos limites para a separação entre as componentes dos sistemas binários ($0\farcs15$ até $1\farcs5$) utilizando testes de completeza da amostra e testes de probabilidade de projeção na linha de visada. Após um minucioso estudo de cada sistema detectado em nossa amostra, conseguimos atingir nosso objetivo e observamos indícios claros da evolução dinâmica desses sistemas binários na Nebulosa de Órion. Descobrimos 55 novos sistemas binários visuais em uma amostra de 72 sistemas binários e 3 sistemas triplos. Determinamos uma frequência de binárias de (8.8±1.1)% na Nebulosa de Órion, um valor 1.5 vezes menor do que para o campo estelar e 2.2 vezes menor do que em associações T. Esse já era um fato conhecido, mas baseado em estatísticas de poucos números, ao contrário dos nossos resultados, que foram obtidos com a utilização de uma amostra estatística mais significante. A razão entre o número de sistemas com separação grande e pequena aumenta significativamente a partir de $460''$ do centro do aglomerado, que é tomado como a estrela θ^1 Ori C. Esse fato, segundo nossa análise, é um indício da evolução dinâmica do aglomerado, que acontece através da destruição dos sistemas binários com grandes separações, após algumas passagens pelo poço de potencial gravitacional do centro do aglomerado. Um sub-produto da nossa análise é a detecção de candidatos a objetos sub-estelares (anãs marrons). Determinamos a natureza dupla do objeto COUP1061, classificado na literatura como uma anã marrom. Essa descoberta implica que o objeto COUP1061 é um sistema binário composto por duas anãs marrons, separados por aproximadamente 100 unidades astronômicas.

Os demais levantamentos foram feitos com a "Wide Field Camera" do "United Kingdom Infrared Telescope". Observamos a Nebulosa de Órion e Cygnus OB2, na região do infravermelho próximo, nas bandas J, H e K. O objetivo desses levantamentos fotométricos é determinar a população de estrelas variáveis dessas regiões de formação estelar. Através da utilização de índices estatísticos, as estrelas variáveis podem ser classificadas em seus diferentes grupos. Por se tratarem de levantamentos fotométricos de áreas grandes, desenvolvemos rotinas especiais para lidar com os catálogos, compostos por dezenas e algumas vezes centenas de milhares de objetos.

A Nebulosa de Órion foi observada por 101 noites, num intervalo de 178 dias. Foi feita uma exposição de 2 segundos por noite. Um longo processo de catalogação e calibração foi

necessário até se obter um conjunto de dados que pode ser utilizado para a busca de estrelas variáveis. Através da aplicação de índices estatísticos conseguimos descobrir novas candidatas a binárias eclipsantes e estrelas com variabilidade causada por pulsações ou por rotação. Um longo processo de análise é ainda necessário para exaurir a enorme quantidade de informação presente nesse levantamento.

A região de Cygnus OB2 foi observada por 112 noites, num intervalo de 217 dias. As observações seguiram o mesmo esquema usado no levantamento da Nebulosa de Órion, que consiste em uma exposição (com duração de 2 segundos) por noite. A análise preliminar dos dados para Cygnus OB2 nos permitiu descobrir 6 glóbulos cometários de pequena escala. Essa descoberta é uma forte evidência do processo de formação estelar recente nessa região. Também foi possível detectar 4 fontes infravermelhas, aparentemente jovens e que possivelmente estão localizadas no Braço Espiral de Perseu, muito mais distante do que a associação Cygnus OB2. Determinamos a natureza dupla da fonte infravermelha IRAS 20304+4059 que é classificada na literatura como possível proto-estrela.

Abstract

In the attempt of increasing our knowledge about young stars, we performed three large scale surveys of two star forming regions, namely the Orion Nebula and the young OB association known as Cygnus OB2.

The first survey was made with the Advanced Camera for Surveys (ACS) onboard the Hubble Space Telescope. We used a narrow band filter, centered in the wavelength of the Hα line, to map the region around the center of the Orion Nebula Cluster. Our main goal is to use the high resolution of the ACS ($0\farcs05$ per pixel) to detect new visual binaries. We set the separation limit between the components of the system ($0\farcs15$ to $1\farcs5$) using completeness tests and the probability of chance alignment. After a minute analysis of each system detected in our sample, we reached our goal and also observed clear evidence of the dynamical evolution of these systems in the Orion Nebula Cluster. We discovered 55 new visual binary systems within a total of 72 binaries and 3 triple systems. We determined a binary frequency of (8.8±1.1)% for the Orion Nebula Cluster, which is 1.5 times smaller than the frequency for the field and 2.2 times smaller than for the loose T associations. This was an already known fact but was based on small number statistics, while our results are based on more significant numbers. The ratio between wide and close binaries has a significant increase at $460''$ from the center of the cluster, assumed to be the star θ^1 Ori C. Our analysis indicates that this is clear evidence of the dynamical evolution of the Orion Nebula Cluster, which happens through the destruction of wide binaries, after few passages through the cluster's potential well. A byproduct of our survey is the detection of substellar candidates. We determined the double nature of the object known as COUP1061, which is classified in the literature as a brown dwarf. This finding implies that COUP1061 is a binary system where both components are brown dwarfs, separated by ∼100 AU.

In order to perform the second and third surveys we made use of the Wide Field Camera of the United Kingdom Infrared Telescope. We observed the Orion Nebula and Cygnus OB2 with near infrared filters, JHK. Our objective with these photometric surveys is to determine the population of variable stars in these star forming regions. Using statistical indices we can separate and classify the variable stars into different groups. Because these photometric surveys cover large areas in the sky we developed special routines to deal with the catalogs, which are composed of thousands and sometimes hundreds of thousands of objects.

The Orion Nebula was observed during 101 nights, covering 178 days. We performed short exposures (2 seconds long) once each night. Long cataloging and calibration processes were necessary until a satisfying dataset was ready to be used in the search for variable stars. Using statistical indices we were able to discover new eclipsing binary candidates and star with variability due to pulsation or rotation. A long analysis process is still necessary to exhaust the huge amount of information obtained in this survey.

The Cygnus OB2 region was observed 112 nights, covering 217 days. The observations followed the scheme used in the Orion Nebula survey, which consisted of one exposure (2 seconds long) each night. A preliminary analysis of the Cygnus OB2 data allowed us to discover 6 small scale cometary globules. This finding is strong evidence of the recent star formation process that occurred in this region. We also detected 4 infrared sources, apparently young and possibly located in the Perseus Arm, far more distant than the Cygnus OB2 association. We also determined the double nature of the IRAS 20304+4059 infrared source, which is classified as a protostar.

Chapter 1

Introduction

Star formation is nowadays one of the most important branches in astronomy. It all started with the first observation of late-type low mass stars in the Taurus-Auriga region by Joy (1945). Later, these stars were proposed to be young stars by Ambartsumian (1957) and they were labeled T Tauri stars, after the object thought to be the prototype of young solar mass stars. Herbig (1960) observed the intermediate mass relatives of T Tauri stars, the Herbig Ae/Be stars. Since these pioneer works we have seen an incredible growth of observations, both in quantity and quality, which supported the establishment of different models of formation, evolution and structure of stars. We study these young stellar systems in the hope that they will give us hints about the history of our own Solar System. We try to understand how stars and planets form so that we can comprehend how the Earth, and other planets in the Solar System, formed when the Sun was only a few million years old.

One of the things we have learned, during the study of young stars, is that most of them are formed in multiple systems (e.g. Leinert et al., 1993; Mathieu, 1994; Duchêne, 1999; Bodenheimer et al., 2000; Patience et al., 2002; Kroupa & Bouvier, 2003; Duchêne et al., 2004; Haisch et al., 2004). If that is true then why is the Sun a single star? A multiple system can be disrupted by different mechanisms such as the fast decay of small-N systems (Sterzik & Durisen, 1998; Reipurth & Clarke, 2001; Durisen, Sterzik & Pickett, 2001; Hubber & Whitworth, 2005; Goodwin & Kroupa, 2005; Umbreit et al., 2005) and the dynamical destruction caused by multiple interactions in clustered environment (Kroupa, 1995a,b; Kroupa et al., 2003). The former mechanism acts at the beginning of star formation, while the molecular cloud core ends its collapse. Nonhierarchical systems with $N > 3$ decay into single objects, binaries and hierarchical multiples. The latter acts during the whole life of the cluster. It consists of the interaction of multiple systems with the cluster's potential well and with the crowded environment that surrounds the object. This interaction will disrupt multiple systems that are loosely bound. Some models also predict that environmental influences, such as the molecular cores' temperature, could be important to define the initial binary fraction (Durisen & Sterzik, 1994; Sterzik, Durisen & Zinnecker, 2003).

The implications of multiplicity for the planet formation scenario, and also for the evolution

of stars, are still unknown. Recently, Stassun et al. (2008) reported the discovery of a pair of "stellar twins" in a binary system. Each star has a mass of 0.41 ± 0.01 $M_{\odot}$, identical to 2%. What makes the pair so special is the fact that although they are similar in mass, they have temperatures differing in $\sim$10% and luminosities by $\sim$50%, with high confidence levels. This binary system, with very similar components, though not identical as claimed by the authors, can give us hints about the influence that multiplicity can exert during the formation of stars.

Multiple systems play an important role in astronomy. They are very important for the calibration of evolutionary models and it is not much to say that the spectroscopic eclipsing binaries act in astronomy as "weights and rulers". These systems, in particular, can give us very precise ($\lesssim 1\%$) absolute parameters (mass, radius, ratio of temperatures, etc) which can be used as constraints to theoretical models. Although multiple systems seem to be very common at the early stages of star formation, only 22 pre-main sequence stars have parameters measured through the use of dynamical techniques (Mathieu et al., 2007; Stassun et al., 2008). In order to discover more eclipsing binaries it is necessary to perform accurate and comprehensive surveys with long time-line bases.

Since the beginning of the study of young stars it became clear that they are extremely variable objects. In fact, photometric variability was one of the criteria used to classify them. Young stars present photometric and spectroscopic variability in all wavelengths, from radio to X-rays. Some of the variability is caused by the circumstellar material in different ways. Circumstellar material can cause variable extinction when it crosses our line of sight toward the object, causing sudden drops of brightness. The process of accretion, through which the star increases its mass, can still be active, causing variability in brightness. In young T Tauri stars the convection zone in their interior creates magnetic fields strong enough to produce large scale cool spots in the photosphere, which along with the star's rotation produce a periodic modulation in the light curve. Flares in young stars, similar to solar flares, can also produce irregular photometric variability. The processes of accretion and ejection of matter can also change the line profile of many atomic species present in the photosphere of the star, giving birth to the spectroscopic variability in young stars (e.g. Guimarães et al., 2006). Pulsation was also observed in young stars (e.g. Kurtz & Marang, 1995) situated at the instability strip of the HR diagram.

After stating the above, we face here two important subjects, namely: multiple young stars and variable young stars. Both subjects are important and they are directly associated, since stars in multiple systems can be (and most of the time are) variable. We will only have a coherent picture of the star formation scenario if we study individual systems in detail. High precision in the determination of absolute parameters, of individual stars, is essential if we want to build models that really represent processes occurring in nature. But in order to select good candidates to study, we first need to discover them. That is the importance of large scale comprehensive surveys. Because astronomers are stuck on Earth, and thus do not have access to their experiments, it is necessary to map the whole sky in the search for the "good experiment". There are many difficulties in doing large scale surveys, for example, availability of telescope time to perform observations in specific areas of the sky, correct instrumentation, storage capacity for the huge amount of data, computational resources to process all the data collected, human resource in order to analyse the data, etc. Many all sky surveys were done recently, covering different wavelengths, such as: the Two Micron All Sky Survey (2MASS, Skrutskie et al., 2006) in the JHK near infrared bands, the Sloan Digital Sky Survey (SDSS, Fukugita et al., 1996) in

the Sloan optical bands (u', g', r', i', z'), the All Sky Automated Survey (ASAS, Pojmanski, 1997) in the optical V and I bands, the UKIRT Infrared Deep Sky Survey (UKIDSS) considered to be the successor to 2MASS, just to cite a few of them.

We are involved in the Variable Young Stars Optical Survey (VYSOS), which intends to continuously monitor stellar objects in star forming regions located in the Galactic plane and also to find new young objects in the same star forming regions. It was part of my project to work with the data collected by these telescopes.

The project consists of 2 small telescopes (the diameter of the main mirror is 41 cm), one installed in the northern hemisphere, at the Mauna Loa Observatory – Hawaii – USA, and the other in the southern, at Cerro Murphy – Chile.

Each telescope will be equipped with a set of Sloan filters (Fukugita et al., 1996) and an SBIG CCD, which has a dimension of 4096×2048 pixels and a pixel scale of $0\farcs77$. Such a combination of pixel scale and dimension will produce a field of view of $27' \times 40'$.

The northern telescope has been facing some mechanical and optical problems. In July 2006 I was at the Institute for Astronomy (IfA) in Hawaii, as part of my PhD program, when a major problem with the optical system was detected. The first problem was detected during the process of collimation. The optical system lacked one degree of freedom necessary to align the optical beam. This problem was reported to the engineers who built the system and some solutions were proposed by them. After trying different approaches we concluded that the missing degree of freedom was really necessary and the problem could not be solved without making a new base for the plain mirror, responsible for sending the optical beam straight to the camera. The difficulties in the process of alignment and collimation made us check the whole optical design and other problems were detected by Dr. Josh Walawender, a postdoc at IfA at that time. After calculations and studies of the optical system the conclusion was that it did not work, except in the optical axis. The set of optical lenses used to focus the beam leaving the tertiary mirror did not posses the necessary quality. Thus, due to construction and optical problems, the telescope was redesigned and many parts of it were rebuilt.

Formerly, the telescope was a modification of the Newtonian design. After being redesigned it was built as a Newtonian telescope. Such a modification brought some advantages, for example it decreased the number of mirrors and lenses used. The collimation and alignment were done easily this time. However, some issues remained, dealing mainly with the tracking system. We were not able to track during long exposures. Also, the telescope showed itself to be extremely sensible to vibrations of the dome. This problem was caused by the fact that there is not a separated pier for the telescope and all dome vibrations (caused by wind) were transmitted to the telescope through the floor. The floor where the telescope is fixed also presented some problems because it was not flat enough. The steel plates that should sustain all the weight of the telescope showed some signs of bending. A new mechanical problem was also found, caused by the 6.8 magnitude earthquake that stroke Hawaii on October 2006. The earthquake caused the telescope to bounce and the aluminum wheel responsible for the right ascension movement was slightly indented.

With so many issues dealing with the installation, the telescope operation was delayed. We decided to focus our work on new projects, which also dealed with photometric variations of young stars. Recently (August 2008) the telescope located in the Mauna Loa Observatory was taken down and will be replaced by a new one. The southern telescope was installed in the same

month but it is not working yet.

Thus, because our main project was delayed, we decided to study binary stars and variable stars from a different point of view. We will focus our attention in specific star forming regions, in order to build a comprehensive database, covering long periods, usually hundreds of days. Instead of looking at the whole sky, we will look at specific regions for a long time interval.

In our attempt to better understand multiple young stars, we report here the performance of an imaging survey using the Advanced Camera for Surveys, onboard the Hubble Space Telescope, of the well studied Orion Nebula. The main objective of this survey is to find new visual binaries in a wide region around the Orion Nebula Cluster. Previous studies have shown that the binary frequency of the Orion Nebula Cluster is lower than the binary frequency of the Galactic field. Does this fact have something to do with the dynamical evolution of the cluster? Can we distinguish between the two mechanisms responsible for the dynamical evolution of the binary properties? We will try to answer these questions in Chapter 2.

Our second incursion in the star formation domain is related to two near infrared large scale surveys of two different star forming regions. Our main goal is to unveil the young variable population of the Orion Nebula and of the young OB association Cygnus OB2. For this task we used the Wide Field Camera of the United Kingdom Infrared Telescope, the most capable infrared imaging survey instrument in the world, currently installed at the summit of the Mauna Kea Observatory. We will present in Chapter 3 some statistical techniques that can be used to characterize the variable star population in these fields. Light curves from the ASAS were used as tests in order to better understand the behavior of these statistical indices.

In Chapter 4 we will present the observations, procedures and results of the survey conducted in the Orion Nebula. We have built a database using 98 nights, from 101 observed nights covering 178 days, which is so far the longest infrared survey of the Orion Nebula. Many interesting variable objects were found after we applied the statistical indices to the database.

Cygnus OB2 will be analyzed in Chapter 5. It is a giant OB association, which was even considered to be a young globular cluster, given the number of O type stars associated to it ($\sim$100 stars). Cygnus OB2 is situated in the Cygnus X star forming region, behind the Great Cygnus Rift. When we look in that direction of the sky, we are looking through the Local Spiral Arm and the Perseus Arm and, hence, we can see many star forming regions projected in the same area of the sky. A better analysis of its low and intermediate mass content is necessary in order to put constraints to its total mass and extent. We observed the center of this OB association during 112 nights, covering an interval of 217 days, but given the huge amount of data we were not able to construct the final database yet. However, four nights were used to construct a preliminary catalog, which we used to study the properties of this interesting star forming region. It is the richest infrared survey made for this association and given the attained angular resolution we will be able to double the number of objects associated to it.

We will present our conclusions in Chapter 6.

Chapter 2

Visual Binaries in the Orion Nebula Cluster

2.1 Introduction

The Orion Nebula Cluster (ONC) is responsible for the ionization of the H II region know as the Orion Nebula (M42 + M43 = NGC 1976), one of the most studied regions in the sky. The ONC calls such attention because it is the nearest giant star forming region ($\sim$450 pc). Its most massive stars, know as the Trapezium stars, are located in its center. They were thought to be a distinct entity (e.g. Herbig & Terndrup, 1986) but it has been argued that they are actually the core of the ONC (Hillenbrand & Hartmann, 1998).

The ONC is not only the nearest site of high-mass star formation but is also very young, with age $\sim$1 Myr. Its youth is supported by:

- the stars located above the ZAMS (Zero Age Main Sequence) (Herbig & Terndrup, 1986; Prosser et al., 1994);
- the photometric variability of more than 50% of its stars (Jones & Walker, 1988; Choi & Herbst, 1996);
- the existence of optical emission line spectra (Herbig & Bell, 1988, and references therein);
- the high polarization;
- the infrared excesses;
- the proplyds pointing toward θ^1 Ori C (the most massive of the Trapezium stars).

The wind and radiation from the massive stars ionize the surrounding medium, with two important consequences. First, the ionization creates a low extinction ($A_V \leq 2.0$) line of sight to the stars around the Trapezium that allows us to study in detail this population. Second, the ionization of the molecular material behind the ONC creates a highly variable background brightness. This molecular material is part of the Orion Molecular Cloud which has a large column density ($A_V = 50 - 100$). Such high extinction helps us in the study of the ONC because it hides the background objects but also prevents us from achieving a complete census of the ONC stellar population.

The ONC has been studied in all wavelengths, from radio to X-rays. Since it is one of the most studied regions in the sky, a full review would be beyond the purpose of this work. We will focus our attention on the orbital evolution of its multiple systems.

An intriguing result of the study of the formation and evolution of binary systems is that binaries are more common (by a factor of 2) in T Tauri associations than in the field (e.g. Reipurth & Zinnecker, 1993; Simon et al., 1995; Duchêne, 1999; Ratzka, Köhler & Leinert, 2005). A more intriguing result is that the ONC has a binary frequency lower than T Tauri associations and the field (e.g. Prosser et al., 1994; Padgett, Strom & Ghez, 1997; Petr et al., 1998; Simon, Close & Beck, 1999; Köhler et al., 2006).

The study of binary properties is marked by the detailed work with field binaries made by Duquennoy & Mayor (1991, hereafter DM91). The properties of the binary field population serve as a reference to the work on younger populations. But can we trust the binary field population? How is it formed? Does the field population come from a mix of other cluster populations (e.g. loose T associations, OB associations, open clusters and so forth)?

In the recent literature there are two main models for the evolution of binary properties: 1) fast dynamical decay of small-N systems within cluster cores (e.g. Reipurth & Clarke, 2001; Sterzik & Durisen, 1998, 2003; Durisen, Sterzik & Pickett, 2001; Hubber & Whitworth, 2005; Goodwin & Kroupa, 2005; Umbreit et al., 2005) and 2) dynamical destruction due to multiple interactions in a clustered environment (e.g. Kroupa, 1995a,b; Kroupa et al., 2003).

The first mechanism acts in the initial stages of star formation, during the Class 0 phase, while the second mechanism needs more time to act and does so for a longer time. We can thus say that the fast decay mechanism acts on a small scale (the scale of the multiple system) while the dynamical destruction mechanism acts on a larger scale (the scale of the whole cluster). We will call them fast decay mechanism (FDM) and dynamical destruction mechanism (DDM).

Assume we have stars forming in a cloud. During the collapse of the cores many multiple systems are formed. The FDM will act on these multiple Class 0 systems in a way that the less massive components will be ejected and the resultant binaries will have their semimajor axis decreased.

The DDM will act in all the systems during their whole lives within the cluster. In order to help us understand how this works we will divide the binary systems into three classes.

1. the wide, or soft, binaries;
2. the dynamically active binaries;
3. the tight, or hard, binaries.

The wide binaries have orbital velocities much smaller than the velocity dispersion of the cluster. The DDM will disrupt these systems and thus populate the field with single stars. The hard binaries, on the contrary, have an orbital velocity much greater than the velocity dispersion. These binaries will release energy to the cluster, becoming harder.

These facts lead Heggie (1975) and Hills (1975) to propose the following law: soft binaries soften and hard binaries harden.

The dynamically active binaries have intermediate binding energies and are difficult to study analytically. However, computations show that these binaries are efficient in exchanging partners when interacting with the other binaries and single stars in a cluster.

An important point to note, coming from the computational simulations, is that dynamical interactions cannot form a significant number of binaries from an initially single star population (Goodwin et al., 2007).

Two points of view come into shock at this present time. Goodwin & Kroupa (2005) argue that almost all stars are formed in multiple systems, meaning that the initial binary fraction is close to unity. The later low binary fraction among M dwarfs would then be caused by the preferential destruction of these low mass systems. They are the first ones to be disrupted by both mechanisms. On the other hand, Lada (2006) argues that because most M dwarfs are single and most stars are M dwarfs, then most stars form as single stars.

Köhler et al. (2006) suggest that the initial binary frequency in the ONC was lower than in Taurus-Auriga. This fact suggests that the binary formation rate is influenced by environmental conditions. Their results do not agree with the mechanisms described by Goodwin & Kroupa (2005).

The statistics of binarity for the ONC were poor and concentrated on regions around the Trapezium stars. Such an important statement should be based on more solid grounds. We will show here, using significant numbers, that the ONC indeed has a lower binary fraction than the T Tauri associations and the field, as reported previously in literature.

We present here a study of the ONC using the Advanced Camera for Surveys (ACS) onboard the Hubble Space Telescope (HST). Our major goal is to study the binary frequency of the ONC, focusing on the outskirts of the cluster and excluding the inner region around θ^1 Ori C. The results presented here were published in the Astronomical Journal, see Reipurth et al. (2007).

2.2 Observation and Catalogs

During program GO-9825, 26 fields were observed with the F658N filter (Hα+N[II]) and an exposure time of 500 seconds per pointing. These 26 fields when combined yield a mosaic image that covers an area of 415 arcmin^2 with a very high angular resolution ($0\farcs05$ per pixel). Further details of the observations are described in Bally et al. (2006) and a schematic figure showing the disposition of the observed areas is shown in Figure (2.1).

Due to the high stellar density in the Trapezium region we excluded a circular region with radius $60''$ centered in θ^1 Ori C, as can be seen in Fig. (2.1). We will not take this region into account in our work. We focus our attention on a larger area around the Trapezium, where we are able to probe the low mass stellar population.

We tested an automatic procedure to detect the stellar sources but it did not yield satisfactory results. The routines were written in IDL (Iteractive Data Language) and made use of the package IDLASTRO, which is a library with many routines written specifically to deal with astronomical issues.

Each one of the 26 images was opened with the *readfits.pro* sub-routine and the data was loaded into a matrix called *data*. The astrometrical information, contained in the header of each image, was extracted with the *extast.pro* sub-routine to be used later in the recovery of the coordinates. Then a sub-routine called *find.pro* was applied to the *data* matrix in order to detect the astronomical sources. It requires some input parameters in order to control the level of detection. The main input parameters for the *find* sub-routine are: roundness, sharpness, hmin, FWHM (Full Width at Half Maximum).

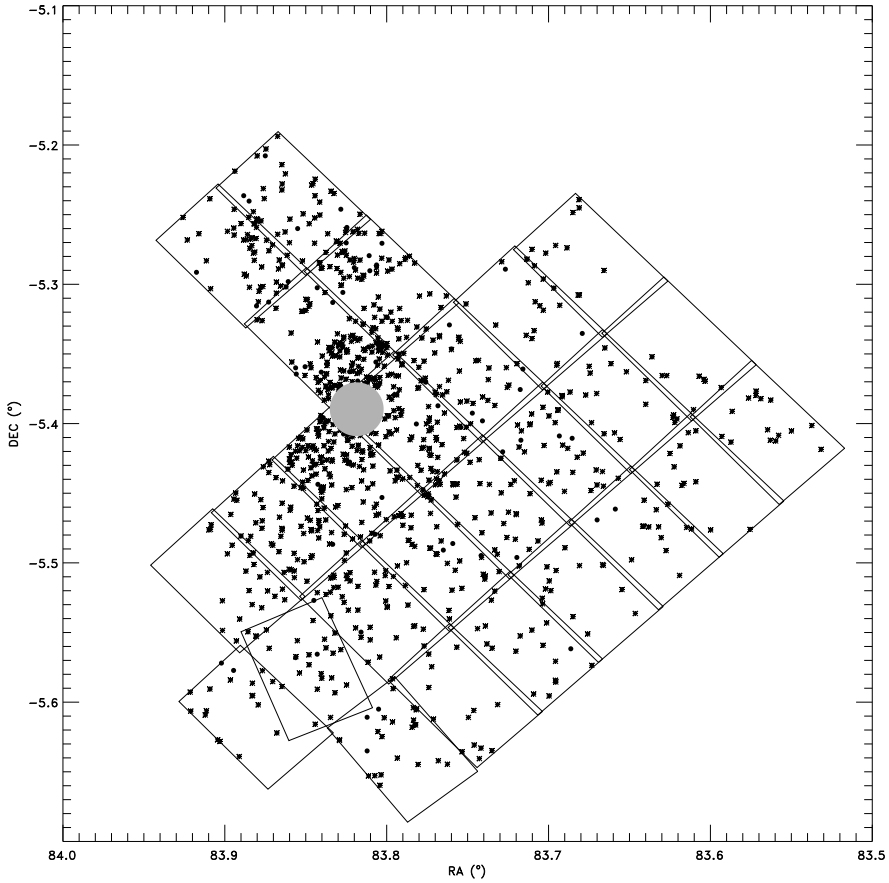

Figure 2.1: Distribution of the visual binaries, with different separations, in the observed region. The grey solid circle, with a radius of $60''$ and centered in θ^1 Ori C, is called the exclusion zone. We did not consider, in our analysis, any star inside this zone. Single stars are plotted as asterisks and binaries (triples included) are plotted as black filled circles.

The *roundness* parameter is related to the geometric form of the object being searched, it is a 2-dimensional vector (between -1 and 1, the default values) and should only be changed if the objects are elongated. Since we have many saturated objects in our images this parameter was of not much use when applied to these cases and in fact introduced many false detections.

The *sharpness* parameter relates to the kind of statistical distribution followed by the objects. It is also a 2-dimensional vector where the default values are 0.2 and 1.0. These values should only be changed in case the objects' point spread function is different from a Gaussian. As in the case of the *roundness* limit, the *sharpness* limit was not of much help while dealing with saturated objects and high background brightness.

The *hmin* parameter is the threshold intensity for the point source. Its value should be 3 or 4 σ above the background noise. We have very faint objects in our sample, thus we cannot put the threshold limit too high. However, setting this limit to a low value would also cause a very high number of detections, given the high background brightness variability. This parameter became our biggest problem while trying to use an automatic detection procedure.

The FWHM is the value of the full width at half maximum to be used in the convolve filter. Because we have so many different objects, with very different intensities, this parameter did not help us discard the false detections.

We tested this automatic procedure many times, with different sets of values for the input parameters, but the output was far from useful. The procedure always returned several thousands of detections per image. Because of this we decided to search the image by eye, individually.

We had to take some care while checking the stellar sources by eye because some images overlap, as can be seen in Fig (2.1). All the overlapping areas were carefully inspected and the stellar sources detected in more than one image were catalogued and counted only once. In the end we detected 1 051 stellar sources in the whole area.

The coordinates for each object were obtained using two routines, also written in IDL. The first one was responsible for obtaining the pixel coordinates of the stellar sources, through the use of a 2-dimensional Gaussian function. The center of the 2D-Gaussian was taken as the center of the stellar source. The pixel coordinates were then transformed to celestial coordinates with the IDLASTRO sub-routine called *xy2ad.pro*.

Once the stellar sources were catalogued we were able to go to the next step, selection of the multiple systems. Visual binaries have two important parameters, the position angle (PA) and the separation (S) between the pair. The position angle measures the angle between the primary and secondary and it is counted from North to East (counterclockwise), using the primary as reference. Figure (2.2) exemplifies the position angle and separation between two stars in a binary system.

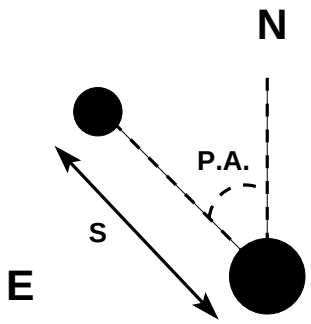

Figure 2.2: Definition of the position angle (PA) and separation (S) between primary and secondary in a binary system.

To calculate the position angle we used an IDLASTRO subroutine called *posang.pro*. The separation between the stars was obtained in two distinct ways. The first method applies the IDLASTRO sub-routine *gcirc.pro*, which calculates rigorous arc distances in spheres. In the second method we used the pixel coordinates to obtain the distance between the objects in the plane of the image, discarding any deformation caused by the sky projection onto the plane of the CCD. Both methods yielded similar results, which can be explained by the fact that the separations are too small to be influenced by the projection of the celestial sphere onto the plane of the CCD, and also because the observed region is close to the equator, where the field deformation is less pronounced. Because some binaries have a very small separation ($<0\farcs15$) we decided to apply the trigonometric method in order to obtain the angular separation. We decided on this method because in our opinion, on these small scales, the pixel coordinate is more accurate than the astronomical coordinate.

2.3 Membership of the ONC

We used 4 criteria to establish whether a star in our sample belongs to the ONC:

1. it has proper motion given by the Jones & Walker (1988, from now on, referred to as JW) catalogue and the membership probability is $\geq 93\%$;
2. it is listed as an ONC member by the X-ray survey performed by the Chandra satellite (COUP project – (Getman et al., 2005));
3. it presents irregular variability as listed by the GCVS (General Catalogue of Variable Stars);
4. it has Hα emission (detected in our unpublished catalogue).

A star does not need to obey all the criteria at the same time, it is sufficient to present one of them to be classified as a member of the ONC. From 1 051 stars in our sample, 655 are listed in the JW catalogue and 596 have a membership probability $\geq 93\%$. We want to point out that most of our binaries are not resolved in the JW survey, given it was made with photographic I-band plates. This fact implies that the proper motions can be affected by changes in the brightness of the companion stars. We observed such variations in our sample. One of our binaries is located on the edge of two images which overlap themselves. Since the observations were made in different epochs we were able to detect a brightness variation in the system. Such variation can change the photocenter of the pair (in an unresolved image, like the photographic plates used by JW) and thus lead to a wrong proper motion. We also would like to point out that some stars with 0% membership probability showed signs of youth, which is good evidence of its association with the ONC. Hence, we concluded that the proper motion information is useful to support the membership of a system, but such information should not be used to exclude membership. Information about the youth of the system can be gathered from other sources, like X-ray emission, Hα emission and photometric variability. That is the reason why we used the COUP catalogue (X-ray), the GCVS (variability) and the unpublished Hα catalogue. Not all young stars present Hα emission, but we assume that a star in the Orion region that presents such emission line is young. From the 1 373 ONC members in the COUP catalogue, we found that 658 are present in our sample. We found 196 variable stars in our sample and 99 stars presented Hα emission.

In the end, out of our 1 051 stars, 781 present at least one (and commonly several) of these four characteristics. We found 75 visual binaries and 3 visual triples among these 781 ONC members. Table (2.1) presents these binaries, columns 1 and 2 list the JW number and probability of the star being a member of ONC, respectively. Columns 3 and 4 present the name in the GCVS catalogue and the COUP number, respectively. Right ascension and declination are listed in columns 5 and 6, for equinox J2000.0. Columns 7 and 8 list the position angle and the separation (in arcseconds) of the system, while column 9 lists the apparent magnitude in the I band (Hillenbrand, 1997, hereafter called H97). The difference in magnitudes from the primary to the secondary, in the Hα filter, is listed in column 10, where the symbol $>$ indicates that the primary is saturated (sometimes both stars), thus Δm is only an aproximation. Columns 11 and 12 list the position angle and separation (in arcseconds) to θ^1 Ori C. Column 13 lists the spectral type given by SIMBAD. Column 14 lists the membership criteria presented by the system: P for proper motion; X for X-ray; H for Hα emission; V for irregular variability. Column 15 lists

the discovery paper in case the binary was already known and the letters correspond to the references: a - Prosser et al. (1994); b - Padgett, Strom & Ghez (1997); c - Simon, Close & Beck (1999); d - Köhler et al. (2006); e - Getman et al. (2005); f - Lucas, Roche & Tamura (2005).

Table (2.2) lists binaries that were found in our sample but that were not used in our analysis. The reasons for not using these binaries are: three binaries have separation in the range $0\farcs11$ and $0\farcs15$, other three binaries are within the exclusion zone and have separations less than $0\farcs4$ and seven binaries do not show any evidence of membership to ONC. The columns in Table (2.2) are the same as in Table (2.1) with one more column that characterizes the binaries as: 1 - binaries with angular separation $< 0\farcs4$ inside the exclusion zone; 2 - binaries with angular separation $<0\farcs15$ outside the exclusion zone and 3 - binaries with angular separation $< 1\farcs5$ outside the exclusion zone but with no evidence of ONC membership .

With the exception of the object JW 945, which is a Herbig Ae/Be star, all of the binaries in our sample consist of late-type stars, see Table (2.1). Figure (2.3 presents stamps for the 72 visual binaries, 3 visual triples and also the 3 visual binaries inside the exclusion zone.

2.4 Completeness

Since our major goal is to search for visual binaries in the ONC, we have to account for the contamination due to line-of-sight alignment. We must set an inferior and a superior separation limit for our search.

The inferior limit was determined based on the angular resolution obtained with the ACS ($0\farcs05$) and with a blind test. We selected 5 stars in our images that presented a good Gaussian profile. An IDL routine was written to copy this Gaussian profile and create artificial stars, which were then positioned beside real stars but with random separations, position angles and flux ratios. Seven sets of 25 images each were created. One example of the artificial binaries is shown in Fig (2.4).

The blind test consists of looking at each image in sequence during no more than 5 seconds. If the pair is visible and easily detected, we call it a positive target. If it is not possible to detect the pair within 5 seconds, we call it a negative target. Three of us (Bo Reipurth, Michael Connelley and I) did this test for each set of artificial binaries and the positive and negative targets were added. If one person counted a target as positive but the other two counted it as negative, the target was then counted as negative. Likewise, two positives and one negative was counted as one positive.

Figure (2.5) presents the results of this blind test. Our observed binaries are shown in the left panel. The right panel shows the detections found during the blind test, where filled circles indicate systems in which we could detect the companions and open circles represent those in which we were not able to. We can detect binary systems down to $0\farcs10$, however, our sample will not be complete in this limit, as can be seen in Fig. (2.5). We have set our inferior limit to $0\farcs10$, but we will use in our subsequent analysis only the binaries with separation $\geq 0\farcs15$.

The superior limit was determined based on the probability of a companion being a line-of-sight contamination, as used by Correia et al. (2006). We used Eq. (2.1) to calculate this probability:

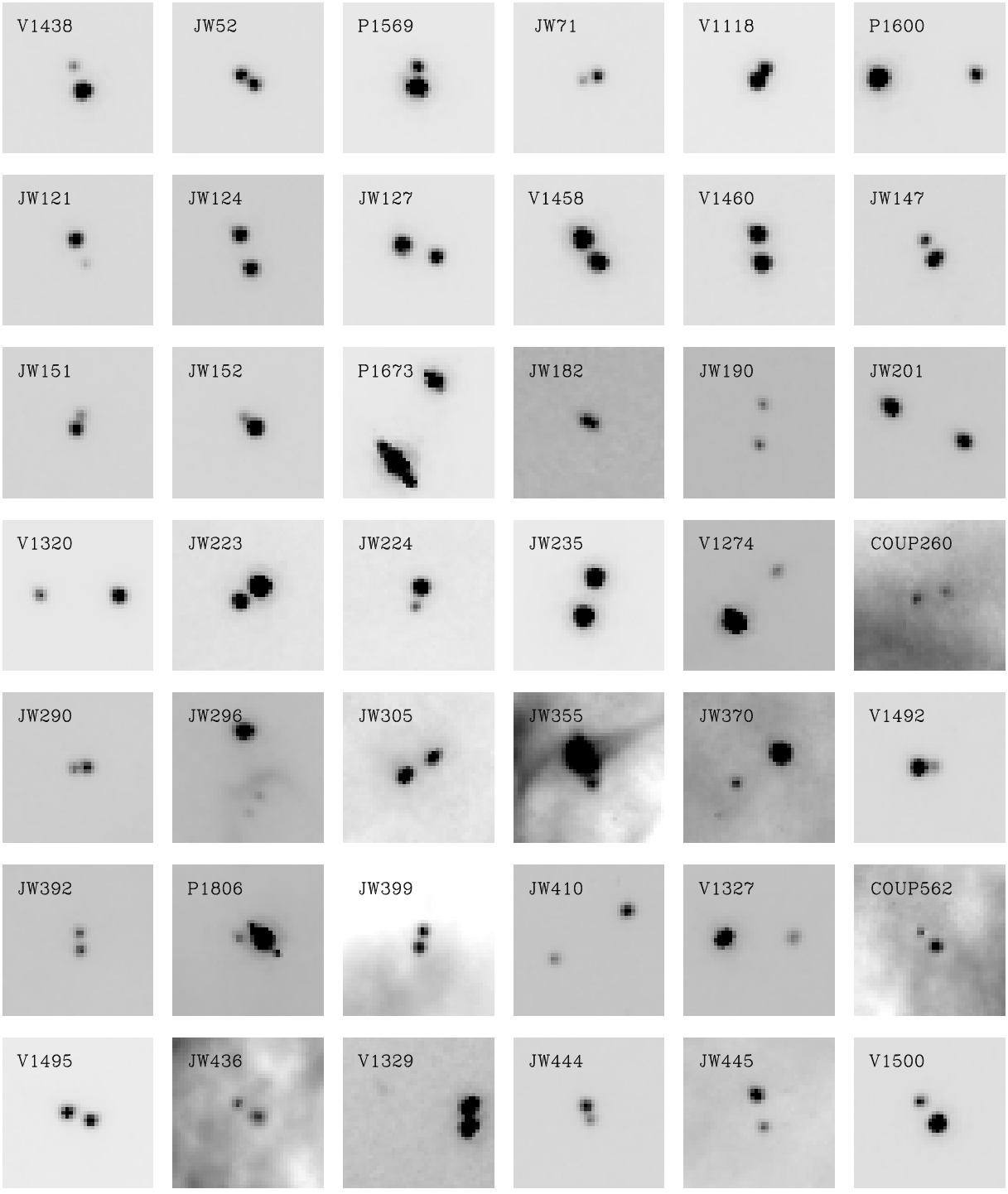

Figure 2.3: All binaries identified among the ONC members. Each stamp is $2''$ wide, with north pointing up and east pointing left.

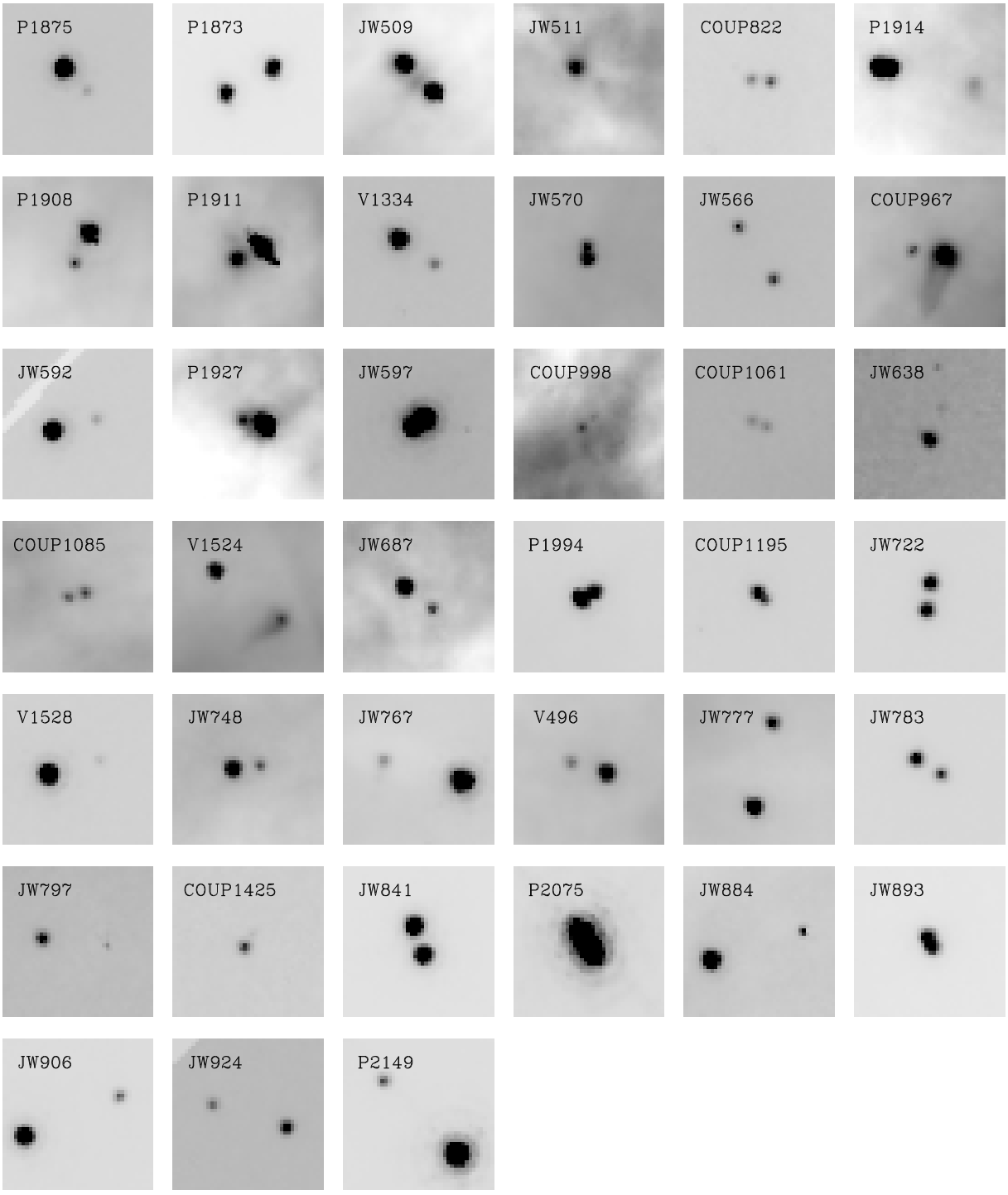

Figure 2.3: Continued

Table 2.1: Pre-main sequence binaries with angular separation between 0.15″ and 1.5″, outside the 60″ exclusion zone around θ^1 Ori C.

JW	%	GCVS	COUP	RA	DEC	PA(sys)	S	m_I	$\Delta m_{H\alpha}$	PA(cluster)	OriC	SpT	Memb.	Bin
39	99	V1438	...	5:34:38.1	-5:27:41	21	0.38	14.29	2.6	246	628	M3	P00V	
52	98	...	...	5:34:40.8	-5:28:09	231	0.20	14.58	0.1	242	604	M5	P000	
63	99	V1441	17	5:34:43.0	-5:20:07	0	0.27	12.75	1.5	291	537	K6	PX0V	
71	99	...	21	5:34:44.5	-5:24:38	105	0.20	15.61	1.4	261	483	M4	PX00	
73	99	V1118	...	5:34:44.7	-5:33:42	329	0.18	14.04	0.4	217	779	M1	P0HV	
81	97	...	28	5:34:46.4	-5:24:32	272	1.34	12.91	1.9	261	454	M0	PX0V	
121	99	...	...	5:34:51.2	-5:16:55	200	0.34	14.90	3.0	316	541	M3	P00V	
124	99	...	64	5:34:51.8	-5:21:39	200	0.48	13.94	0.0	286	382	M3.5	PX0V	
127	99	...	66	5:34:52.1	-5:24:43	254	0.48	14.28	0.6	258	373	M3.5	PXHV	
128	97	V1458	67	5:34:52.2	-5:22:32	215	0.39	12.64	>0.6	278	366	M2.5	PXHV	
135	99	V1460	72	5:34:52.7	-5:29:46	11	0.40	14.45	0.1	223	522	M3	PX0V	
147	99	...	...	5:34:54.4	-5:17:21	26	0.30	14.80	1.4	318	489	M5	P000	
151	99	...	95	5:34:54.8	-5:25:13	332	0.15	15.44	1.6	251	341	M3	PX00	
152	99	...	96	5:34:55.1	-5:25:30	51	0.18	14.12	2.5	248	343	M3	PX00	
176	99	KQ	123	5:34:57.8	-5:23:53	336	1.28	11.58	>1.1	264	280	K8	PX0V	e
190	99	...	134	5:34:59.3	-5:23:33	355	0.56	15.33	0.3	268	256	M6	PX00	f
201	99	...	150	5:35:01.0	-5:24:10	246	1.09	13.41	0.8	258	235	M2.5	PXH0	
222	98	V1320	174	5:35:02.2	-5:29:10	89	1.07	14.14	1.4	212	407	M2	PX0V	
223	99	...	177	5:35:02.4	-5:20:47	130	0.34	13.64	1.3	307	261	...	PX00	
224	99	...	180	5:35:02.7	-5:19:45	164	0.27	15.38	2.4	317	299	M1	PX0V	
235	0	...	197	5:35:03.6	-5:29:27	346	0.54	13.69	0.4	208	411	...	PXHV	d
248	99	V1274	214	5:35:04.4	-5:23:14	320	0.90	12.73	>3.7	273	180	M3	PX0V	e
...	...	...	260	5:35:06.2	-5:22:13	284	0.40	16.20	0.3	295	169	M4	0X00	f
296	99	...	275	5:35:06.6	-5:26:51	196	0.89	14.30	3.2	215	255	M4.5	PX00	
296	99	...	275	5:35:06.6	-5:26:52	158	0.27	14.30	0.4	215	256	M4.5	PX00	
305	99	...	...	5:35:07.6	-5:24:01	302	0.45	14.58	0.3	254	137	M3	P00V	f
355	0	...	402	5:35:10.9	-5:22:46	197	0.42	15.03	3.5	294	90	K:	0X00	
370	99	...	452	5:35:11.9	-5:19:26	122	0.73	13.86	3.5	344	246	K1.5	PX00	
383	99	V1492	489	5:35:12.7	-5:16:14	280	0.19	14.57	2.1	353	433	M3	PX0V	
392	99	...	498	5:35:12.7	-5:27:11	185	0.23	15.21	0.2	194	234	M6	PX00	
391	99	...	501	5:35:12.8	-5:20:44	94	0.29	12.97	>3.3	341	168	M1	PX0V	
399	99	...	523	5:35:13.2	-5:22:21	345	0.22	16.77	0.1	322	78	...	PX00	a,c
410	99	...	...	5:35:13.2	-5:36:18	167	1.19	16.00	1.3	184	777	...	P00V	
406	99	V1327	543	5:35:13.5	-5:17:10	271	0.95	13.88	2.6	353	375	M1	PX0V	d
...	...	...	562	5:35:13.6	-5:21:21	62	0.24	16.27	1.5	341	129	M3	0X00	a
422	99	V1495	566	5:35:13.7	-5:28:46	74	0.31	14.43	0.0	187	326	...	PX0V	
436	0	...	620	5:35:14.3	-5:22:04	238	0.32	16.97	1.0	338	85	...	0X00	a,c
439	99	V1329	626	5:35:14.5	-5:17:25	150	0.30	14.97	0.1	355	359	M1	PX0V	
439	99	V1329	626	5:35:14.5	-5:17:25	78	1.21	14.97	4.1	355	359	M1	PX0V	
444	99	...	651	5:35:14.6	-5:16:46	190	0.18	15.53	1.0	356	398	...	PX00	
445	26	...	645	5:35:14.7	-5:20:42	191	0.44	14.67	1.8	351	163	...	0X00	a
...	...	V1500	...	5:35:14.9	-5:36:39	82	0.38	14.45	2.2	182	797	...	000V	
465	97	V409	...	5:35:14.9	-5:38:06	271	0.43	14.71	4.1	182	883	...	P00V	
498	99	V1504	...	5:35:15.8	-5:32:59	122	0.70	13.81	0.2	181	576	...	P0HV	
509	99	...	789	5:35:16.2	-5:24:56	46	0.49	15.06	0.1	182	93	...	PX0V	a,b,f
511	99	...	...	5:35:16.3	-5:22:10	241	0.41	15.67	2.4	358	73	M1	PX00	a,c,e,f
...	...	...	822	5:35:16.8	-5:17:17	84	0.26	16.37	0.5	1	366	...	0X00	
551	99	...	881	5:35:17.4	-5:25:45	265	0.14	13.87	0.0	174	142	M1	PX00	a
551	99	...	881	5:35:17.4	-5:25:45	262	1.27	13.87	3.6	174	143	M1	PX00	
552	99	V410	897	5:35:17.5	-5:21:46	156	0.46	14.50	>1.8	9	99	...	PX0V	a,c
560	98	V1334	927	5:35:17.9	-5:15:33	235	0.60	14.17	3.2	3	471	...	PX0V	
570	99	...	937	5:35:17.9	-5:25:34	0	0.15	14.73	0.8	170	133	...	PX00	a,b
566	0	...	939	5:35:18.0	-5:16:13	214	0.86	14.93	0.0	3	430	...	0X00	d
...	...	...	967	5:35:18.4	-5:24:27	78	0.42	15.16	2.4	155	70	M2.5	0X00	a,b,f
592	99	...	974	5:35:18.5	-5:18:21	285	0.61	14.37	4.0	6	304	M2.5	PX00	
597	0	...	994	5:35:18.8	-5:14:46	307	0.17	14.02	0.1	4	519	...	0XHV	
...	...	...	998	5:35:18.8	-5:22:23	314	0.20	17.54	0.3	31	70	...	0X00	a
...	...	...	1061	5:35:20.0	-5:18:47	71	0.22	17.31	0.1	11	281	M9	0X00	
638	99	...	1077	5:35:20.0	-5:29:12	354	1.01	17.03	3.2	171	353	...	PX0V	
681	99	V1524	...	5:35:21.4	-5:23:45	232	1.09	16.39	0.9	107	77	K7	PX0V	a
687	54	...	1158	5:35:21.7	-5:21:47	231	0.49	14.66	2.1	39	124	...	0X0V	a,c
709	99	...	1202	5:35:22.2	-5:26:37	309	0.22	12.92	0.5	156	213	M0.5	PX00	
722	98	...	1208	5:35:22.3	-5:33:56	216	0.36	14.51	0.2	172	639	M4.5	PX00	
727	99	V1528	1233	5:35:22.8	-5:31:37	285	0.73	13.87	4.7	169	503	M2	PXHV	
748	99	...	1279	5:35:24.1	-5:21:33	277	0.35	14.77	2.0	46	159	M3	PX0V	a
767	99	...	1316	5:35:25.2	-5:15:36	75	1.13	13.89	>4.1	16	485	M2.5	PX0V	d
776	99	V496	1328	5:35:25.4	-5:21:52	73	0.50	14.20	1.8	56	162	...	PX0V	a
777	80	...	1327	5:35:25.5	-5:21:36	347	1.19	15.15	1.2	52	173	K6	0X00	
783	95	...	...	5:35:25.5	-5:34:03	283	0.40	14.17	0.8	168	656	...	PX00	
797	99	...	1363	5:35:26.6	-5:17:53	323	1.42	16.30	2.8	25	363	...	PX00	
...	...	...	1425	5:35:29.5	-5:18:46	329	0.23	16.06	2.6	35	338	...	0X0V	
841	99	...	...	5:35:30.0	-5:12:28	16	0.41	14.41	0.1	17	686	M4	P0HV	
867	99	...	1463	5:35:31.3	-5:18:56	212	0.29	12.19	>0.3	40	347	K8	PXHV	
884	99	...	...	5:35:32.4	-5:14:25	287	1.32	14.91	2.8	24	589	...	P000	
893	99	...	...	5:35:33.2	-5:14:11	208	0.15	14.07	0.0	24	606	...	P00V	
906	99	...	...	5:35:34.7	-5:34:38	293	1.39	14.17	2.7	158	728	M3	P00V	
924	99	...	...	5:35:36.5	-5:34:19	73	1.04	16.63	1.3	156	722	...	P000	
945	99	...	...	5:35:40.2	-5:17:29	46	1.41	12.51	3.6	45	501	B6	P000	

$$P(\Sigma, \Theta) = 1 - e^{-\pi \Sigma \Theta^2} \tag{2.1}$$

where Σ is the surface density of stars and Θ is the separation limit, in our case it was set to

Table 2.2: Other binaries with angular separations $< 1.5''$ toward the ONC.

JW	%	GCVS	COUP	RA	DEC	PA	SEP	m_I	$\Delta m_{H\alpha}$	PA	OriC	SpT	M	Bin	C
553	99	V1510	899	5:35:17.6	-5:22:57	113	0.36	12.41	1.4	34	31	K3.5	PX0V	a	1
596	99	AF	986	5:35:18.7	-5:23:14	78	0.30	13.06	2.2	75	34	K3.5	PX0V		1
...	...	...	1085	5:35:20.2	-5:23:09	104	0.21	...	0.4	76	57	...	0X00		1
182	48	...	127	5:34:58.0	-5:29:41	77	0.11	16.56	0.2	216	467	...	0X00		2
290	99	...	266	5:35:06.4	-5:27:05	84	0.11	15.48	1.3	214	268	...	PX00		2
...	...	...	1195	5:35:22.3	-5:18:09	227	0.11	15.67	0.8	15	326	...	0X00		2
...	...	...	...	5:34:19.5	-5:27:12	168	0.56	10.52	0.1	255	881	G5			3
58	0	...	...	5:34:41.8	-5:34:30	282	1.43	16.13	2.2	218	844	...			3
61	46	...	...	5:34:42.7	-5:28:37	153	0.45	13.52	0.9	238	594	...			3
...	...	...	...	5:34:45.8	-5:30:58	324	0.46	...	0.1	225	645	...			3
...	...	...	...	5:35:01.4	-5:24:13	292	0.28	...	0.6	257	231	...			3
...	...	...	...	5:35:18.3	-5:24:39	96	0.67	16.72	2.2	160	81	...			3
...	...	...	...	5:35:30.0	-5:34:31	237	1.29	...	0.3	163	699	...			3

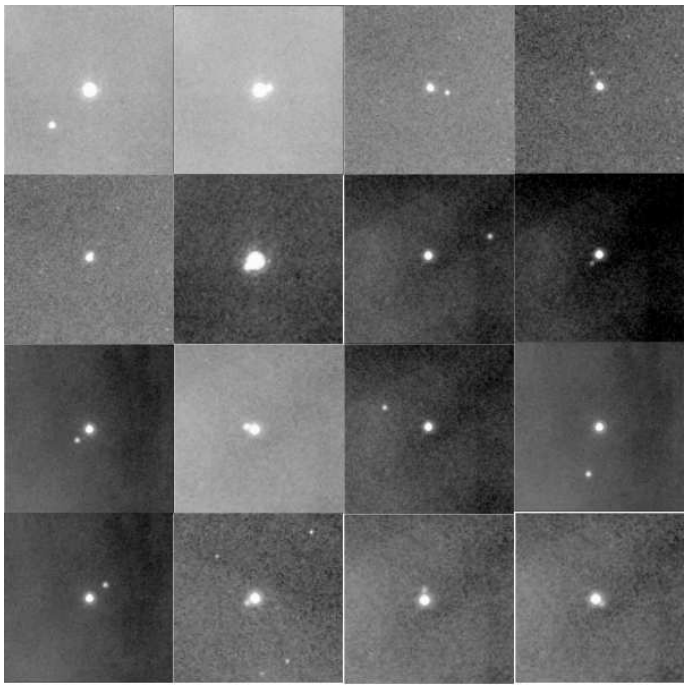

Figure 2.4: Examples of the artificial binaries, created using the profiles of real stars of our sample, in order to analyse our completeness.

$1\farcs5$. Because Correia et al. (2006) do not describe in detail the meaning of this equation, we decided to give more details about it in the following.

First, we need to know what is the probability of finding a companion to a primary star given a certain separation Θ. We can translate this to the following equation (P stands for primary and C for companion):

$$\text{prob(P in field AND C within } \Theta) = \text{prob(P in field)prob(C within } \Theta) \quad (2.2)$$

The probability of the primary being in the field is 1, because we are using it as the central star. In order to calculate the probability of finding a companion within the given radius, we will use the Poisson distribution, because these are rare events and we have lots of trials. Using the Poisson distribution we have:

$$\text{prob(C within } \Theta) = e^{-\mu} = e^{-\pi\Theta^2\Sigma} \quad (2.3)$$

where μ is the mean value and it is equal to the given area ($\pi\Theta^2$) multiplied by the surface density of stars (Σ).

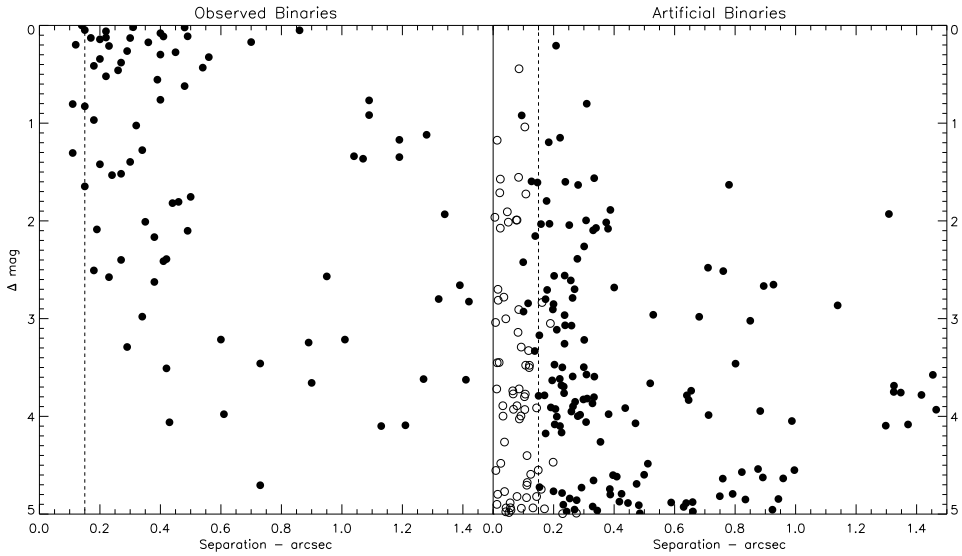

Figure 2.5: These two plots show the Δm versus *binary separation* in arcseconds. The observed binaries are shown in the left panel, where the dashed line indicates the $0\farcs15$ separation limit. The right panel shows the artificial binaries, created from real stars present in our images, with different separations, position angles and Δm. In the right panel, filled circles indicate systems where we could detect the companions, while open circles represent those where we were not able to detect them.

Hence, the probability of finding a companion to a star, given a certain radius is:

$$\text{prob(P in field AND C within } \Theta) = e^{-\pi\Theta^2\Sigma} \tag{2.4}$$

Now that we know the probability of finding a companion, we only have to subtract 1 to find the probability of a companion being a line-of-sight contamination, which was given in Eq. (2.1).

To calculate the surface density we applied two distinct methods. The first method consists of counting the number of stars inside a circle of $30''$ radius centered on each star of our sample and dividing this number by the area of the circle. This way we obtain a local density of stars which are influenced by the subclusters in that specific area. The second method consists of defining large circular areas starting from the exclusion zone. Each annulus has width of $30''$ and the density was again obtained counting the stars inside each area and dividing by the area of the annulus. One problem with this method is the shape of our mosaic, which can be seen in Figure (2.1). Because we centered each annular area in θ^1 Ori C, when the radius increases beyond $60''$ we start to have part of the annulus outside our surveyed area. We fixed this problem by calculating the area outside the mosaic, which means that the area used to calculate the density takes into account only the amount inside the mosaic. The first annulus has inner radius starting at $60''$ and outer radius at $90''$. The second annulus starts at $90''$ and ends at $120''$. The other areas continue with a step of $30''$ each with the last annulus having an outer radius of $1\,020''$. In the end we came to the conclusion that the correct procedure should be the first one because it was the only way to account for the subclustering observed in the Hα images.

The value of $1\farcs5$ was chosen because it allows us to study the wide visual binaries (at

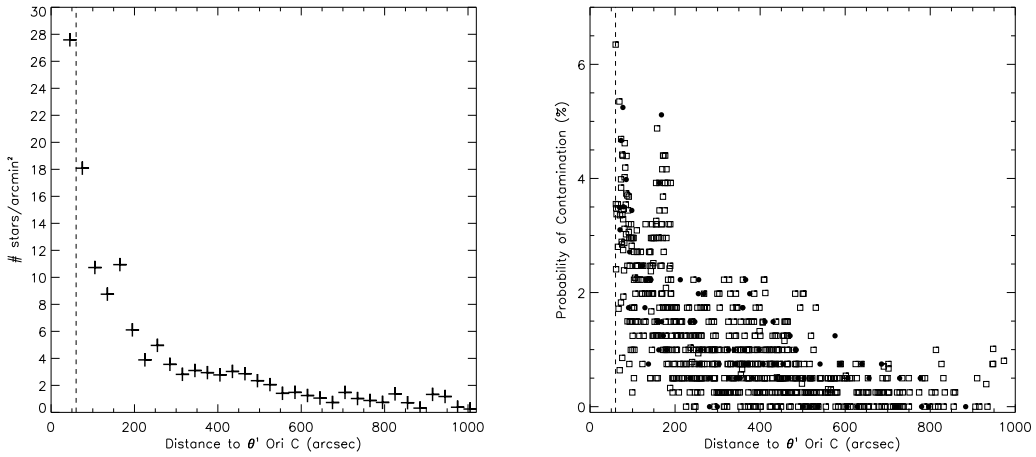

Figure 2.6: Left panel: surface density profile of the ONC members as a function of distance to θ^1 Ori C. The exclusion zone is indicated by the dashed line. This profile was used as a guide to understand and localize the subclustering in the region studied. It was not used to obtain the probability of chance alignment. Right panel: probability that a star would have a companion as a line-of-sight association, obtained with Eq. (2.1). Presented here are all the 781 ONC members, squares for single stars and circles for binaries. One can see a subclustering around 180″. We used the surface density obtained considering the number of stars inside an area of 30″ centered in each star.

this separation these systems are still gravitationally bound) without compromising the overall contamination of false pairs. To obtain the number of false pairs we added up the probability of being a chance alignment of all the stars (781 members). We have 9 flase pairs in our sample, which means we have a contamination of 11% (9 false pairs among 781 members). Thus, the superior limit (1.″5) was chosen as the separation that minimizes the contamination by false pairs but still provides systems that are likely to be physically related.

The left panel of Fig. (2.6) shows the ONC density profile, calculated using the second method described above, while the right panel shows the probability of the companion being a line-of-sight association. In both panels it is possible to see a subclustering in the analyzed area. Since we are using a narrow band filter, which is extremely sensitive to the background brightness, we cannot be sure if the subclustering is real or not. It exists in our Hα images, however, there are many stars which were not detected in these images. This is another completeness problem in our sample and it is an unquantifiable one.

2.5 Results

2.5.1 Binary Fraction

With our range set to 0.″15 – 1.″5, we have 72 binaries and 3 triples, members of the ONC. If we correct this number for the contamination described previously and count 1 triple as 2 binaries we end up with 69 physical binaries. Such a number implies a binary fraction of (8.8±1.1)% in the interval 67.5 to 675 AU (0.″15 to 1.″5), where the error was estimated as 1σ based on Poisson statistics. If we count one triple as a single system we can calculate the multiplicity frequency, which gives us a value of (8.5±1.1)%, with errors estimated in the same previous way.

Analyzing the inner 40″×40″ area of the Trapezium cluster, Petr et al. (1998) found four binaries in the separation range 0.″14 – 0.″50, which corresponds to a binary fraction of (5.9±4.0)%.

In the same separation range we have 50 binaries leading us to a value of (6.4±0.9)%. The numbers agree inside the error bars, however one must remember that we do not analyse the inner zone of the Trapezium.

Reipurth & Zinnecker (1993) observed nearby T Tauri associations and found 38 binaries out of 238 stars in the range 150 – 1800 AU. The common range between our work and Reipurth & Zinnecker is 150 – 675 AU. We calculated the binary fraction (counting the three triples as six binaries) in this common range for both samples. The numbers are: (11.8±2.2)% for the nearby T Tauri associations and (5.3±0.8)% for ONC. These numbers lead us to conclude that the binary fraction in T Tauri associations is higher than in ONC by a factor of 2.2, in qualitative agreement with Petr et al. (1998).

2.5.2 Separation Distribution Function

The left panel of Figure (2.7) presents the separation distribution function in an angular scale, with bins $0\farcs1$ wide. There is a clear decrease in the number of binaries with separations larger than $0\farcs5$. The same distribution, but in a logarithmic scale, is presented in the right panel of the same figure, where we also plotted the binary contamination and the distribution of the field stars based on DM91. The contamination by line-of-sight pairs was calculated using Eq. (2.1), but with the separation parameter set to the separation of each pair, the probabilities were added up for each bin. This approach is meaningless for individual objects but it can be used to distribute the false binaries in each bin. For example, the total of the probabilities for all the systems in the last bin in the right panel of Fig. (2.7) is 68%. This means that out of the 9 false binaries in our sample, 6 are located in this bin. The bins with the larger separations have a larger number of false binaries, as expected. The errors are indicated by the straight lines and were calculated assuming a binomial distribution.

Using our whole range of separations we have a binary fraction of (8.8±1.1)%, while using data from DM91, in the same range of separations, we estimated a binary fraction of 13.7% and 12.4%, using a trapezoidal approximation and a linear interpolation, respectively. It was necessary to convert the periods given by DM91 to angular separations. Since the stars analyzed by DM91 are solar-like stars (F9-G6 V) we assumed a typical G2V spectral class and transformed the periods to separations. Hence, the field has a binary fraction 1.5 higher than ONC.

2.5.3 Wide versus Close Binaries

Is there a difference between the number of wide binaries and close binaries? Previous studies (e.g. Köhler et al., 2006) tried to find such difference without success. The dramatic change in the separation distribution function seen in the left panel of Fig. (2.7) lead us to choose this separation as a dividing point. Binaries with angular separation in the range $0\farcs15 \leq$ separation $\leq 0\farcs5$ are called "close" and binaries with angular separation in the range $0\farcs5 <$ separation $\leq 1\farcs5$ are called "wide".

To study the distribution of these systems as a function of separation to θ^1 Ori C we build cumulative distributions like the ones shown in Fig (2.8). The left panel shows a simple cumulative distribution as a function of distance to θ^1 Ori C, created by adding up the close and wide binaries as the distance to θ^1 Ori C increases, in steps of $1''$. We can see in this figure that there are close and wide binaries distributed in the whole range of distances. This means that

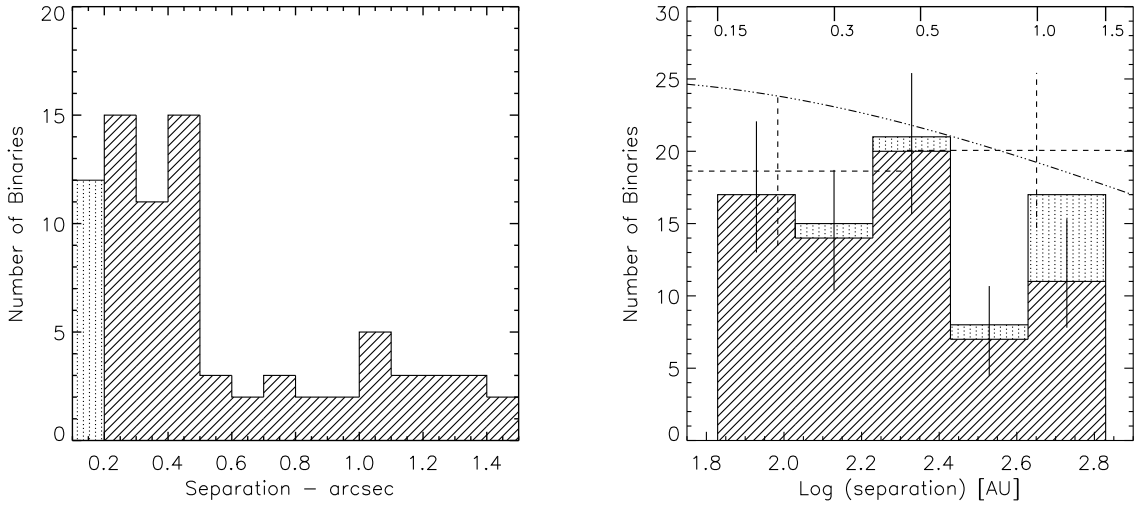

Figure 2.7: The left panel shows the histogram of binary angular separations in steps of 0.″1. The number of binaries in the innermost bin, with separations less than 0.″1, is incomplete. We filled this bin with vertical dotted lines. One can see the abrupt decrease in the number of binaries when the separation increases beyond 0.″5. The right panel shows the logarithmic separation distribution function of the ONC binaries compared to the distribution of field binaries from Duquennoy & Mayor (1991) across the separation range from 0.″15 to 1.″5. The dot-filled part of the histogram bins represents the contamination by line-of-sight pairs, obtained using Eq. (2.1). The bins representing large separations are the most contaminated ones, as expected. The vertical solid lines present in each bin represent the 1-σ errors calculated using a binomial distribution. The data from DM91 within our separation range are shown as two dashed crosses, while the Gaussian distribution they fit to their complete data set is represented by the dash-dotted line, which can be seen above the histogram. The top axis indicates separations in arcseconds at the distance of the ONC.

close binaries are not exclusive of the center regions and that we can detect wide binaries close to the center as probably as far from it. However the distributions are not the same.

The right panel in Fig. (2.8) shows a different situation. Here we have the ratio of wide to close binaries as a function of distance to θ^1 Ori C. The cumulative distribution function was calculated in the following manner: the first point was calculated dividing the total number of wide binaries by the total number of close binaries with distances to θ^1 Ori C, starting in the exclusion zone and going up to 30″ from it (the exclusion zone is at 60″ from θ^1 Ori C, which means that the first step used stars with distances from θ^1 Ori C in the range 60″ to 90″), the next step increased the distance in 1″ and made the same calculation. In this way, as the curve moves away from θ^1 Ori C it accounts for more and more binaries until it reaches the end of the distribution, where we have the mean ratio of wide-to-close binaries for the ONC. In the figure, the dashed lines indicate the 1σ errors and the dotted lines indicate the same ratio for the DM91 binaries, assuming a Gaussian fit (lower line), and the actual data points (upper line). The DM91 lines represent the ratio for field stars.

It is evident that there is a very pronounced and almost monotonic change in the ratio of wide-to-close binaries as one moves away from the core of the ONC until a distance of about 460″, at which point the ratio becomes flat. It is also clear that the mean ratio of wide-to-close binaries for the whole ONC is lower than DM91 values.

The separation distribution function in the ONC most probably has not yet found its final shape. Two classic mechanisms operate that can affect the orbit of a young binary: rapid dynamical decay in small-N clusters (e.g. Sterzik & Durisen, 1998; Reipurth & Clarke, 2001;

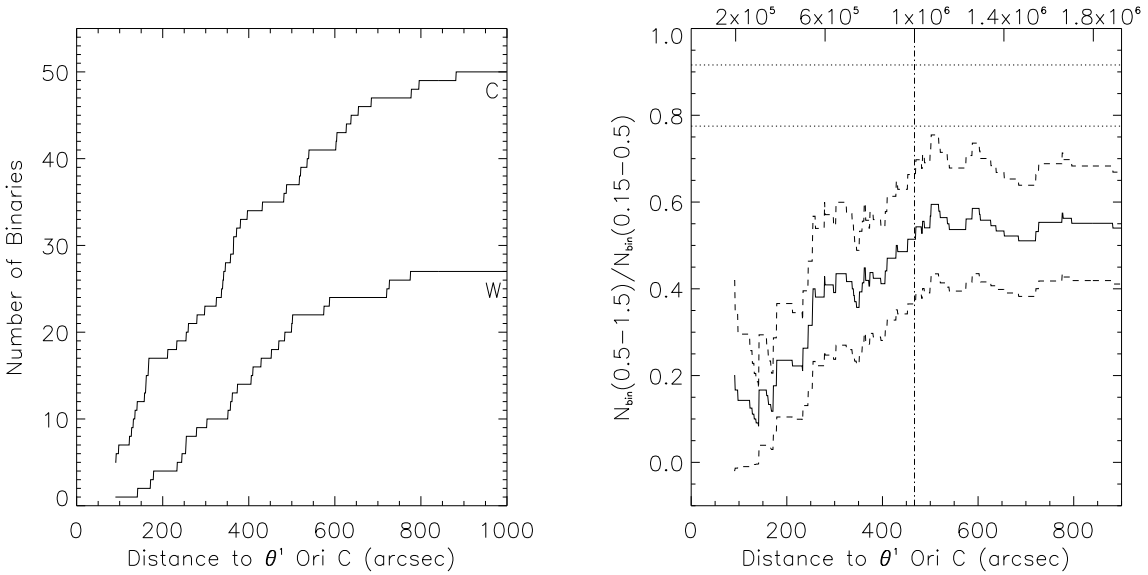

Figure 2.8: The left panel shows the cumulative distributions of close (0.″15 – 0.″5) and wide (0.″5 – 1.″5) binaries in the ONC as a function of distance from θ^1 Ori C. The right panel shows the ratio of wide to close binaries in the ONC as a function of distance to θ^1 Ori C. The dashed lines indicate the errors. The dotted horizontal lines at the top of the panel are the same ratio from the DM91 field binary study. The lower line comes from their Gaussian fit and the upper line comes from their actual data points. The top axis scale shows the crossing time in years, assuming a mean one-dimensional velocity dispersion of 2 km s^{-1}. The vertical dot-dashed line indicates the distance where the ratio becomes essentially flat, suggesting an age for the ONC of about 1Myr.

Bate, Bonnell & Bromm, 2002) and the passage of a binary through a dense cluster (e.g. Kroupa, 1995a,b, 2000; Kroupa, Petr & McCaughrean, 1999). The former occurs primarily during the Class 0 phase (Reipurth, 2000) and is no longer relevant for stars in the ONC. The latter, however, may be essential for understanding the binary population of the ONC. A wide binary falling through the potential well of a cluster will gain kinetic energy through encounters and binaries with weak binding energies are eventually disrupted (Heggie, 1975). A prediction of this scenario is that binaries at distances from the cluster center larger than the corresponding crossing time should not show any dynamical alterations due to encounters with other cluster members (Kroupa, Petr & McCaughrean, 1999; Kroupa, Aarseth & Hurley, 2001). The crossing time of a star through a cluster is $t_{\rm cross} = 2R/\sigma$, where R is the cluster radius and σ is the mean one-dimensional velocity dispersion in the cluster. Assuming that this velocity dispersion in the ONC is of the order of 2 km s^{-1} (e.g. Jones & Walker, 1988), we have indicated in the right panel of Fig. (2.8) the crossing time for different distances to the cluster center. The figure suggests that for distances larger than roughly 460″ there is no longer a measurable change in the ratio of wide-to-close binaries. Given that the wide-to-close binary ratio changes by a factor of 4–5 from the inner to the outer regions, this suggests that many, and perhaps most, of the wide binaries are disrupted after only a few passages by the cluster center. The variation of the ratio of wide-to-close binaries from the inner to the outer regions of the ONC offers the first compelling observational evidence that dynamical interactions in the dense central region of the ONC have taken place.

In principle, the right panel in Fig. (2.8) allows us to determine the age of the ONC. An angular distance of ∼460″ corresponds to a crossing time of about 1 million years. However, an age determined in this manner is directly dependent on the velocity dispersion assumed.

Therefore, all we can say about the age of 1 million years we estimate for the ONC is that it is consistent with other ONC age estimates (e.g. Hillenbrand, 1997).

The significantly lower numbers of binaries that we find in the ONC compared to associations thus appears to be due, at least in part, to the dissolution of wide binaries. However, under certain circumstances, an encounter could lead to hardening of the binary, making it closer than our resolution limit, so it is not lost to the overall binary budget.

Even in its outermost regions, the ONC shows a smaller ratio of wide-to-close binaries than seen in the field by DM91. Considering that the majority of field stars are likely to have been formed in a cluster, it follows that many of the wide binaries in the field must have formed in the gentler environment of a loose T association.

Durisen & Sterzik (1994) found, on theoretical grounds, that binaries are more likely to form in clouds with lower temperature. Reipurth & Zinnecker (1993) found observational evidence that clouds with more stars have relatively fewer binaries in the separation range under study (mostly wide visual binaries). Both of these results indicate that loose T associations produce or retain more wide binaries than clusters do. However, Brandeker et al. (2006) noted that the young sparse η Chamaeleontis cluster has a deficit of wide binaries. Unless this small cluster is the remnant of a much denser cluster, this result would seem to be in contradiction to the notion that wide binaries are preferentially formed/preserved in loose associations. In any case, there is no question that the field binary population is a mixture of binaries formed in clusters and in associations.

2.5.4 Flux Ratios and Substellar Companions

We have determined the flux ratios of the unsaturated binaries and present a histogram as a function of Δmag in Fig. (2.9).

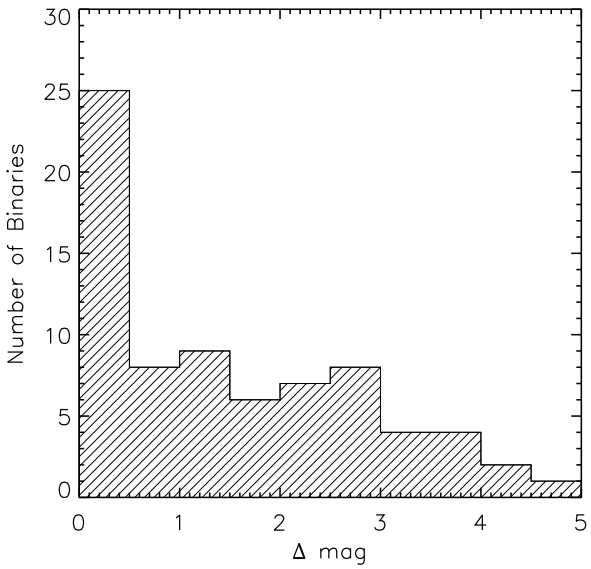

Figure 2.9: Luminosity ratio of the binary population, based on the Hα fluxes of primaries and secondaries. All binaries with separation between $0\farcs1$ and $1\farcs5$ are plotted, except the saturated ones.

The majority of the binaries in the ONC have unequal components, although the bin with equal components ($\Delta m < 0.5$ mag) is the most populated. Only very few of the companions have a magnitude difference between the primary and the secondary of more than 3 mag.

In the absence of spectroscopic information, we have made a crude attempt to investigate the nature of the companions based on their measured flux ratios. In order to do that we have made some assumptions. First, we assume that the observed flux ratios reflect photospheric fluxes, in other words, that Hα emission-line fluxes are not seriously affecting the ratios. This may not always be a good assumption, since mid-to-late M dwarfs often are very active and their photospheric fluxes are so low that Hα line emission could be a significant contribution. If we mistake Hα line emission for photospheric flux from the primary, our estimate of a spectral type for a companion will be earlier than it really is.

Second, most published photometry of late-type dwarfs is broadband, whereas we have observed in the narrow band Hα filter, so we assume that our observed magnitude differences can be compared to R-band photometry. Since we are dealing with the difference between two stars, this is probably not a bad assumption, at least when the flux ratio is not large.

Third, we assume that the observed flux ratios are not affected by differences in extinction between the components. Given the young age and occasional association with molecular clouds, this may not hold true in all cases.

With these caveats spelled out, we have used the M_I versus spectral type relation and the $R - I$ colors for M dwarfs (Dahn et al., 2002) to derive the difference in R-band magnitudes as a function of spectral type for M dwarfs. The relation turns out to be essentially linear, with a mean drop of 0.56 mag per spectral subtype throughout the M spectral range, as can be seen in Fig. (2.10). We then used the spectral classifications for the primaries provided

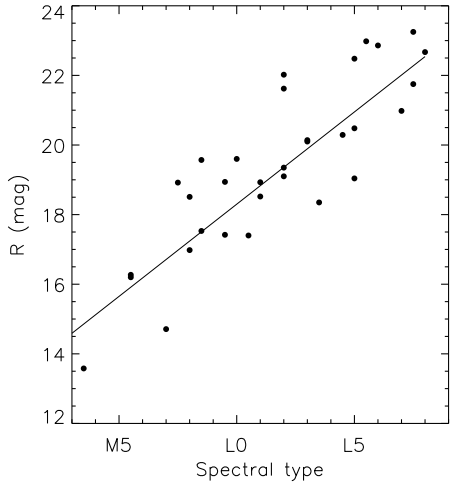

Figure 2.10: R-band magnitudes as a function of spectral type for M dwarfs and very cool objects (spectral type L).

by SIMBAD, of mixed provenance, with our flux ratios to estimate a spectral type for the secondaries. For a cluster with an age between 0.5 and 3 million years, the substellar limit is

around spectral type M6.25, following the models of Baraffe et al. (1998) and Chabrier et al. (2000) and using the temperature scale of Luhman et al. (2003, 2006). To our surprise, quite a number of the secondaries appear to be brown dwarfs, in at least one case forming a wide brown dwarf-brown dwarf binary. Given the assumptions involved and the simplistic nature of these spectral type estimates, it is obvious that spectroscopy is required to establish the true nature of the secondaries. These brown dwarf and very low mass systems are very important to the study of the low-mass end of the initial mass function. The detection of such objects in binary systems is also very important for evolutionary and star formation models.

2.6 Summary of Results

We have analyzed a large set of Hα images of the ONC acquired with the ACS onboard the HST with the goal of detecting binaries among a sample of 781 ONC members. The following results were obtained:

1. A total of 75 binaries and 3 triple systems were detected, of which 55 are new discoveries.
2. Within the limited angular range of $0\farcs15$ – $1\farcs5$, corresponding to projected separations of 67.5 – 675 AU, we have found a binary fraction of (8.8±1.1)% after correcting for a statistically determined contamination of nine line-of-sight binaries.
3. The field binary fraction for solar-type stars in the same separation range is 1.5 times larger and for T Tauri associations it is 2.2 times larger than in the ONC, confirming with more significant data the earlier results that the ONC is deficient in binaries.
4. The separation distribution function for young binaries in the ONC shows a dramatic decrease in binaries for angular separations larger than $0\farcs5$, corresponding to projected separations of 225 AU.
5. The ratio of cumulative distributions of wide to close binaries shows an increase out to a distance of about $460''$ from the center of the ONC, after which it levels out. We interpret this as clear observational evidence for dynamical evolution of the binary population as a result of passages through the potential well of the ONC. These results are consistent with an age of the ONC of about 1 million years.
6. It appears that, at least in part, the deficiency of binaries in the ONC compared to the field star population, can be understood in terms of the destruction of wide binaries combined with a secondary effect from orbital evolution of binaries toward closer separations that are unobservable in direct imaging surveys.
7. Limited spectral information about the primary stars indicated that they are low-mass T Tauri stars, except for one Herbig Ae/Be star. Assuming that most binaries are not affected by differential extinction, we find that possibly as many as 50% of the binaries have companions with spectral types later than M5 and from one-sixth to one-third of the binaries may have substellar companions, all of which have separations of at least 50 AU. This large number of wide substellar companions is of interest for theories of brown dwarf formation.

The environment of the loose T associations seems to favor the survival of the wide binary population, while the dense environment of the star forming regions like the ONC, seems to be responsible for the disruption of part of these wide binaries. It is reasonable to suppose

that the wide binaries (mainly the late-type ones) that populate the field were born in loose T associations and therefore survived, while the single late-type field stars were born in multiple systems in dense star forming regions, which were disrupted after some close encounters in their dense environment. Thus, regions like the ONC would contribute with single stars to the field population, while T associations (like Taurus-Auriga, Lupus, Ophiuchus, etc) would contribute with multiple systems, as well as with single stars.

The discovery of visual binaries, in a star forming region like the ONC, is very important because we can try to determine precise stellar parameters of young stars. Although the ONC is ∼450 pc away, astrometric observations of these binaries, with the ACS onboard the HST for example, can be used to determine their projected orbit and in this way obtain mass, radius, etc. Similar studies have already been conducted for other visual binaries (e.g. Chauvin et al., 2005; Neuhäuser et al., 2008).

2.7 Individual Binaries of Interest

Below, we describe some of the interesting objects. We will assume that the difference in magnitude between primary and seconday is not affected by extinction differences.

V1438 Ori (JW 39). The spectral type of M3 is from H97. The 2.6 mag difference implies that the companion is an M8 brown dwarf at a projected separation of 170 AU. Stassun et al. (1999) detected lithium in the system.

JW 71. The spectral type of M4 is from H97. The 1.4 mag difference implies that the companion is an M7 brown dwarf with a projected separation of 90 AU.

V1118 Ori (JW 73). This is a member of the EXors class (Herbig, 1989). The star, which is also know as Chanal's Object, has had five outbursts since its discovery in 1984 and typically varies within the range $14.5 < V < 18$, with a rise time of less than a year and a declining phase about twice as long. Optical and infrared spectroscopy of V1118 Ori is reported by Parsamian, Mujica & Corral (2002) and Lorenzetti et al. (2006), and x-ray observations are analyzed by Audard et al. (2005). The discovery that V1118 Ori has a companion only 0.4 mag fainter in the Hα filter raises interesting questions about which of the components may drive the variability (Herbig, 2008).

JW 121. The spectral type of M3 is from H97 and the 3.0 mag difference implies that the companion is an M8 brown dwarf with a projected separation of 153 AU.

JW 147. The spectral type M5 is from H97 and the 1.4 mag difference implies that the companion is an M8 brown dwarf with a projected separation of 135 AU.

JW 152. The spectral type of M3 is from H97 and the 2.5 mag difference implies that the companion is an M7 brown dwarf with a projected separation of 81 AU.

JW 235. It is associated with object HH 504, discovered by Bally & Reipurth (2001); see also O'Dell (2001). The binarity of the star was discovered by Köhler et al. (2006). Its proper motion in the JW catalogue implies that it has a very low probability of being a member of the ONC. However, given similar brightness of the two components (0.4 mag), it is likely that brightness variations of the stars shifted the photocenter used for astrometry. Evidence for ONC membership is strong and is based on the presence of Hα emission, detection in X-rays, optical variability and association with an HH object.

V1274 Ori (JW 248). The spectral type of the primary is somewhat in dispute. H97 suggests M0.5-M2 (with the Ca II lines in emission), Edwards et al. (1993) suggest M3 and Meeus & McCaughrean (2005) suggest M0-M4. The binarity of the system was found by the COUP survey. Our primary is the secondary in the COUP catalogue, indicating that our secondary is highly X-ray active. Sicilia-Aguilar et al. (2005) detected lithium in the (optical) primary and found an inverse P Cygni profile at Hα. If there is not an extinction difference between the primary and the secondary, then the large flux difference (> 3.7 mag) suggests that the companion could be an L0 brown dwarf. However, the system is only $3'$ from θ^1 Ori C, so there is a 1% chance of a line-of-sight association.

JW 296. It is the primary of a hierarchical triple system. The secondary and tertiary are very faint stars, surrounded by a common proplyd-like envelope know as 066-652 (O'Dell & Wong, 1996). The primary is of spectral type M4.5 according to H97 and if the brightness difference is taken at face value, the secondary and tertiary should be L0 brown dwarfs. Although, given the obvious association with nebulosity it is likely that their faintness is merely due to extinction.

JW 355. The primary of this system is located at the edge of a proplyd known as 109-246 (O'Dell & Wong, 1996). The proper motion of the star suggests it is not an ONC member but it is found to be a member by the COUP project. H97 suggests a mid-K spectral type. The system is only $90''$ from θ^1 Ori C and the star density is so high that the possibility of a line-of-sight association is several percent.

JW 370. There is a silhouette disk close ($\sim 3\farcs4$) to this binary. Given the local density of stars around this system, the probability that such a silhouette disk is just a chance alignment is $\sim$7%. The chance of a line-of-sight alignment for the binary itself is 1.5%. H97 suggests a spectral type of K0-K3.

V1492 Ori (JW 383). The primary is of spectral type M3 according to H97. The 2.1 mag brightness difference implies that the companion is an M7 brown dwarf with a projected separation of 86 AU. Stassun et al. (1999) derived a rotation period of 7.11 days for the primary and noted the presence of lithium in the spectrum.

Parenago 1806 (JW 391). The primary is of spectral type M1 according to Edwards et al. (1993) and H97, who also noted the presence of Ca II emission. The primary is saturated in our images, but with a magnitude difference of at least 3.3 mag, the companion will be an M7 brown dwarf. However, the pair is located in a region of high stellar density, so the probability of a chance alignment is more than 5%.

JW 509. This binary was first detected by Prosser et al. (1994) and subsequently by Padgett, Strom & Ghez (1997) and Lucas, Roche & Tamura (2005). Although it is a well known binary it does not have a spectral type in the literature. Since this system is located in a crowded region, the probability of a chance alignment is $\sim 2.7\%$ but the reality of the binary is supported by an interaction zone between the stars, visible in our Fig. (2.3), first row, third stamp.

Parenago 1914 (JW 551). The primary of this hierarchical triple system has a spectral type M1 according to H97. The tertiary is not detectable either in the optical or in X-rays, and since its separation from the primary is as large as $1\farcs27$ it could be a background object. The system seems to be part of a small subcluster, which gives it a high probability of a chance alignment ($\sim$2.2%). Given the primary spectral type and the difference in magnitudes to the tertiary (3.6 mag) and assuming that the tertiary is not a background object, the tertiary could

have a spectral type of M7 or M8 and thus would be a brown dwarf candidate.

COUP 967. This star was catalogued as a binary by Prosser et al. (1994), Padgett, Strom & Ghez (1997) and Lucas, Roche & Tamura (2005). Our image shows that the primary is associated with a proplyd (184-427 in O'Dell & Wong (1996)) and the secondary is a faint object ($\Delta m_{H\alpha} = 2.4$). The spectral type for the primary is M2.5 according to H97. The system is very close to θ^1 Ori C ($\sim 70''$) and the probability of a chance alignment is 3.5%. If the components have the same extinction, then the secondary would be of spectral type M6.5 and thus at the hydrogen-burning limit.

JW 592. The spectral type is M2.5 according to H97 and M4 according to Edwards et al. (1993). The 4 mag difference implies an M9.5 spectral type or later for the secondary, making it a brown dwarf with a projected separation of ~ 275 AU.

COUP 1061. This very close system (~ 100 AU) has a combined spectral type M9-L0 according to Meeus & McCaughrean (2005), who did not resolve it, and since the components have virtually the same brightness (0.1 mag), this is a bona fide brown dwarf-brown dwarf binary with a projected separation of 100 AU.

V1524 Ori (JW 681). This binary was first catalogued by Prosser et al. (1994), according to which it has spectral type K7. The secondary is associated with the proplyd 213-346 (O'Dell & Wong, 1996). In the H97 catalogue this system has two entries, both with number 681 but with different coordinates. SIMBAD identifies three different objects: H97b 681, H96b 681a and H97b 681b. The first is JW 681, also known as V1524 Ori and is the primary in this pair. The second is the unrelated object MLLA 312 and the third is the X-ray source COUP 1149, which forms the secondary component, associated with the proplyd. Because this system is located near θ^1 Ori C ($\sim 77''$) the probability of a chance of alignment is 3.5%.

V1528 Ori (JW 727). The spectral type M2 is from H97 and the difference in brightness suggests a spectral type of L0 for the companion if the components have the same extinction. If so, the secondary is a brown dwarf with projected separation of 329 AU. The primary shows Hα emission according to our unpublished survey.

JW 748. This binary was discovered by Prosser et al. (1994) and the spectral type of the primary is M3 according to H97. Given the brightness difference the secondary could be a brown dwarf with spectral type M7 and a projected separation of 158 AU.

JW 767. First discovered by Köhler et al. (2006) this system has spectral type M2.5 from H97. The secondary has a silhouette disk and is associated with the object HH 668 (Bally et al., 2006). The extinction caused by the silhouette disk probably is responsible for the large difference in brightness of more than 4 mag between the primary and secondary.

Parenago 2075 (JW 867). This object was observed by Köhler et al. (2006) but despite its brightness and angular separation ($0\farcs29$) they did not resolve it, suggesting possible major variability of the secondary. The system presents evidence of Hα emission, X-rays and optical variability. A spectral type of M1 was suggested by Blanco (1963) and more recently Duncan (1993) assigned a spectral type of K8 Ve. Sicilia-Aguilar et al. (2005) reported lithium in the spectrum of the primary.

JW 906. The primary has spectral type M3 according to H97 and the 2.7 mag difference implies that the secondary is a brown dwarf with spectral type M8 and a large projected separation of 625 AU. Sicilia-Aguilar et al. (2005) reported lithium in the spectrum of the primary.

Chapter 3

Variability

3.1 Introduction

Variability is an inherent characteristic of the stars. We can say that all stars are variable, in different stages of their lives, with different amplitudes and time scales. During its lifetime, a star travels along different paths in an HR diagram because it presents different characteristics. However, it is impossible for us to observe a star as it evolves from its parental cloud, through the main sequence towards its final moments as a white dwarf, a neutron star or even a black hole. What we can do is study different stars in different evolutionary stages and try to put the puzzle together in a coherent frame.

We will call "variable stars" those which present brightness variability in a time scale that we can measure, be it seconds, days, years or decades, with amplitudes that we can measure using CCDs, photometers or even photographic plates. The time scale, shape of the light curve and amplitude of the brightness variations can be used to classify variable stars. Spectral type, luminosity class and chemical composition are also important parameters to help us classify the stars according to the origin of the variations.

Variable stars can be divided into two major groups: intrinsic variables and extrinsic variables. Intrinsic variable stars are those that vary due to physical processes in the star itself, while extrinsic variable stars are those that vary due to processes external to the star.

Examples of intrinsic variables are the pulsating variables (there are many kinds of pulsating variables, young ones, old ones, dying ones) and the eruptive (or explosive) variables (flare stars, novae, supernovae). Extrinsic variables are, for example, eclipsing variables (the eclipse may be due to a companion star, a planet or even the circumstellar material in young or very old systems) and rotating variables (which include pulsars).

It must be clear that one kind of variability does not exclude the other. We can have, for example, an eclipsing pre-main sequence star in which one of the components (or even both) presents pulsations.

3.2 Types of Variables

The variable stars we are mainly interested in are the eclipsing binaries, irregular, pulsating pre-main sequence and rotating variables. The light curve of some eclipsing binaries is very different from other variables, because it presents itself constant except for its minima. The light curves for irregular variables cannot be classified or grouped in any class, hence their name. The pulsating and rotating variables can present very similar light curves and can be misclassified if one uses only the shape of the light curve as a parameter for classification. Stellar properties like the spectral type, luminosity class, etc, can help us distinguish between these two groups. The four groups, listed above, have different characteristics and statistical indices can be used to separate the sample.

Absolute parameters such as radius, mass and temperature with high precision ($\leq 1\%$) can only be obtained for spectroscopic eclipsing binary stars and are very important for putting constraints on the models of star formation and evolution. There are only 22 pre-main sequence stars in the literature, with absolute parameters that are well determined, through the use of dynamical techniques (Mathieu et al., 2007; Stassun et al., 2008). The discovery of more pre-main sequence eclipsing binaries is in demand.

Given that pre-main sequence stars (T Tauri and Herbig Ae/Be stars) still possess material from their original environment and some of them are still accreting and/or ejecting matter, the probability of finding a star with irregular photometric variability is quite high. Young stars can also present flares which will cause an increase in brightness or present drops in brightness caused by some obscuration in the line of sight. The physical cause of such events can be, for example, the accreting material.

Spots on the photosphere of a star can also cause drops in the brightness. If we add to it the rotation of the star, we end up with a modulation in the light curve that can be related to the period of rotation. Many young stars in the Orion Nebula have their period determined in that way (e.g. Rebull, 2001).

A few years ago pulsating pre-main sequence stars got the attention of the astronomical community (Kurtz & Marang, 1995). These stars occupy a locus in the HR diagram known as the instability strip, where many post-main sequence pulsating stars are also observed. These variables are important for studying the interior of young stars and the determination of pulsation modes and periods. They can be used as constraints to evolutionary models.

It is impossible to predict what kind of variable stars we will find in the Orion Nebula and Cygnus OB2 surveys. We will probably have a mixture of different types.

3.3 Statistical Indices

In order to distinguish between different types of variability it is necessary to use some statistical indices. Some of them can be applied directly to the light curve of a star, while others are suitable to be applied to residual curves or even to mean values. In this work we will use the following set of statistical indices:

1. mean magnitude;
2. standard deviation;
3. geometric deviation;

4. mean absolute deviation;
5. absolute value of the maximum amplitude variation;
6. maximum deviation from mean magnitude;
7. R-statistics;
8. skewness;
9. kurtosis.

1 - Mean magnitude:

$$\overline{m} = \frac{1}{N}\sum_{i=1}^{N} m_i \tag{3.1}$$

The mean magnitude of each object is obtained through a simple mean involving all detections. It is used in other statistical indices, like the standard deviation, geometric deviation, mean absolute deviation, maximum deviation from mean magnitude, R-statistics, skewness and kurtosis. We will see later that the study of the mean magnitude curve can help us in the characterization of variable stars.

2 - Standard deviation:

$$\sigma = \sqrt{\frac{1}{N-1}\sum_{i=1}^{N}(m_i - \overline{m})^2} \tag{3.2}$$

where N is the number of detections, m_i is the differential magnitude in the ith frame and $\overline{m}$ is the mean magnitude. The standard deviation is useful in the detection of measurements that clearly stand out of the normal behavior of the star. It is sensitive to large variations.

3 - Geometric deviation:

$$\sigma_g = \exp\left(\frac{1}{N}\sum_{i=1}^{N}\ln|m_i - \overline{m}|\right) \quad \text{if} \quad |m_i - \overline{m}| \geq 0.001, \tag{3.3}$$

as in Eq. (3.2), N is the number of detections, m_i is the differential magnitude in the ith frame and $\overline{m}$ is the mean magnitude. The geometric deviation is the geometric mean of the absolute deviations greater than 0.001. The geometric deviation is sensitive to small variations and it is useful to detect constant stars. The smaller the deviation is from the mean, the smaller the value of the geometric deviation is and that is the reason why we have set a limit of 0.001 to the variation of the measurements. We can see in Eq. 3.3 that if the measurement is equal to the mean magnitude we will have a null value in the argument of the neperian logarithm.

4 - Mean absolute deviation:

$$\sigma_{abs} = \frac{1}{N}\sum_{i=1}^{N}|m_i - \overline{m}|. \tag{3.4}$$

The mean absolute deviation is defined as the simple mean of the absolute deviations. In Eq. (3.4), N is the number of detections, m_i is the differential magnitude in the ith frame and $\overline{m}$ is the mean magnitude.

The standard deviation (σ) is very sensitive to very different values of the magnitude while the geometric deviation (σ_g) behaves in the opposite sense, it is not sensitive to great differences but it is sensitive to small differences. The geometric deviation is ideal to search for constant stars. The mean absolute deviation (σ_{abs}) has a value between the standard deviation and the geometric deviation. We can use it in stars that are not constants and also that do not present great variations.

5 - Absolute value of the maximum amplitude variation is exactly what its name indicates, it is the maximum variation among all the detections. It is useful to detect stars with great variations.

6 - Maximum deviation from mean magnitude: yields the largest difference among the detections of an object and its mean magnitude, it can be positive or negative. It is useful to separate flare stars from eclipsing binaries.

7 - R-statistics:

The R-statistics (R from residuals) was introduced by Baptista & Steiner (1993) and improved by Bruch (1999). It is an adimensional number that measures the systematicity of a set of residuals, being zero if the data has a random distribution around its mean value, close to 1 if the data has a systematic behavior and close to -1 if the data has systematic deviations alternating between positive and negative.

$$R = \frac{1}{N-1}\sum_{i=2}^{N}\frac{(m_i - \overline{m})(m_{i+1} - \overline{m})}{\sigma_{\text{res}}^2}, \tag{3.5}$$

where N is the number of detections, m_i is the differential magnitude in the ith frame, $\overline{m}$ is the mean magnitude and σ_{res} is the standard deviation of the deviations $(m_i - \overline{m})$ shown by the object's measurements (σ_{res}^2 measures the variance of the residuals). If we have a statistically significant number of measurements then R can be associated with the probability of the deviations being systematic or random. If a star presents periodic variability, the R-statistics value should be close to -1, indicating that the star's brightness oscillates about a mean value.

8 - Skewness:

$$\gamma_1 = \frac{\mu_3}{\sigma^3}, \tag{3.6}$$

where μ_3 is the third moment about the mean and σ is the standard deviation. Skewness is useful to indicate if deviations from the mean are positive or negative. The moment about the mean (μ_k) for a random variable X is defined as:

$$\mu_k = \overline{(X - \overline{X})^k} \tag{3.7}$$

Distributions with negative skewness have left tails longer than right tails while distributions with positive skewness have right tails longer than left tails. Usually the models assume that data points have a normal distribution, meaning that they are symmetric about the mean and the skewness is zero. In reality the data point distribution is not symmetric and the skewness can help us determine how the data is distributed about the mean. If a star has negative skewness it implies that the measurements showing high deviations are located in the left tail, which means lower magnitude values (the star is brighter). A star that has a positive skewness presents the

measurements with high deviations in the right tail, which means higher magnitude values than the mean (the star is fainter). We expect to see eclipsing binaries with high positive skewness values.

9 - Kurtosis:

$$\gamma_2 = \frac{\mu_4}{\sigma^4} - 3, \tag{3.8}$$

where μ_4 is the fourth moment about the mean and σ is the standard deviation. The minus 3 is a correction to make the kurtosis of the normal distribution equal to zero. There is a lower limit of -2 for the kurtosis, but there is no upper limit, it could in fact be infinite.

Kurtosis is a measure of whether the data is peaked or flat relative to a normal distribution, which has kurtosis equal to zero. A positive kurtosis means that the distribution in question has a sharper peak around the mean than the normal distribution. In other words, the values around the mean have a higher probability than in a normal distribution. A negative kurtosis means that the distribution has a less acute peak around the mean, the values around the mean have a lower probability than in a normal distribution. The Laplace distribution, for example, has a positive kurtosis while the discrete and continuous distributions have negative kurtosis.

Stars with irregular variability will present a kurtosis value lower than stars with well defined variability, for example, eclipsing binaries. Because the detached eclipsing binaries spend most of their time with a constant magnitude, their kurtosis tend to have high values.

3.4 Testing the Indices

In an attempt to see the effect of different types of variability in the statistical indices we will use real light curves, obtained by the All Sky Automated Survey[1] (ASAS) (Pojmanski, 1997). We will use light curves of α^2 Canum Venaticorum stars, Cepheids, δ-Scuti stars, detached eclipsing binaries, RR Lyrae stars and unknown type variables.

Figure (3.1) shows an example of typical light curves for each of these six variable types. The period (in days) for each star is indicated in the panels. The ASAS gives the V band magnitudes and the periods, which we used to construct these phase diagrams. The last panel shows a variable star of unknown type, with a trial period indicated by the ASAS database.

We selected five stars from each variable type and an IDL routine was written in order to calculate the statistical indices for the whole sample. The statistical index values for all the variable stars are presented in Table (3.1). The first column presents the object's mean magnitude, while the period in days is shown in the second column. The σ, σ_g and σ_{abs} are shown in columns 3, 4 and 5. The R-statistics is shown in the sixth column while the seventh column shows the empiric discovery probability (ω). The skewness and kurtosis are presented in columns 8 and 9.

It is possible to see that the final values of skewness and kurtosis of the eclipsing binaries are always positive and larger than 1.0, as we expected, while the final values of the same indices for the RR Lyrae variables are always negative, except for the skewness value of the third star. All the Cepheid stars present negative kurtosis, an indication that the measurements are more scattered about the mean. The only other variable class that presents similar statistical indices

[1] http://www.astrouw.edu.pl/asas/

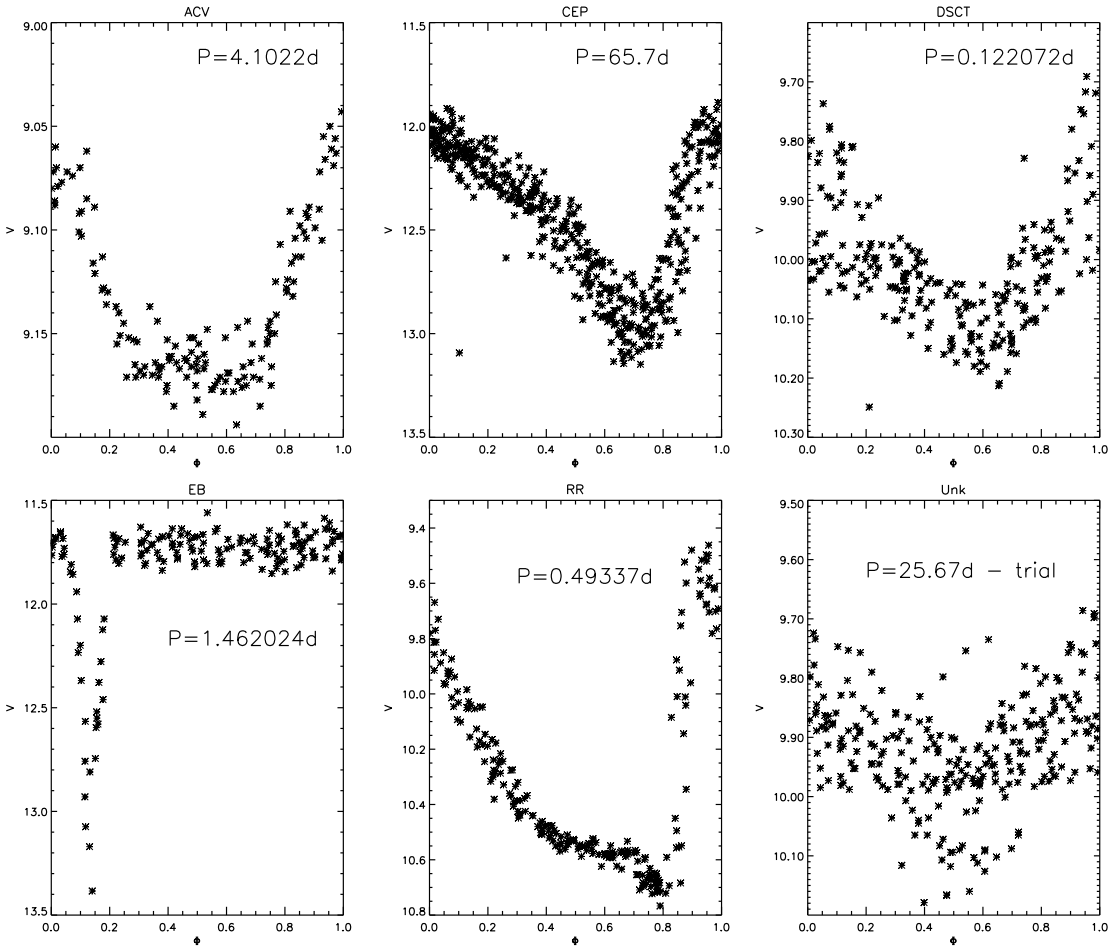

Figure 3.1: Examples of the light curves of the variables stars used to test the statistical indices. The plots show the star's V magnitude versus the phase. The period, indicated in each panel in days, was obtained in the ASAS database. Each panel has a label at the top indicating the variable type; starting in the first row we have the α^2 Canum Venaticorum (ACV), Cepheids (CEP), δ-Scuti (DSCT), eclipsing binary (EB), RR Lyrae (RR) and unknown type variable (Unk).

to the Eclipsing binaries is the δ-Scuti class, although some δ-Scuti show negative indices. This is an interesting feature since the light curves of these classes are completely different. The kurtosis of eclipsing binaries is expected to have high positive values because most of the time the star has an almost constant magnitude, only changing in the occurrence of eclipses. The R-statistics index for the unknown type variables presents values close to unity, meaning that these stars indeed present some systematic behavior. The skewness index, for the same class of stars, presents values close to zero, which are expected for a normal distribution of data points.

A very interesting behavior can be seen for Cepheids and eclipsing binaries. Their period seems to be correlated with the R-statistics value: the greater the period the higher the R-statistics value. However, after a more detailed study using a larger sample (18 stars) we concluded that there is no correlation between the period and the R-statistics.

All these values are obtained with the total light curve of each variable. In other words, they are static numbers that do not measure the dynamics of the variability. Instead of calculating these indices using the total light curve we will calculate them every time a new point is inserted in the database. In the end we will have not a light curve but σ-curves, σ_g-curves, and so on.

Table 3.1: Statistical index values for all the variable stars in the test sample.

Mag	P (d)	σ	σ_g	σ_{abs}	R	Skewness	Kurtosis
			α^2-Canum Venaticorum				
9.135	4.1022	0.0388	0.0262	0.0335	−0.1227	−0.6851	−0.8437
11.323	2.4734	0.0549	0.0273	0.0423	0.1440	0.1017	0.5296
10.424	1.1288	0.0458	0.0317	0.0401	−0.1126	−0.0143	−1.1253
9.023	2.0787	0.0326	0.0169	0.0263	0.1442	−0.3499	−0.4929
10.963	1.9038	0.0490	0.0269	0.0409	0.2035	0.2660	−0.6990
			Cepheid				
12.444	65.70	0.3429	0.2322	0.2989	0.7903	0.3982	−0.9581
13.583	29.09	0.3192	0.1893	0.2659	0.3487	0.6048	−0.2670
13.154	33.36	0.3603	0.2207	0.3031	0.6327	0.3068	−0.7508
11.316	2.21	0.2060	0.1159	0.1739	0.0062	−0.1843	−1.1133
13.468	22.33	0.3072	0.1832	0.2596	0.4726	−0.0579	−0.8913
			δ-Scuti				
10.014	0.122072	0.1051	0.0477	0.0791	−0.0085	−0.7398	0.3976
13.727	0.130639	0.2393	0.1134	0.1756	0.0135	−1.0912	10.4336
11.446	0.062784	0.3925	0.0653	0.1270	0.0071	8.6554	80.5066
11.644	0.194607	0.1352	0.0880	0.1161	0.0929	0.4668	−0.9158
9.725	0.091002	0.1361	0.0616	0.0873	0.1712	8.2930	136.6497
			Eclipsing Binary				
11.843	1.462024	0.3385	0.1190	0.2025	0.0291	2.9088	8.5518
11.723	0.46322	0.1623	0.0549	0.0981	0.0451	2.6532	7.2993
10.963	8.715623	0.0584	0.0161	0.0310	0.1552	3.9536	19.3385
11.690	11.045	0.1216	0.0557	0.0869	0.2483	1.6225	2.2106
8.768	2.0846	0.2882	0.0822	0.1180	0.1174	9.7805	111.6151
			RR Lyrae				
10.311	0.49337	0.3515	0.2320	0.2985	0.44994	−0.84352	−0.5270
12.257	0.52974	0.3126	0.2007	0.2611	0.02951	−0.70139	−0.2916
13.846	0.74407	0.2626	0.1485	0.2141	0.11214	0.38185	−0.3857
13.557	0.51716	0.3468	0.2119	0.2921	0.17726	−0.31978	−0.7885
10.169	0.49545	0.3835	0.2576	0.3319	0.69940	−0.57875	−0.9648
			Unknown Variable Type				
9.921	25.67	0.0914	0.0453	0.0702	0.7556	0.1622	0.3296
11.307	59.5	0.2791	0.1787	0.2382	0.9032	0.1945	−0.9385
9.543	43.1	0.1025	0.0518	0.0807	0.7095	0.0836	0.0484
11.755	100.6	0.1792	0.1200	0.1556	0.8183	0.1697	−1.0165
11.718	41.6	0.1757	0.0913	0.1350	0.8875	1.2236	1.0639

.

Figure (3.2) shows the statistical indices for the first α^2-Canum Venaticorum variable star. The values for the statistical indices calculated using the whole light curve are listed in the first row of the α^2-Canum Venaticorum section in Table (3.1). Starting in the first row of Fig. (3.2) we have, from left to right, the observed magnitude, the mean magnitude curve and the standard deviation curve. In the second row we present the mean absolute deviation curve, the skewness and the kurtosis curves applied to the magnitudes. The third row shows the skewness and kurtosis curves applied to the mean magnitude and the R-statistics curve. We can see clearly in these panels that the statistical indices are not static, they change along the observations. The deviations are more visible at the beginning of the curves and this can be easily explained by the fact that in the beginning we have few points to use in the statistic.

In this variable star we see a large variation in the mean magnitude at the beginning of

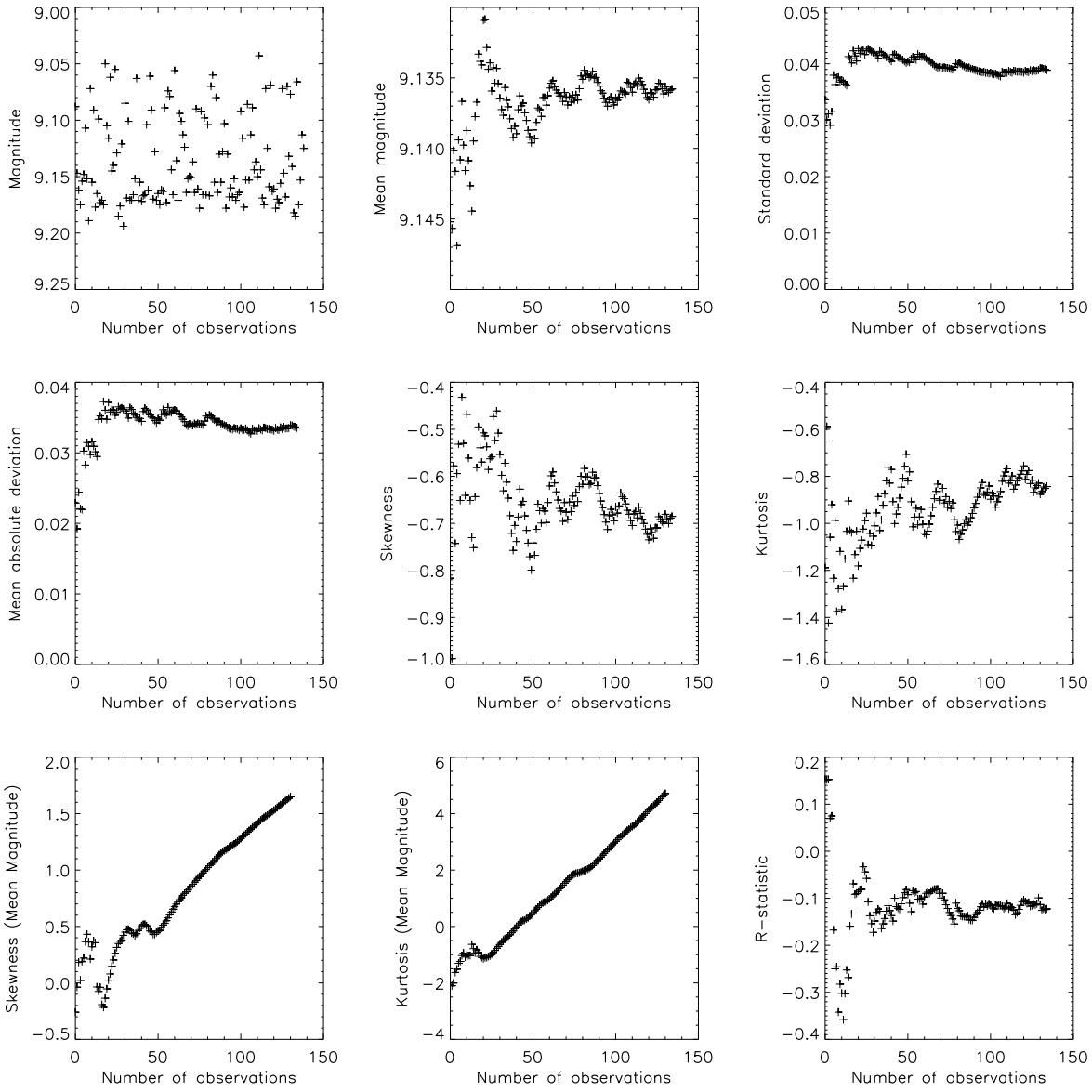

Figure 3.2: Statistical indices applied to an α^2-Canum Venaticorum type star as a function of time. In the first row we present, from left to right, the real light curve of the star, the Mean Magnitude curve and the σ-curve. The second row shows the σ_{abs}-curve, the skewness curve and the kurtosis curve. These last two curves were obtained using the magnitude of the object. The third row presents the skewness and kurtosis curves, obtained using the Mean Magnitude curve, and the R-statistics curve.

the observations, which continues, but with a smaller amplitude, throughout the observations. The σ and σ_{abs} decrease with time and they seem to reach a constant value at the end of the observations. Skewness and kurtosis applied to the magnitudes oscillate around a negative value without a clear tendency. On the other hand, the skewness and kurtosis applied to the mean magnitudes show a tendency to increase without apparent limit. An interesting feature can be seen in the beginning of the observations, where a decrease in the skewness curve correlates with the increase in the kurtosis curve. The R-statistics curve also shows large variations at the beginning but at the end seems to be oscillating around the final value.

Figure (3.3) shows the statistical indices applied to the light curve of the first Cepheid star in

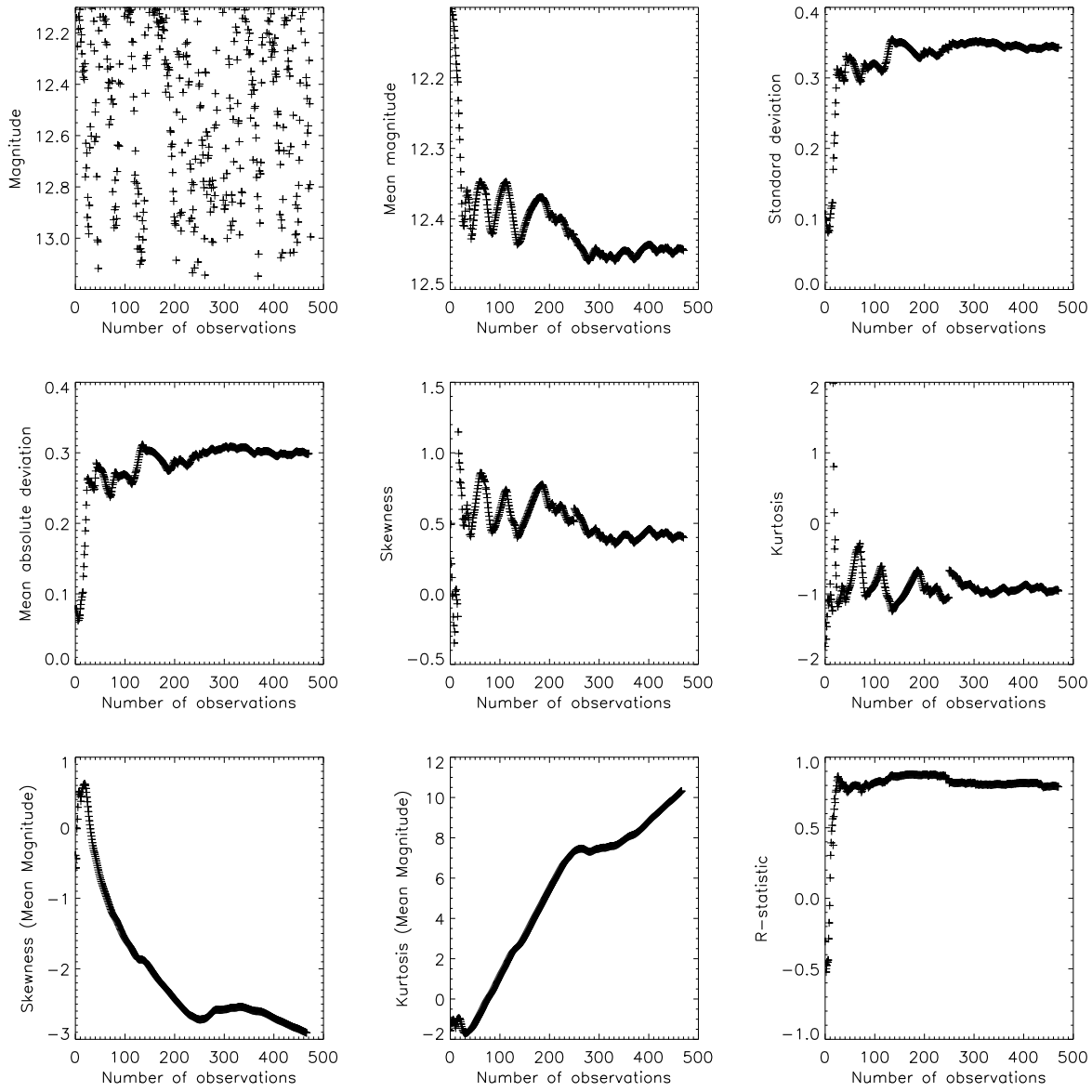

Figure 3.3: Statistical indices applied to a Cepheid type star as a function of time. The indices are the same as in Fig. (3.2).

Table (3.1). We can see large variations at the beginning of the observations but after some time the mean magnitude, the σ and σ_{abs} tend to a constant value. The skewness and kurtosis applied to the magnitudes still present small scale variations and oscillate around a final value. The skewness and kurtosis applied to the mean magnitudes present opposite behavior, the skewness decreases while the kurtosis increases, both without reaching a constant value. The R-statistics curve starts at ~ -0.5 and quickly reaches the value around which it will oscillate until the end of the observations ($\sim$0.8). The Cepheid variables show on average high values of R-statistics.

Figure (3.4) shows how the statistical indices evolve along the observations of the first δ-Scuti variable star in Table (3.1). The mean magnitude curve of the δ-Scuti star did not present a constant plateau, even after more than 200 measurements. The σ and σ_{abs} seem to have reached a constant value right at the beginning of the observations. The skewness curve began with a

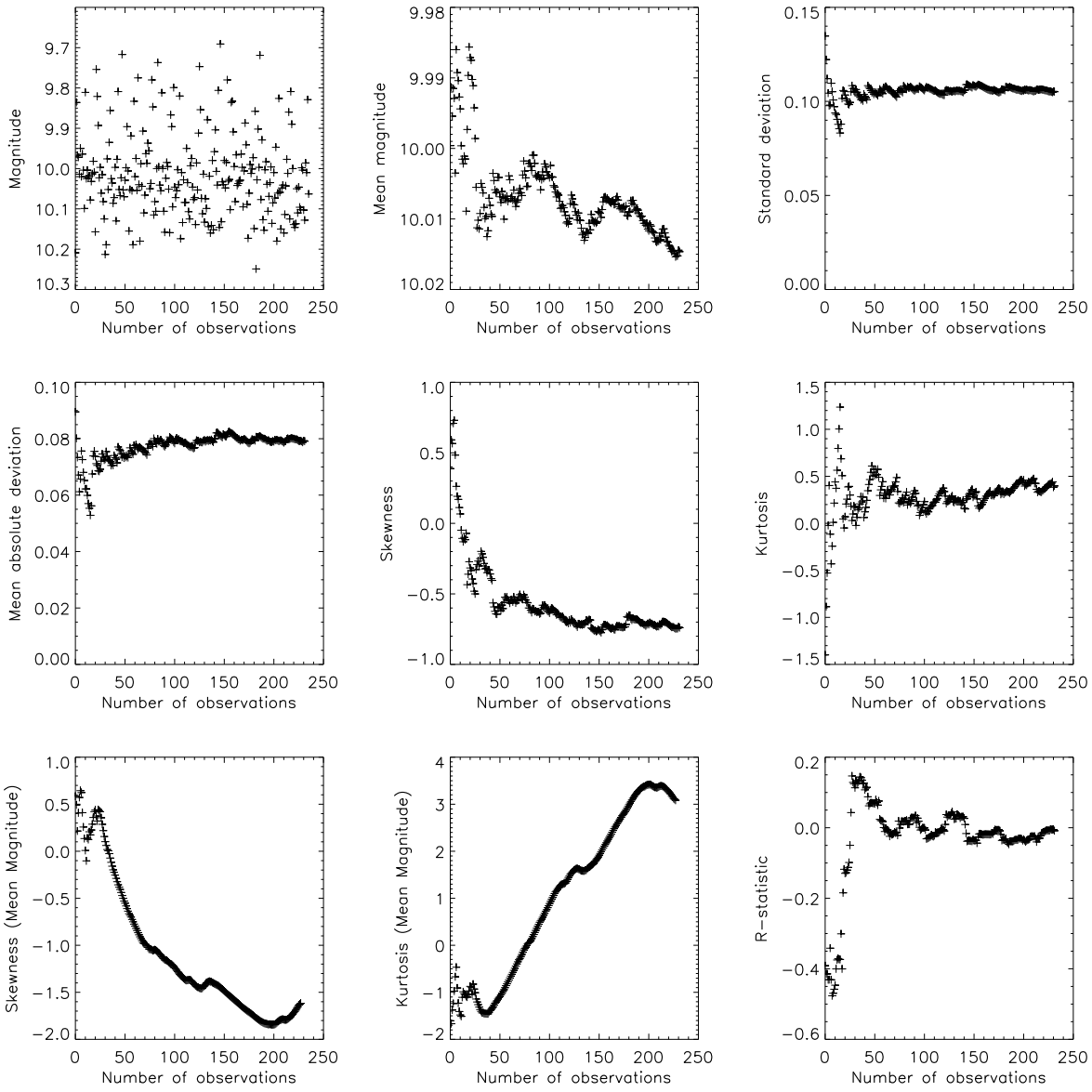

Figure 3.4: Statistical indices applied to a δ-Scuti type star as a function of time. The indices are the same as in Fig. (3.2).

high positive value, close to 1, and decreased to values around -0.5 after $\sim$50 observations, where it stayed almost constant until the end. The kurtosis shows more variations at the beginning but after some time it also stayed almost constant about a positive value. The skewness and kurtosis applied to the mean magnitudes present opposite behavior, like the Cepheid. The R-statistics curve presents a large variation at the beginning of the observations. It starts with value ~ -0.4 and after $\sim$30 measurements suffers a fast increase, reaching positive values. It presents some oscillations but with smaller amplitudes than at the beginning.

Figure (3.5) shows the same statistical indices but for the first eclipsing binary in Table (3.1). A peculiar fact about the statistical index curves of an eclipsing binary is their segmented aspect. Only the skewness and kurtosis curves of the mean magnitudes did not present a segmented aspect. The segmentation can be understood if we consider that the eclipsing binary

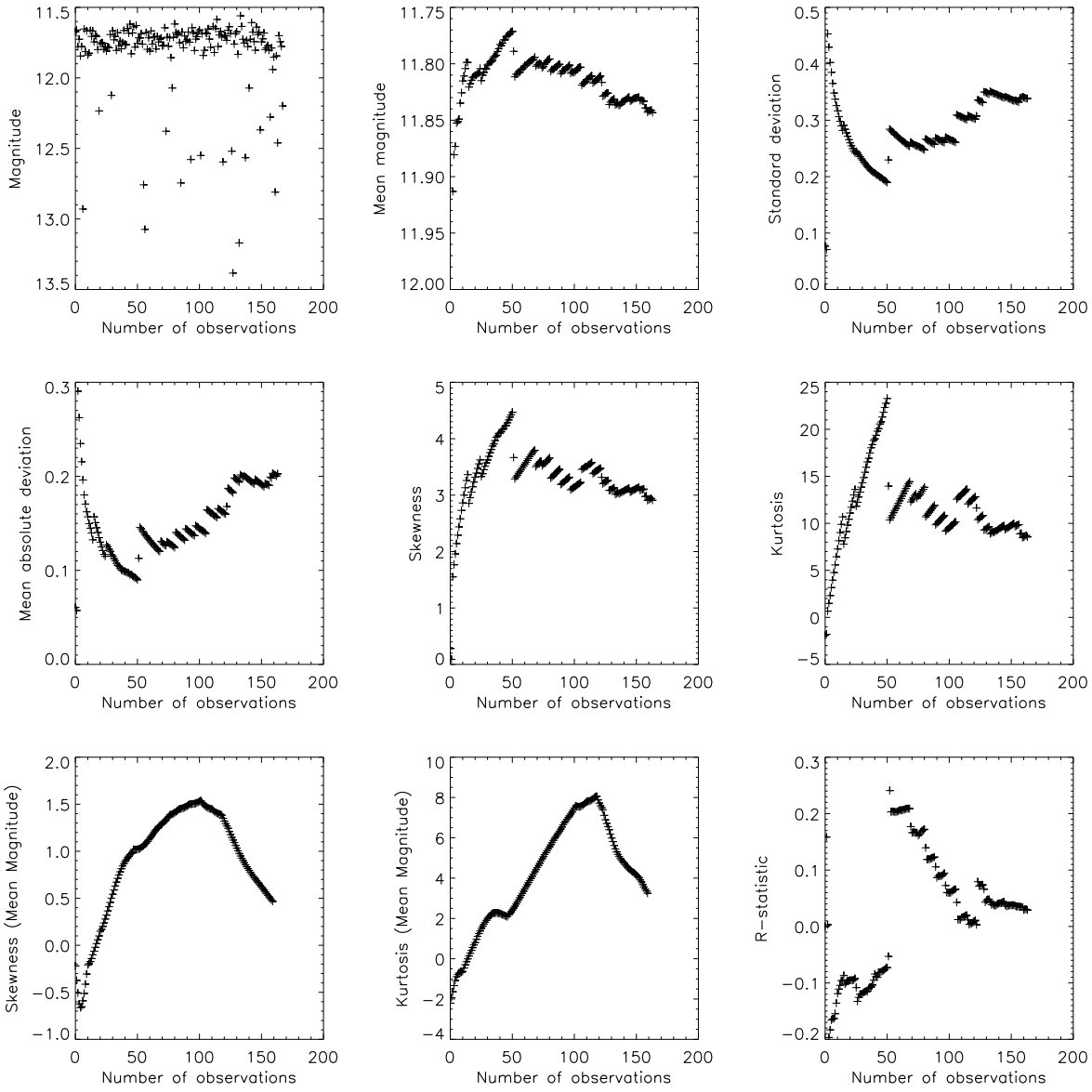

Figure 3.5: Statistical indices applied to an eclipsing binary as a function of time. The indices are the same as in Fig. (3.2).

has a constant magnitude except during the eclipses. Because we do not observe the eclipse continuously, we have sudden variations of brightness, as exemplified in the first panel of the first row in Figure 3.5, where we can see that most of the observations have a similar value except for those measured during the eclipses. These sudden brightness variations affect the statistical indices in a very peculiar way, that can be used to classify the eclipsing binaries in a large sample of light curves. All curves show a large variation around the observation number 50 and the most affected index is the R-statistics.

Figure (3.6) shows the statistical indices applied to the light curve of the first RR Lyrae star in Table (3.1). It is interesting to note that although the amplitude of the brightness variation is considerable (Δm=1.4) the mean magnitude oscillates with a small amplitude around a constant value from the middle to the end of the observations. The σ and σ_{abs} curves present small

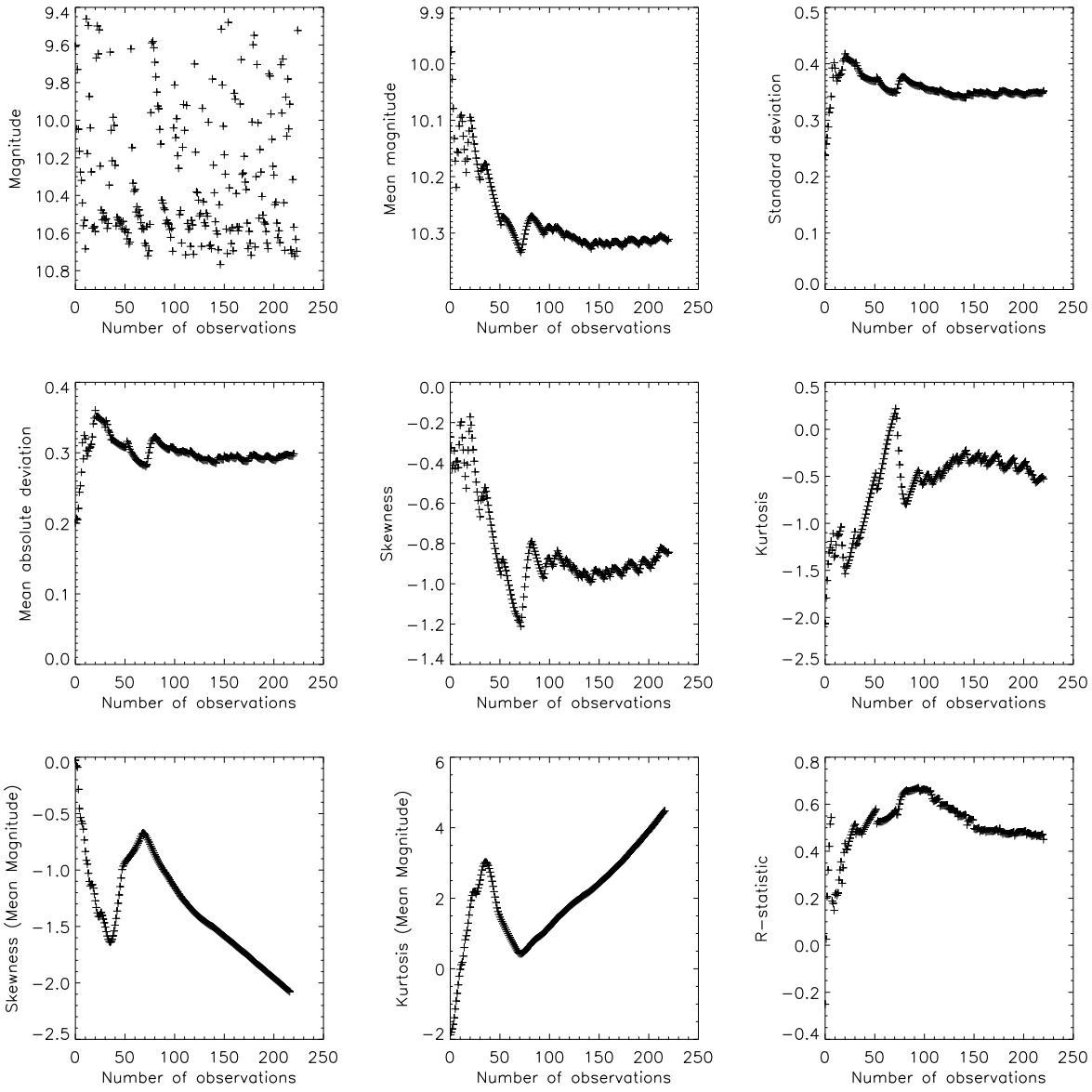

Figure 3.6: Statistical indices applied to an RR Lyrae type star as a function of time. The indices are the same as in Fig. (3.2).

variations, and like the mean magnitude, reach an almost constant value from the middle to the end of the observations. The skewness and kurtosis applied to the magnitudes present opposite behavior in the beginning but also reach almost constant values after 100 observations. The skewness and kurtosis applied to the mean magnitudes have opposite behavior.

Figure (3.7) presents the statistical indices for the first unknown type variable star in Table (3.1). We can see large scale variations in all index curves. The mean magnitude seems to reach an almost constant value from the middle to the end of the observations. The skewness and kurtosis applied to the mean magnitude show a large variation with opposite behavior but from the middle to the end of the observations they have the same behavior, a tendency to increase. The R-statistics curve reached an almost constant value, $\sim$0.8.

Cepheids, δ-Scuti and RR-Lyrae stars have a similar behavior for the skewness and kurtosis

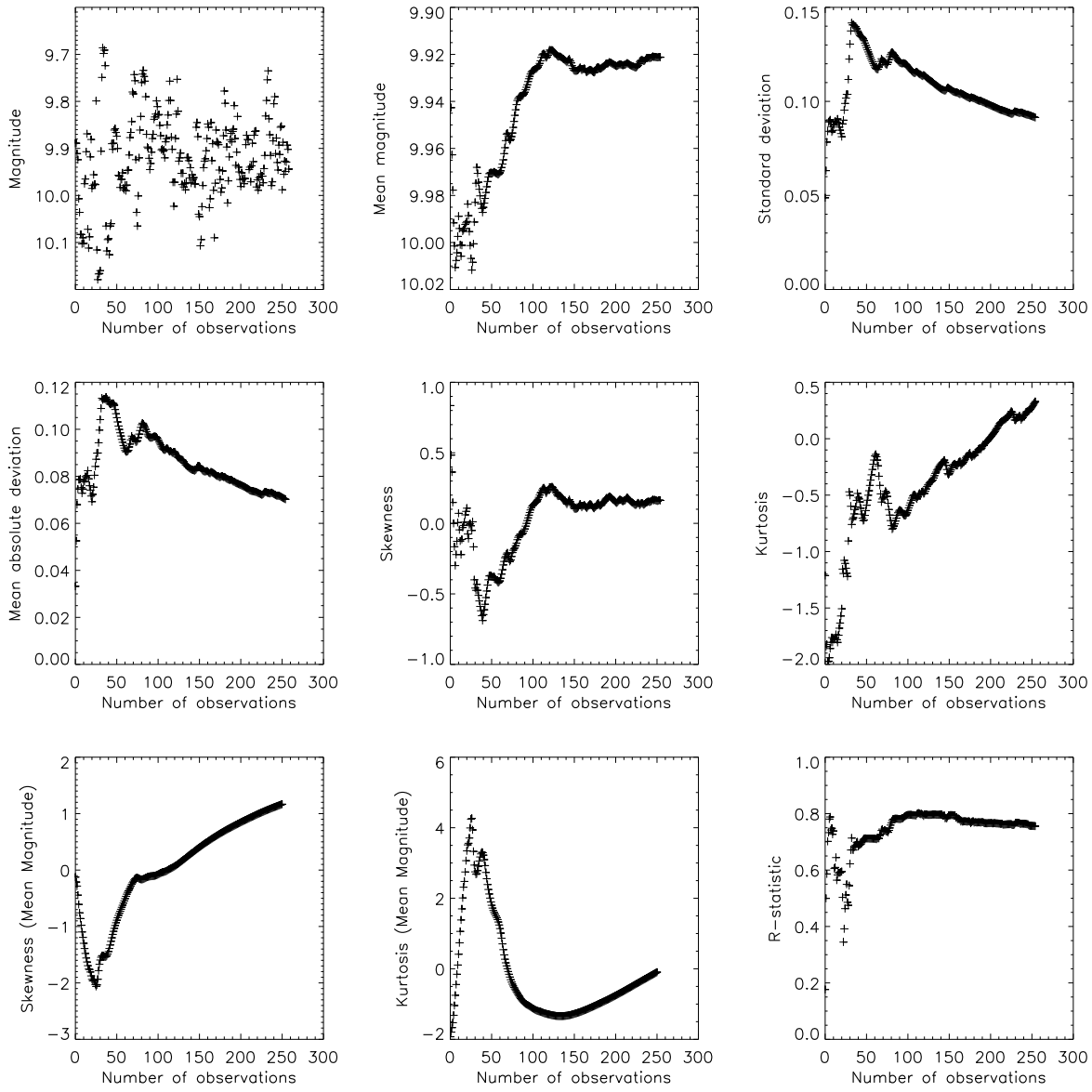

Figure 3.7: Statistical indices applied to the light curve of a star with unknown variability as a function of time. The indices are the same as in Fig. (3.2).

applied to the mean magnitude. The skewness, in these variables, tends to have negative values, meaning that the values with higher deviations are located in the left tail of the distribution. In other words, higher variations happen when the star becomes brighter. The kurtosis tends to have positive values, meaning that the distribution has a sharper peak around the mean than a normal distribution. This can also be seen in the σ and σ_{abs} curves, which reach constant values after some observations. These three are pulsating variables, hence, the opposite behavior of these two statistical indices can be used to separate them from the other variables.

The α^2-Canum Venaticorum variable star presents equal behavior for the skewness and kurtosis curves applied to the mean magnitude, both increase with time. An increase in skewness toward positive values implies that the deviations are higher when the star becomes fainter. This variable presents rotational variability.

The peculiar aspect of the statistical index curves for the eclipsing binary can be used to distinguish this class from the other variable stars in a large sample of light curves.

We still want to study in more detail the behavior presented by statistical indices of a continuously growing database. However, we will try to apply some of them to our variability surveys in order to test their reliability.

Chapter 4

The Orion Nebula Survey

4.1 Introduction

An overview of the Orion Nebula Cluster (ONC) was given in Chapter 2. We will discuss here the variable stars in this star forming region.

Since the beginning of the study of young stars by Joy (1945) and Herbig (1960, 1962), photometric variability served as one of the defining characteristics of pre-main sequence stars. Variability was first detected and studied in the optical bands but later it became clear that young stars are variable in all wavelengths. Rebull (2001) monitored $\sim$ 3600 young low mass stars in the outer regions of the ONC using optical (UVI_c) and near infrared filters (2MASS data) and determined periods for 281 low mass stars. Carpenter, Hillenbrand & Skrutskie (2001) used 2MASS data to study near infrared photometric variability in the Orion A Molecular Cloud. A large effort was done with the Chandra Orion Ultradeep Project (COUP) to understand the emission of X-rays by young stars in the ONC (Getman et al., 2005). Flaccomio et al. (2005) used the COUP data to study the modulation of X-ray emission in the ONC young stars and they were able to find stars where the X-ray modulation is correlated with the rotation period. Stassun et al. (2006) optically (BVRI) monitored the ONC while COUP was monitoring the same region in X-rays and they report time-correlated optical and X-ray variations.

Our group has participated of a similar survey, using photographic films (Kodak Tech-Pan 4415 emulsion, sensitive from approximately 630 nm and 690 nm, roughly the R band) and observations done at the ESO' Schmidt 100/152 cm telescope (La Silla, Chile), scanned by the SuperCOSMOS team[1]. The films covered a large area of 5° by 5° during a period of 2 years, and some preliminary results were published by Lima (2002).

Our purpose is to observe the ONC and its surroundings, in near infrared wavelengths (JHK), during a long time, in order to detect variable stars in timescales of a few days to a few months. One of the most important byproducts of such a survey is the detection of eclipsing binaries, whose stellar parameters are very important for putting constraints in the formation and evolutionary stellar models.

[1] http://www-wfau.roe.ac.uk/sss/

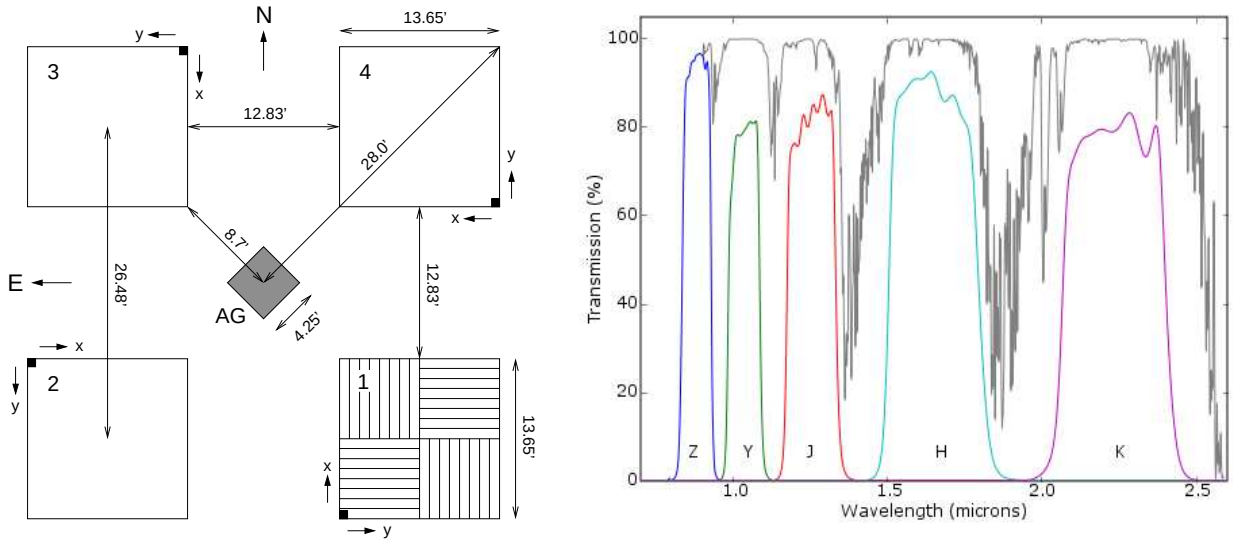

Figure 4.1: Left panel: Details of the WFCAM focal plane. The four detectors are shown in their respective position relative to each other. Detector 1 shows the channel layouts. Right panel: The broad band filters used in WFCAM. We used only the JHK filters in our survey.

We will try to attain our goals using observations made with the WFCAM, described in the next section. Unfortunately we will not be able to use the final pipeline released data because of problems detected in the subtraction of the sky background. We will instead use the summit pipeline data, which will give our results the status of preliminary results.

4.2 WFCAM Survey

WFCAM stands for Wide Field Camera, which is the most capable IR imaging survey instrument in the world, currently installed at the United Kingdom Infrared Telescope (UKIRT) at the summit of the Mauna Kea Observatory. It is composed of four Rockwell Hawaii-II 2048×2048, 18 micron pixel array detectors. The pixel scale is 0.4″ with a focal ratio of f/2.4. The detectors are spaced apart from each other in a way that four exposures are combined to cover 0.8 degrees[2]. The left panel in Fig. (4.1) shows the detectors' arrangement. Each detector is divided into quadrants and each quadrant is divided into eight channels of 128 × 1024 pixels, as exemplified in detector #1, in the left panel of Fig. (4.1).

WFCAM has eight filter housings, five are used for the broadband set ZYJHK, two are used for the narrow band H2 and Brγ and the last one is blanked for darks. In our survey we used the broadband filters JHK. An illustration of the filter passbands is shown in the right panel of Fig. (4.1).

4.2.1 Problems

There are many issues already known for the images acquired with the WFCAM. Some of these issues are corrected during the pipeline reduction. We describe some of the most important problems below. The description of these problems was taken from the instrument's webpage[2].

[2]http://casu.ast.cam.ac.uk/surveys-projects/wfcam

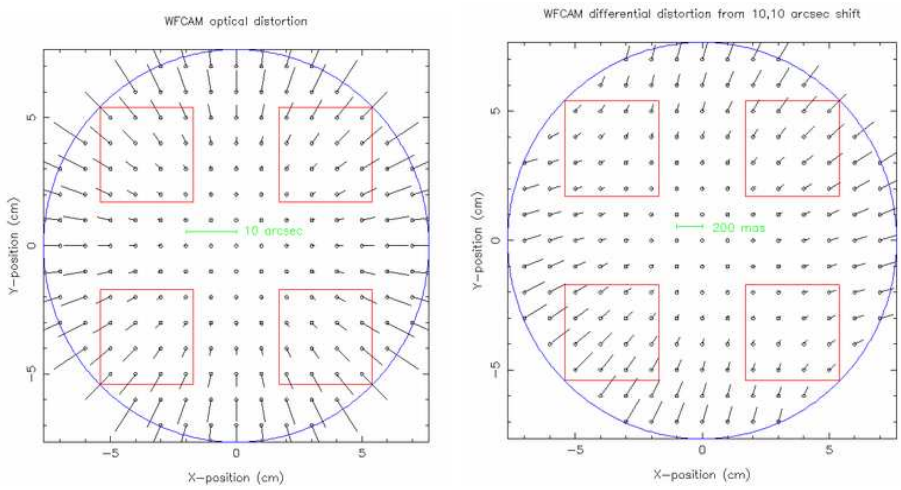

Figure 4.2: Left panel: Field distortion. Right panel: Differential non-linear distortion.

Field distortion can amount to 10″ from the center to the edge of the field. Most of the distortion can be accounted for by a cubic radial term, which is included in the WCS (World Coordinate System) solution. Differential non-linear distortion can also be present (∼1%). Both effects are presented in Figure (4.2).

Crosstalks are artificial structures created by saturated stars with either a doughnut appearance from heavily saturated regions or half-moon-like from only weakly saturated stars. They appear along the channels and have features at ∼1% of the differential flux of the source, dropping to ∼0.2% and ∼0.05% further out. Figure (4.3) illustrates, in the left panel, where crosstalk images are expected in the detector X-Y space relative to the position of saturated objects for each quadrant. The crosstalk pattern rotates from quadrant to quadrant because the readout amplifier for each quadrant is on a different edge of the detector (denoted by the red lines). The right panel in Fig. (4.3) shows an example of crosstalk detected in our images.

Dark current and reset anomaly are 2D additive features that affect WFCAM. All IR detectors suffer from reset anomaly to some degree and its main component is a large intensity ramp at one edge of each quadrant (where the readout amplifier is located), reaching about 50 ADUs.

It has been shown that the reset anomaly ramp is stable throughout a night and even between nights for a given set of exposure parameters. The ramp is remarkably similar for a wide range of exposure times. This implies that master darks can be used to do the reset anomaly correction. However, care must be taken to reject any dark frames that are exposed right after a filter change to avoid any persistence effects.

Darks are routinely computed from daily observations, by combining as many darks taken with the same readout parameters as the object frames of interest (that is exposure time, readout mode and number of coadds). By combining many dark frames, artifacts such as cosmic rays can be eliminated from the resulting master dark.

The average dark current is generally negligible and the dark frames are dominated by reset anomaly variations, as shown in Figure (4.4).

Decurtaining is a pseudo-periodic ripple at the ±5 ADU level and can be seen at low level in the darks. It is best illustrated by the difference between two dark frames of the same type,

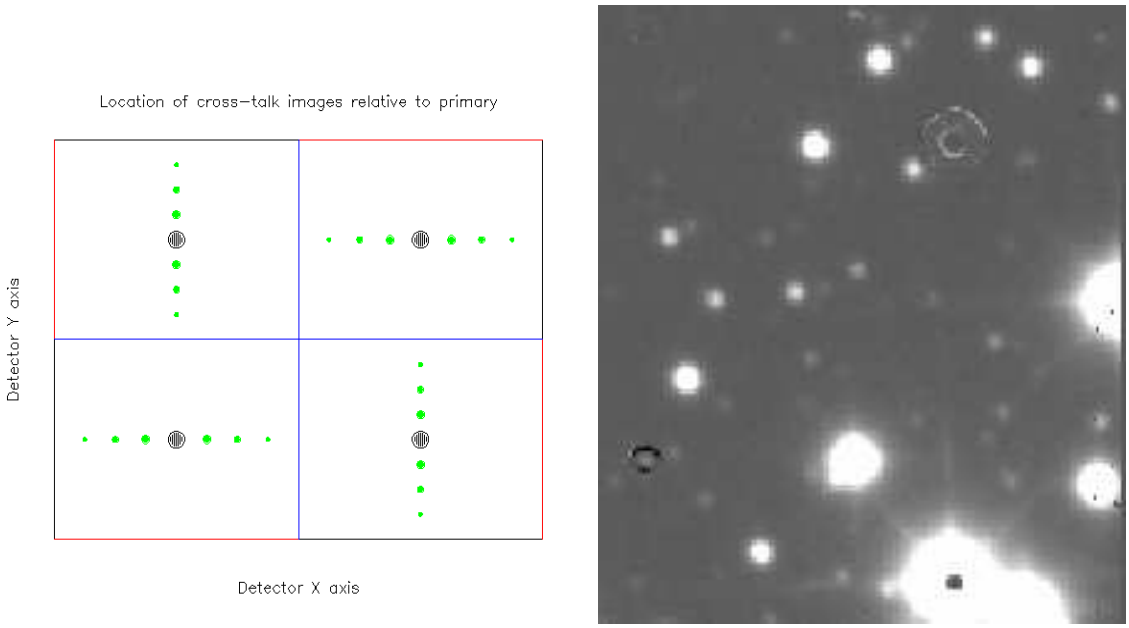

Figure 4.3: Left panel: Diagram showing how the crosstalks appear in different quadrants. The crosstalk pattern rotates because the readout amplifier for each quadrant is located on a different edge of the detector, as shown by the red lines. Right panel: An example of crosstalk detected in one of our images. Whenever there is a saturated star, a crosstalk pattern will be present.

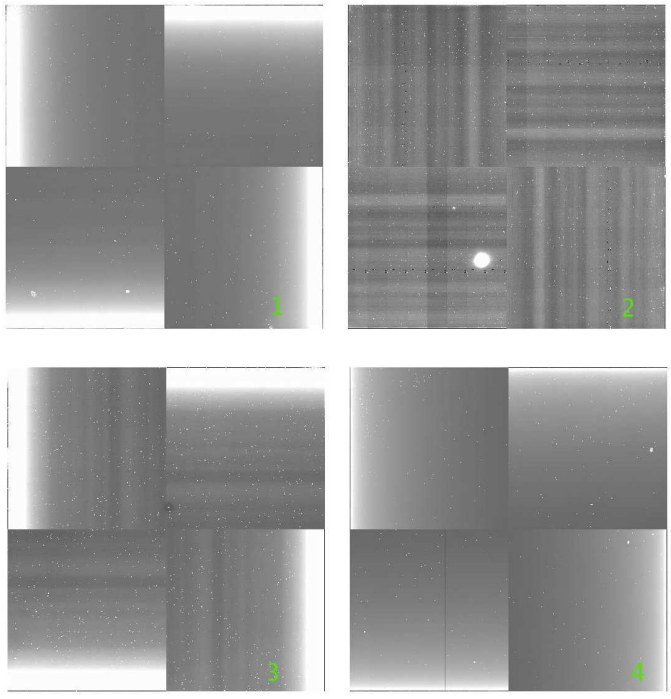

Figure 4.4: This figure shows how the dark frames, for all detectors, are dominated by the reset anomaly.

as shown in Figure (4.5).

An algorithm is used to correct this problem and the results can be seen in the right panel of Figure (4.5).

Persistence happens when a saturated image in a previous exposure leaves a persistent image in following exposures. It has been observed in WFCAM data and is typical of infrared

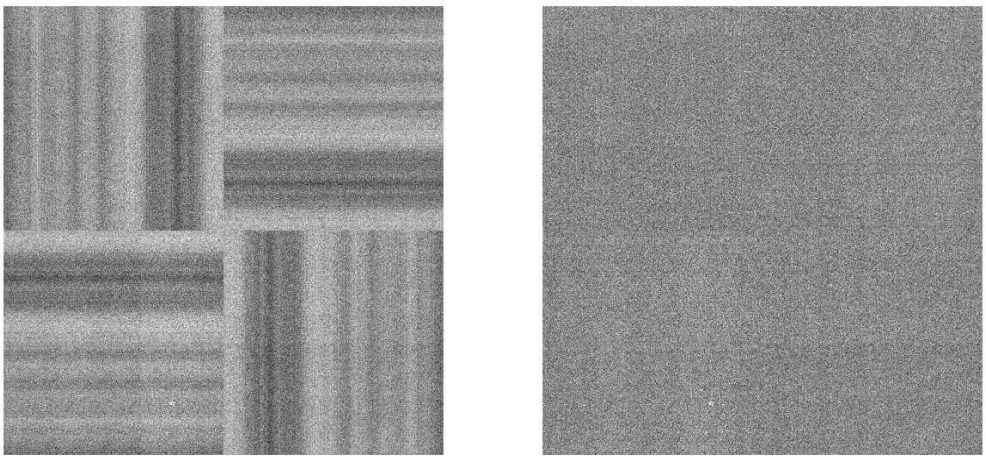

Figure 4.5: Left panel: Difference between two dark frames taken in order to show the decurtaining effect. Right panel: Dark frames with decurtaining solved.

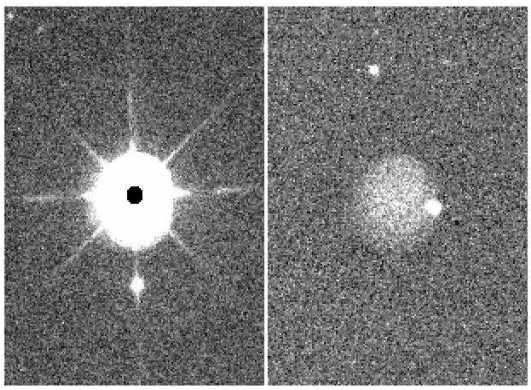

Figure 4.6: This figure shows an example of persistent images in the WFCAM.

detectors. This phenomenon is not clearly understood and varies considerably between detectors. Persistent images are very approximately top-hat shaped and cover the area that was saturated in the contaminating frame. Persistence is not corrected by the pipeline reduction and an example is shown in Figure (4.6).

4.2.2 Reduction

By the time we started the analysis of the M42 data we did not have the final reduction data. We used the summit pipeline data, which was done using routines similar to the ones used in the final pipeline. However, some of the problems described in the previous section were not corrected during the summit reduction. We deal with them using our own routines in IDL.

The basic steps for the normal astronomical reduction were taken during the summit reduction and we describe them below.

Dithering is the procedure of splitting a long NIR exposure into several short exposures at slightly different positions in order to minimize the contribution from bad pixels and cosmic rays, and to avoid background saturation. Dithering shifts and combines these input frames into a single output using the appropriate dither offsets, which are initially calculated from the WCS

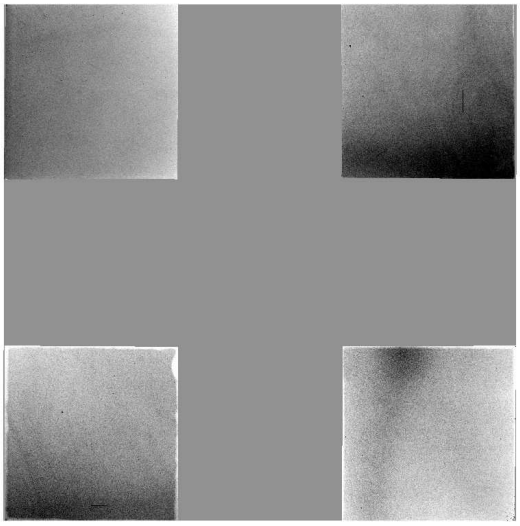

Figure 4.7: This figure shows an example of the flatfield correction.

parameters in the FITS headers that have been generated from the astrometric calibration. The offsets are then further refined by object position cross-correlation.

Flatfield in the WFCAM departs somewhat from the usual NIR processing strategies by making extensive use of twilight flats, rather than dark-sky flats, which potentially can be corrupted by thermal glow, fringing, large objects etc. The principle adopted is to attempt to decouple sky estimation/correction from the science images. An example is shown in Figure (4.7).

Ideally, sufficient (dawn) twilight flatfield frames to form master flats are taken once a week using a series of 9-point jitter sequence observations in Z,J,K one night and Y,H the next. Note that it is impossible to get good flats in all broadband filters in any one night. The suitable individual 9-point jitter sequences ($\sim$5000-20000 counts/pixel ie. $\sim$25000-100000 e^-/pixel) are dark-corrected and then scaled and robustly combined to form new master flats. If enough are available, these may be further combined to reduce the random photon error in the master flats even further. If available a pair of these flats at different count levels ($\sim$factor 2) is then used to automatically locate the bad pixels and create the generic confidence map, one for each filter. Bad pixels are defined as those having properties significantly different from their local neighborhood "average" in the individual master flats or in their ratio.

These flats give good dark sky correction (i.e. gradients are at the $\sim$1% level at most), and show no fringing nor measurable thermal emission. The overall QE is good but the flats show large spatial gradients across the detectors indicative of up to a factor of 2 sensitivity variation. Since the general characteristics of these variations can be seen across all filters, the simplest interpretation is that these variations in level reflect genuine sensitivity variations across the detectors. This has been subsequently confirmed by examining the χ^2 values of the residuals from PSF-fitting. These sensitivity variations also cause problems for the generation of the confidence maps, uniformity of surveys, and possibly also impacts on the calibration error budget.

Photometric calibration is currently based on 2MASS, via color equations to convert to the WFCAM instrumental system. 2MASS solutions for every catalogued frame are generated and allow monitoring of effective ZPs (Zero Points) at the $\sim$few % level.

4.3 Observations

The observations began in October 2006 and ended in April 2007, giving us a total of 101 nights. This is a short program that only uses some minutes per night, with 2 seconds per exposure. Table (4.3) shows the observation dates for the ONC.

Table 4.1: Observation log for the Orion Nebula.

October - 2007	26	27	28	30	31						
November - 2007	01	09	11	12	13	14	15	16	17	19	20
	21	22	23	26	27	29	30				
December - 2007	05	06	08	09	10	12	14	15	16	17	19
	20	21	23	24	27	28	29	30	31		
January - 2008	01	02	03	06	14	15	16	17	18	19	20
	22	24	25	26	27	28	30				
February - 2008	05	06	07	12	13	14	15	16	19	20	21
	22	23	24	25							
March - 2008	02	03	04	05	08	09	10	16	17	18	19
	20	21	22	23	24	25	26	27	28	29	
April - 2008	04	19	20	21							

The observation method used by the WFCAM consists of performing four exposures with a coordinate shift between each exposure, in a way that a mosaic is obtained in the end of the process. We designate each area to be exposed as a letter: a, b, c, d. Each CCD in the camera is also designated as a letter: w, x, y, z. Figure (4.8) shows the layout used to observe the ONC. Each exposure took two seconds.

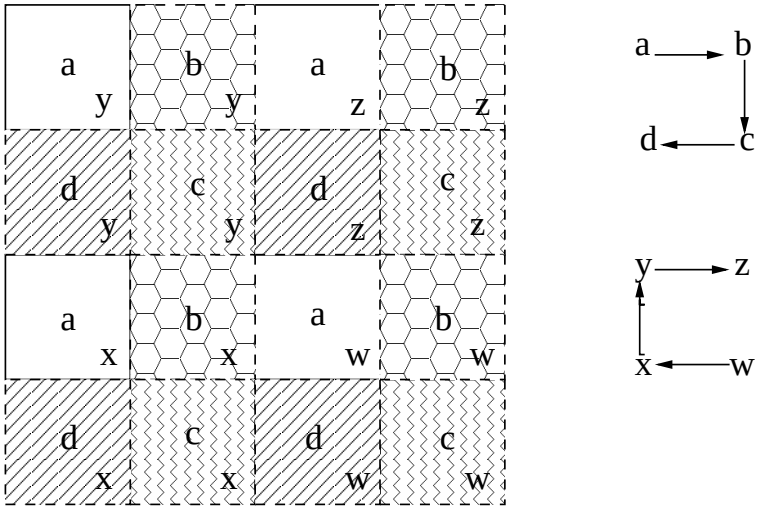

Figure 4.8: WFCAM layout and reading scheme used to observe the ONC.

We had access to the summit pipeline reduced data during the observation period. The data was kindly reduced by Dr. Andy Adamson after each night of observation. The summit pipeline,

however, does not have all the tools necessary to deal with deformations and field distortions.

We started working on the data at the end of 2006, while part of the observations was still in progress. The catalogs have a simple structure in ASCII format, easy to be read by IDL routines. Each CCD for each area has a separate catalog. An example of a catalog is given below.

```
1 colours were created
K
Origin: IO::SExtractor
0 09  05 35 20.97  -05 31 21.69  1991.484 71.761 -14.8113  0.0010  0
0 10  05 35 21.03  -05 28 09.25  2949.217 69.721 -14.3697  0.0014  0
0 11  05 35 21.16  -05 25 56.98  3607.804 60.891 -14.8718  0.0009  0
0 13  05 35 21.30  -05 24 57.29  3905.070 51.429 -15.1335  0.0007  0
0 17  05 35 21.63  -05 26 57.76  3305.145 25.587 -13.0385  0.0049  0
0 19  05 35 21.56  -05 32 46.01  1572.265 27.137 -11.2798  0.0248  0
```

The first line indicates that there is only one color in the catalog, which is shown in the second line. The third line indicates that the catalog was generated by the summit pipeline. The parameters for each star start in the fourth line of the catalogs. The first column is an empty flag and the second column gives an ID for each detection. The third, fourth and fifth columns contain the right ascension (H:M:S.S), the sixth, seventh and eighth columns contain the declination (D:M:S.S). The ninth column presents the number of counts and the tenth column has the count error. The instrumental magnitude is presented in the eleventh column, with the associated error in the twelfth column. The last column shows a flag that indicates if the measurement is good (0) or bad (99).

An IDL routine was written to read the catalogs. We can see in the second column that the running ID isn't linear and in fact is not fixed for each star. It only denotes the order of the detections. The same star has different IDs for different filters (JHK) and different nights, meaning that we have to read each catalog and store the information about each star in a new table.

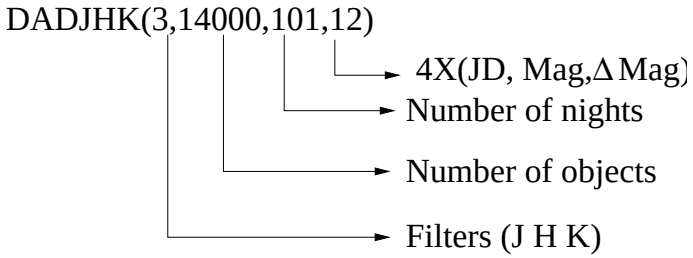

Figure 4.9: DADJHK - layout of the table containing all the photometric information.

Figure (4.9) presents the layout of the structure used in the new table that contains all the photometric information, for each star. We created a matrix with dimensions shown in Fig. (4.9), where the last dimension has twelve positions. We repeated the parameters; Julian data (JD), magnitude (Mag) and error in the magnitude (ΔMag), four times because stars on the borders of the CCDs can be detected more than once, since the CCDs overlap each other. Thus, one star can be stored in different catalogs for the same night in the same filter.

The observations were performed using the filters in the KHJ order. We analyzed each object

individually in the first night because we wanted to be sure that only objects with stellar profiles were being catalogued. Crosstalk, cosmic rays and persistence defects were rejected during this procedure. We began facing problems when we started analyzing the second night. Due to the fact that the field and differential distortions were not corrected by the pipeline, the same stars had very different coordinates from one night to the other. It was necessary to create some sort of correction for the coordinates.

4.3.1 Workarounds

In order to find the correct coordinates for stars in different nights, we wrote an IDL routine that shifts the coordinates until the correct match (inside a given error limit) is achieved. We searched inside an area of $0\farcs6$ radius trying to find matching objects. The separation from the object being analyzed to the catalogued one is stored in a different matrix. All objects are searched and the separations are stored. In a second step we perform a shift in the coordinates using the values stored. The necessary shift is calculated using weights. We give more weight to the objects with smaller separations, assuming that large separations are produced by defects or previously undetected objects.

We realized that one shift was not enough to produce the desired effect and hence we started to perform subsequent shifts. We were surprised to see that some nights required large shifts, sometimes requiring initial shifts of $7''$. We ended up with a routine that uses six shifts, beginning with large values ($20''$) and performing the two last shifts with a search radius of $0\farcs6$. This procedure corrected the field and differential distortions.

We were lucky to have few stars per CCD because a considerable computational time is required to perform each shift. It took us approximately five months to have a preliminary database with all the observed nights. Although the number of nights is 101, our database has only 98 nights because 3 nights were not reduced by the summit pipeline.

4.3.2 Superposition problems and calibration solutions

When we began analyzing the stored data we faced a problem that we did not expect. Each CCD has a different detection level for each area, and also for different nights. This means, for example, that the CCD 'w' has a different detection level when used in area 'a' and area 'b'. Also the same CCD, 'w' for example, showed different detection levels in different nights even when used in the same area. This problem would make the construction of the final database much harder than we thought because stars located in the superposition areas had four different magnitudes in the same night. We are not certain about the causes of these level variations.

Figure (4.10) shows plots of (Mean Magnitude - Magnitude) versus Magnitude, for all the 16 fields in the J band, that when put together comprehend the full mosaic of the fourteenth night. We are using the instrumental magnitude and it is possible to see that the measurements behave in the same manner. All the CCDs have the same level in all areas. We expect that, in this kind of plot, most of the data points are situated about the zero value.

Figure (4.11) shows the same kind of plots but for the eighteenth night, where we can see clearly that the CCDs present different levels for different areas. There is no measurement for the CCD y in area d (first column, second row). We can see in the panels of Fig. (4.11) that the data points have the behavior we expect, except that they are not situated about the zero

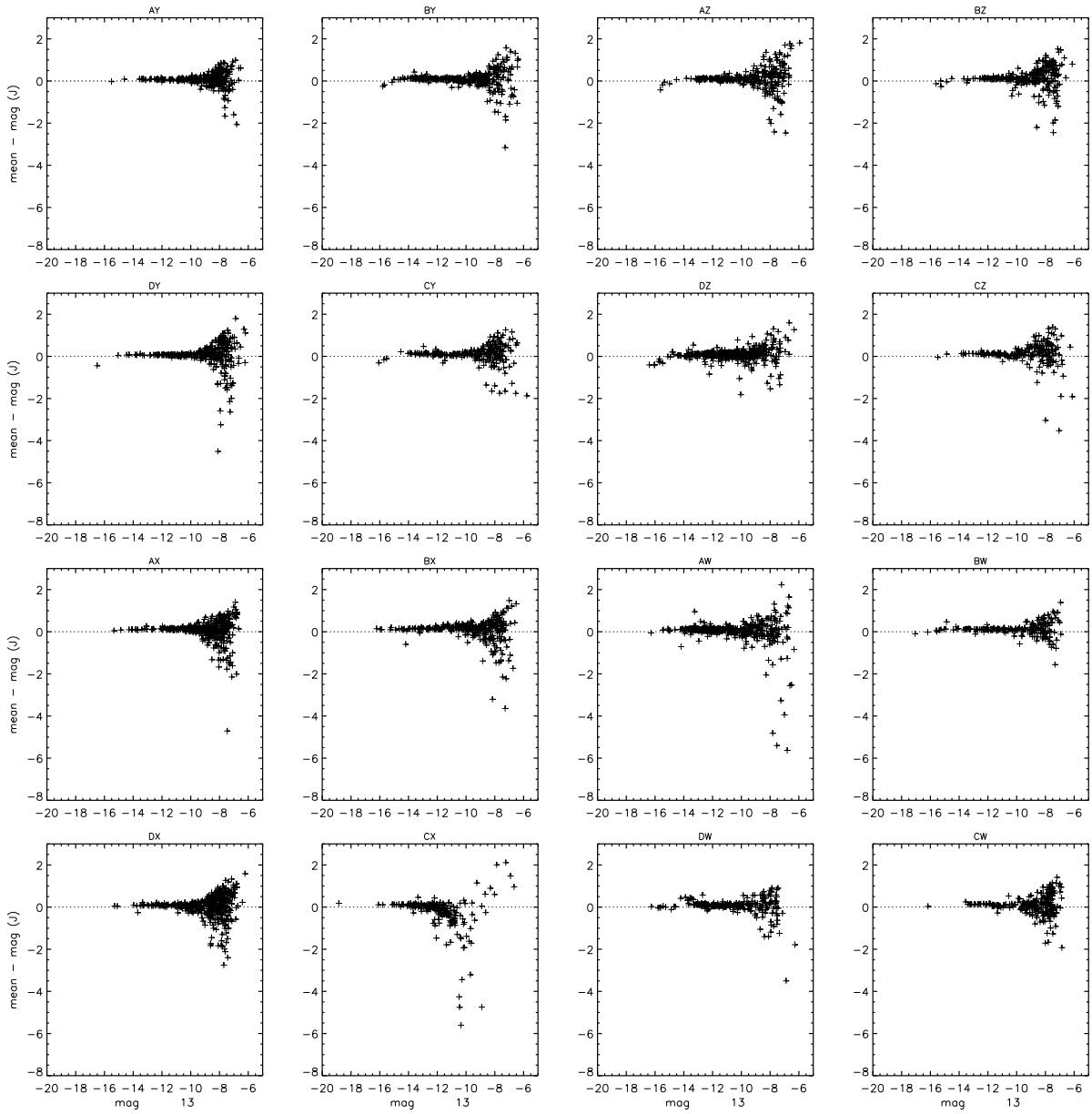

Figure 4.10: (Mean Magnitude - Magnitude) versus Magnitude for the filter J, fourteenth night, for all the CCDs and areas. The panels are distributed in the same layout shown in Fig. (4.8).

value, but shifted by 2 and even 4 magnitudes.

Because we were dealing with data from the summit pipeline, we decided to analyze stars located outside the superposition areas. In other words, we will only analyze stars that have been detected once each night. This way we can perform the necessary level corrections for each CCD individually.

The level correction for each CCD was done using constant shifts in the objects' magnitude. To obtain the shift values we first calculated the geometric deviation for each CCD, in each area, for each filter, for each night. As explained in Chapter 3, the geometric deviation will help us identify the most constant stars. We will use these stars to calculate the mean magnitude that will be used to shift the data points toward the zero value.

After this step was taken one last procedure is necessary. Because we are dealing with data

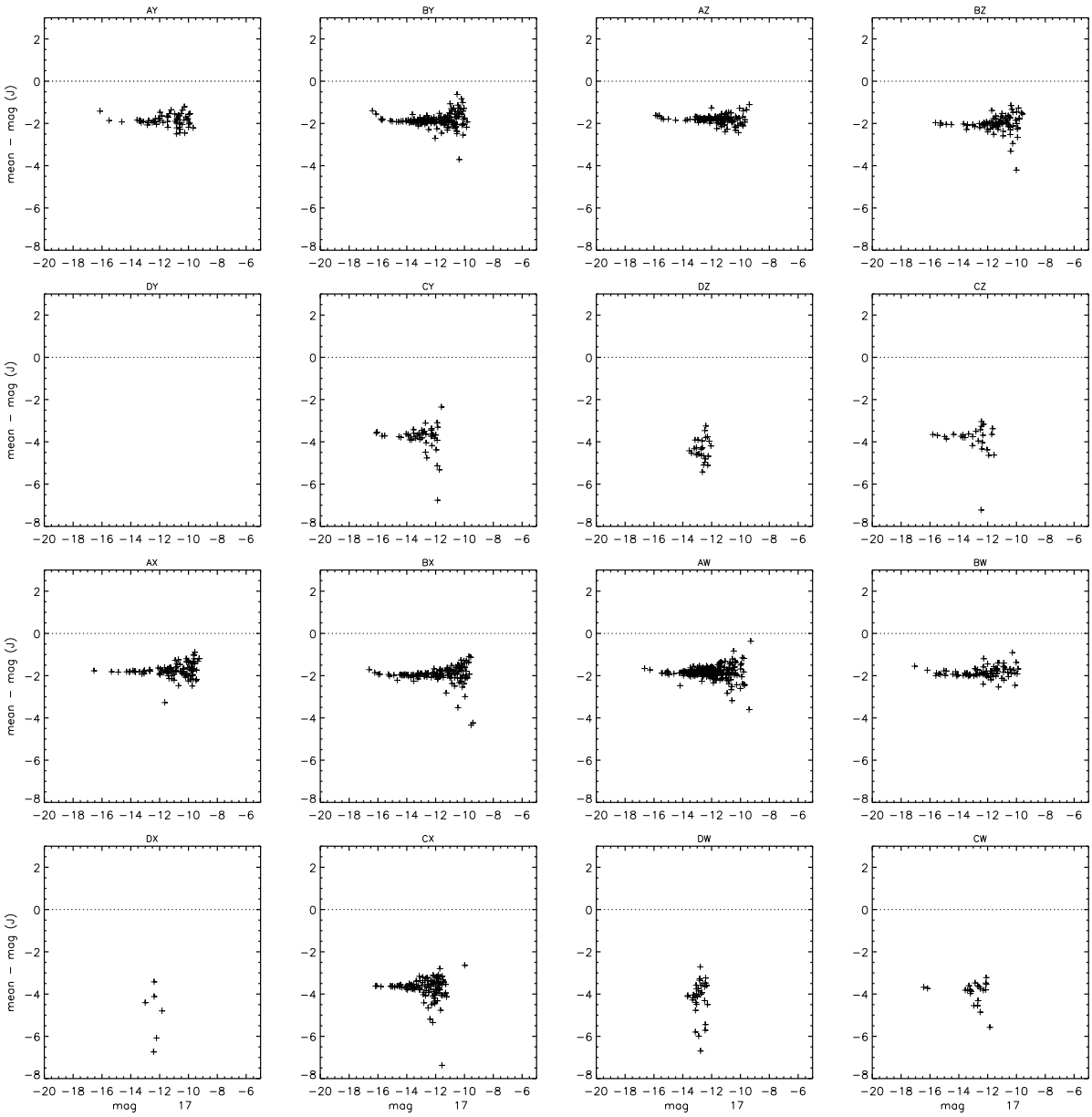

Figure 4.11: Same as Fig. (4.10) but for the eighteenth night.

coming from the summit pipeline, and also due to the fact that Orion is a region with strong background variation, we decided to do differential photometry for all the stars in the field. Such procedure requires constant stars along the observations to be used as comparison stars. We need a set of constant stars for each CCD in each area.

Using the geometric deviation, the absolute value of the maximum amplitude variation (AMV) and the maximum deviation from the mean magnitude (MDM), we selected the six most constant stars present in each CCD for each area. We considered geometric deviations values lower than 0.01, AMV values lower than 0.30 magnitudes and MDM lower than 0.15 magnitudes. The limit value of the last two parameters changed for different CCDs in different areas. The best values were achieved for the CCD w in area a, with maximum values for AMV and MDM respectively 0.06 and 0.03 magnitudes. The worst values were found for the CCD y in area d (0.30 and 0.15 magnitudes for AMV and MDM).

Once the constant stars were chosen the differential photometry could be obtained comparing the magnitude of the star being analysed with the constant stars, as shown below.

$$\begin{aligned} \Delta M_1 &= M - C_1 \\ \Delta M_2 &= M - C_2 \\ \Delta M_3 &= M - C_3 \\ &\vdots \end{aligned}$$

where ΔM_n is the differential magnitude relative to the n^{th} comparison star. However, we can define the best comparison star, for each CCD in each area, as the *primary* comparison and transform the other comparison stars to the *primary*.

$$\begin{aligned} \Delta C_2 &= \overline{C_1} - \overline{C_2} \\ \Delta C_3 &= \overline{C_1} - \overline{C_3} \\ &\vdots \end{aligned}$$

where ΔC_n is the difference between the n^{th} comparison star and the *primary*, obtained using the mean magnitudes ($\overline{C_n}$). We use mean magnitudes because the comparison stars were considered to be constant stars.

We can then transform the comparison stars into the *primary* using the following equations.

$$\begin{aligned} C_{P2} &= C_2 + \Delta C_2 \\ C_{P3} &= C_3 + \Delta C_3 \\ &\vdots \end{aligned}$$

This procedure allows us to do n comparisons between the star in study and the *primary*.

$$\begin{aligned} \Delta M_1 &= M - C_1 \\ \Delta M_2 &= M - C_{P2} = M - C_2 - \Delta C_2 \\ \Delta M_3 &= M - C_{P3} = M - C_3 - \Delta C_3 \\ &\vdots \end{aligned}$$

The mean value of the M_n differential magnitudes will be our differential magnitude. The final equation to be applied to the data is:

$$\langle \Delta M \rangle = M - \overline{C_1} + \frac{1}{n} \sum_{i=2,N} (\overline{C_i} - C_i) \tag{4.1}$$

where M is the instrumental magnitude of the star, C_1 is the *primary* comparison in that CCD in that area, n is the total number of comparison stars (six in our case) and C_i is the i^{th} comparison star. This equation must be applied for each night of observation. M and C_i are the magnitudes for the night being corrected.

After the level correction for each CCD and the procedure to obtain the differential photometry, we began to reorganize the photometric and astrometric data. We need to know the position of a specific star inside the data matrix in order to retrieve the magnitudes for each

filter and each night. An IDL routine was written to reorganize the data and this step was easily done.

With the data reorganized we were able to plot the light curves for all the stars, and also to apply the statistical indices to the light curves.

4.4 Variable Candidates

We will show in this section some of the results achieved with the preliminary data for the Orion Nebula. Although the results have a preliminary status, we want to emphasize that the kind of variability shown here is real and in some cases corroborated by works of other authors.

We wrote IDL routines to calculate the statistical indices for the whole sample and after that we analysed the results individually.

4.4.1 Eclipsing binary candidates

We will first present six eclipsing binary candidates. Table (4.2) presents the identification of the candidates, their coordinates, trial periods and period errors. Due to the fact that we have few points to define the minima of the light curves, we are not able to obtain precise periods. An observational campaign is necessary in order to better constrain the period and also to obtain the orbital solution for these binaries.

Table 4.2: Six candidates to be eclipsing binaries in M42

ID	RA(J2000)	DEC(J2000)	Per(d)	err(d)
JW 102	05:34:48.957	-05:28:16.70	10.6	0.1
V387 Ori	05:35:05.312	-05:34:28.43	8.59	0.01
JW323	05:35:08.531	-05:25:18.01	31	1
JW 363	05:35:11.080	-05:36:50.51	7.02	0.01
COUP 462	05:35:12.043	-05:28:08.32	7.28	0.01
OX Ori	05:35:54.622	-05:27:07.77	17.31	0.01

As described in Chapter 3, the Mean Magnitude curve of an eclipsing binary is very peculiar, with descontinuities caused by sudden changes in brightness. We used these Mean Magnitude curves to help us in the task of finding eclipsing binaries. There is, however, another kind of variable star that also presents discontinuities in the Mean Magnitude curve, the flare stars. This kind of variable presents sudden increases of brightness, which cause the same kind of peculiarity in the curves we want to use. To help us distinguish between flare stars and eclipsing binaries we used the maximum deviation from the mean, which is positive for flare stars and negative for eclipsing binaries. We also used the continuous light curve as a visual guide when analyzing individually the stars, since the light curve of these variables has an opposite behavior.

Figures (4.12) and (4.13) present the continuous light curve, the Mean Magnitude curve and the phased light curve of the eclipsing binary candidates. Each plot presents the name of the respective star. The phase is obtained using the following equation:

$$\Phi = \mathrm{frac}\left(\frac{\tau - \mathrm{E}_0}{\mathrm{P}}\right), \qquad \tau = \mathrm{t} + \delta\mathrm{t} \tag{4.2}$$

where τ is the time of mid-observation with heliocentric correction, P is the period, E_0 is the epoch or instant of an adopted minimum and *frac* denotes the decimal part of that ratio.

The period of each star was obtained through the use of the phase dispersion method by Lafler & Kinman (1965), which searchs for periodic signals. The test requires that the sum of the squares of the magnitudes differences between observations of adjacent phase to be a minimum. It uses the following equation:

$$\theta = \frac{\Sigma_i (m_i - m_{i+1})^2}{\Sigma_i (m_i - \overline{M})^2} \tag{4.3}$$

where $\overline{M}$ is the mean magnitude and N is the number of observations. The denominator is independet of the phase and thus only the numerator needs to be calculated for each trial period. Hence, in principle, the period with the minimum value of θ is the nearest to the correct one.

4.4.2 Periodic variables

We used the skewness and kurtosis of the mean magnitudes to construct skewness curves and kurtosis curves, which were then used to identify stars that present pulsational or rotational modulation. During the individual analysis of each star, we selected 23 stars that present clear evidence of periodic modulation.

Table (4.3) presents the stars identified through this technique. The first column shows the name of the stars, followed by their coordinates in the second and third columns. The period determined in this work is presented in the fourth column, with the respective error in the fifth column. Columns 6, 7 and 8 present the identification, period and error when a star is present in the catalogue published by Stassun et al. (1999). Columns 9, 10 and 11 present the identification, period and error listed in the catalogue published by Rebull (2001). We obtained the periods of the stars using the same technique applied to the eclipsing binaries. The values listed in Table (4.3) are mean values obtained using the periods for all filters (some stars do not have JHK light curves, in such cases we used the filters available).

Except for V1289 Ori, V482 Ori and V1277 Ori, the periods obtained in our work and the periods obtained by Stassun et al. (1999) and Rebull (2001) agree within the errors.

Figures (4.14) to (4.21) present the continuous light curve, the phased light curve, the skewness curve and the kurtosis curve of the stars listed in Table (4.3) Each panel is identified by the name of the star.

4.4.3 Interesting light curves

The catalogue is composed of approximatelly eight thousand stars and it is beyond the scope of this work to present all the light curves. We present here examples of interesting light curves found within our sample. A survey covering a large area of an important star forming region like the Orion Nebula, with such a long timeline base, will certainly change our view about the variability status of young stars.

Table (4.4) presents the names and coordinates of these interesting stars while Figure (4.22) presents their light curves.

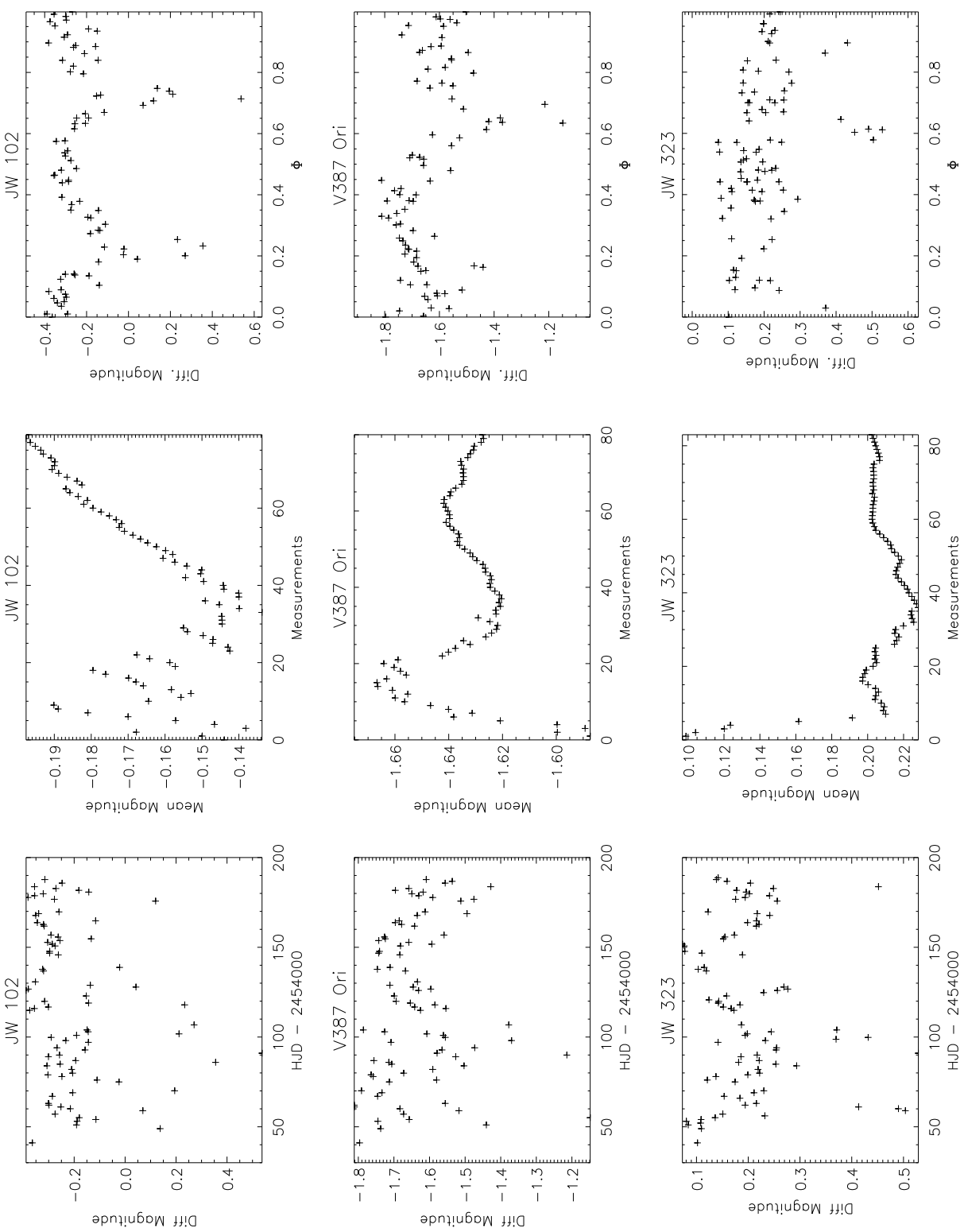

Figure 4.12: Light curves, Mean magnitude curves and phased light curves for three eclipsing binary candidates.

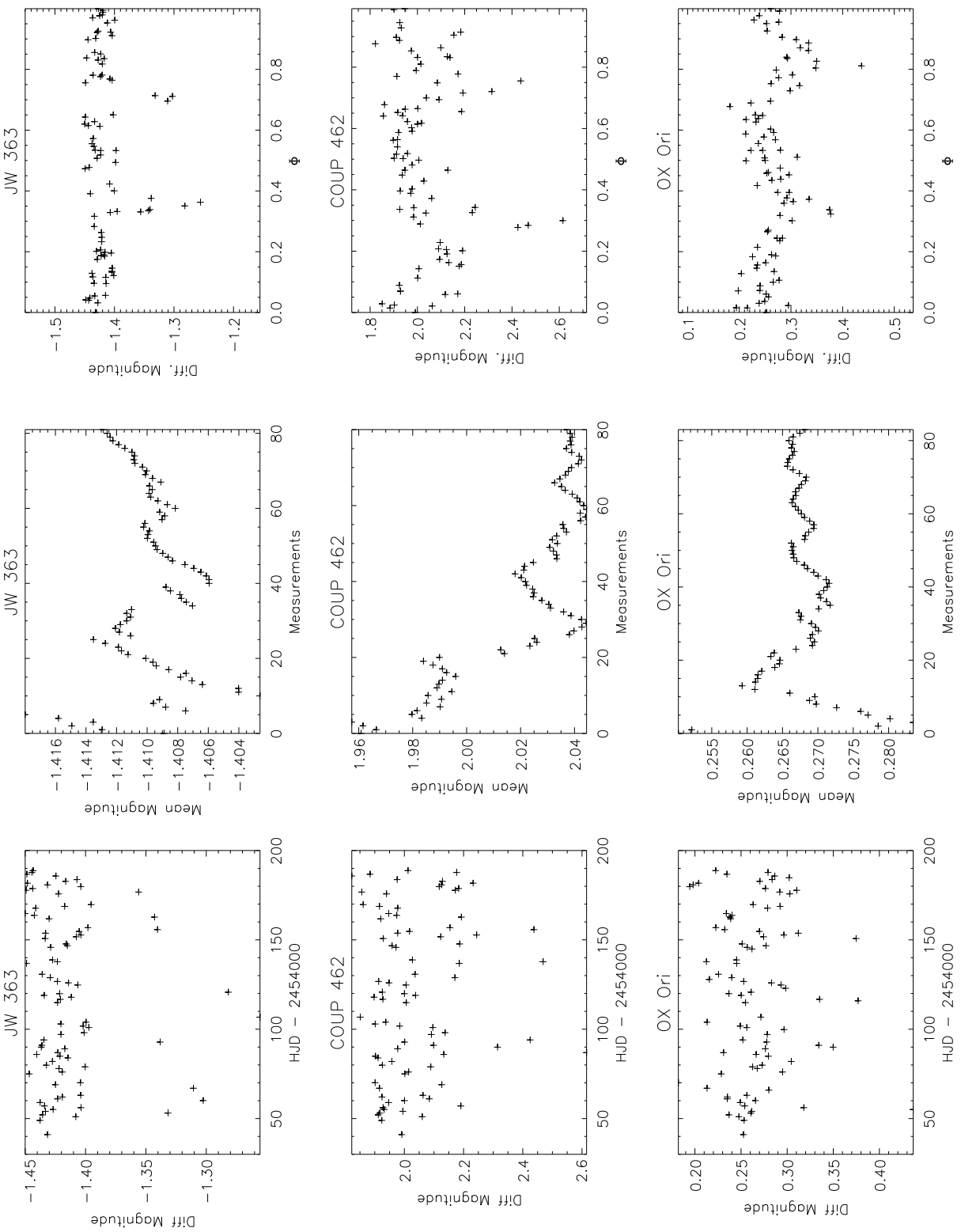

Figure 4.13: Light curves, Mean magnitude curves and phased light curves for three eclipsing binary candidates.

Table 4.3: Objects candidate to be variable, selected through the study of statistical indices

ID	RA(J2000)	DEC(J2000)	Per	err	SMMV	Per	err	R2001	Per	err
MN Ori	05:35:15.774	-05:33:12.17	9.570	0.004						
V1479 Ori	05:35:01.475	-05:28:20.45	5.467	0.004	1545	5.32	0.23			
KO Ori	05:34:56.463	-05:31:35.81	5.740	0.003						
JW 156	05:34:55.526	-05:36:05.82	7.87	0.01						
V1313 Ori	05:34:43.394	-05:30:06.52	7.381	0.003	1099	7.04	0.40			
Parenago 1327	05:34:00.308	-05:35:42.60	18.5	0.2						
V385 Ori	05:33:33.865	-05:33:25.39	7.073	0.003						
V386 Ori	05:33:44.904	-05:31:07.55	2.6276	0.0006						
V1293 Ori	05:35:30.657	-05:27:16.75	6.336	0.004	3197	6.30	0.32			
V1561 Ori	05:35:31.669	-05:30:04.10	5.549	0.006	3240	5.51	0.24			
V1539 Ori	05:35:27.479	-05:35:19.41	4.688	0.008	3088	4.62	0.17			
V947 Ori	05:35:49.466	-05:35:26.47	8.61	0.01	3710	9.27	0.69	2329	8.63	0.022
V1123 Ori	05:35:23.467	-05:10:51.78	7.64	0.01	2919	7.70	0.47	1989	7.64	0.009
TKK 891	05:35:29.062	-05:06:04.10	3.305	0.004						
V1585 Ori	05:35:52.171	-05:39:24.89	6.226	0.005	3758	6.27	0.31	2356	6.24	0.012
V1558 Ori	05:35:31.232	-05:40:10.81	6.17	0.01	3220	6.15	0.30	2089	6.09	0.011
CHS2001 10147	05:35:26.118	-05:45:08.46	5.828	0.004						
V1289 Ori	05:35:29.469	-05:16:33.40	10.65	0.03	3158	8.69	0.60			
V1490 Ori	05:35:11.875	-05:45:37.76	4.041	0.001	1907	4.02	0.13	1791	4.04	0.004
V482 Ori	05:35:06.105	-05:45:30.97	8.326	0.004	1707	7.70	0.47	1710	4.18	0.008
COUP 172	05:35:02.006	-05:20:54.86	9.355	0.005						
JW 131	05:34:52.618	-05:15:36.27	2.351	0.002						
V1277 Ori	05:35:12.844	-05:15:23.80	9.04	0.02	1982	7.78	0.48			

Table 4.4: Some objects presenting interesting light curves, identified with the procedures developed in the present work

ID	RA(J2000)	DEC(J2000)
CHS2001 9298	05:35:19.562	-05:27:04.54
COUP 981	05:35:18.586	-05:26:24.96
V1500 Ori	05:35:14.895	-05:36:39.34
V982 Ori	05:35:06.429	-05:33:35.06
V381 Ori	05:37:02.354	-05:36:29.93
WY Ori	05:34:15.630	-05:32:23.90
R2001 759	05:33:45.406	-05:36:31.64
V1555 Ori	05:35:30.794	-05:30:36.40

4.5 Summary of Results

Surveys covering large areas and long timelines are very important for discovering new variable stars. We conducted such a survey in the Orion Nebula and the completion of our catalog of variable stars is near. The creation of this catalog presented many challenges, which were studied and conquered step-by-step.

The use of statistical indices proved to be useful when trying to separate the stars of a sample using their light curves. We were able to find variable stars with periodic modulation (rotational and pulsational) and also eclipsing binary candidates. The discovery of eclipsing binary candidates was, from the beginning, one of our main objectives. The next step is to plan follow up observations, both photometric and spectroscopic, in order to obtain precise stellar parameters, which are so important in our attempt to better comprehend how the stars are formed and how they evolve.

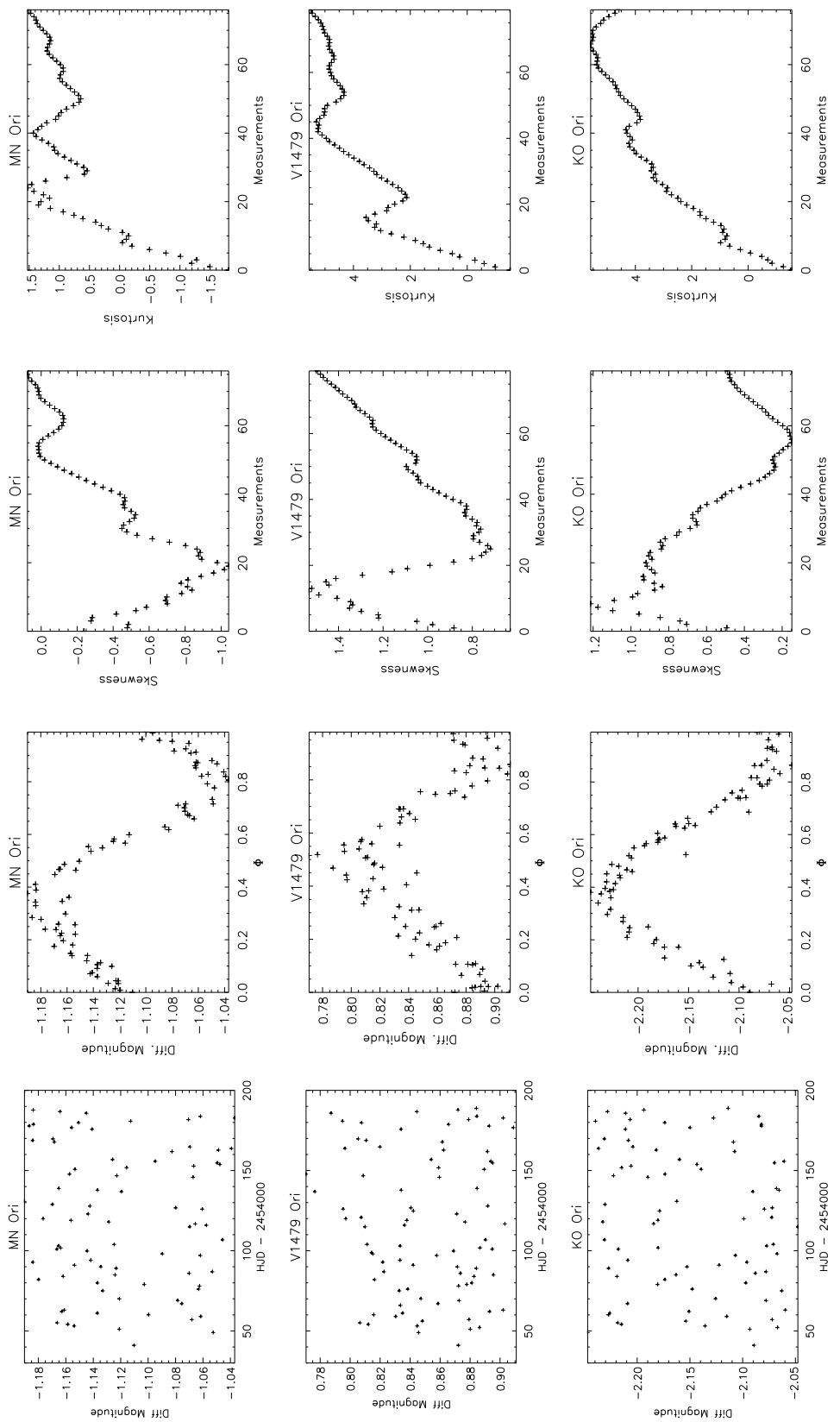

Figure 4.14: We present here the light curves, phased light curves, skewness and kurtosis curves (of the mean magnitudes) for the stars that presented rotation or pulsation.

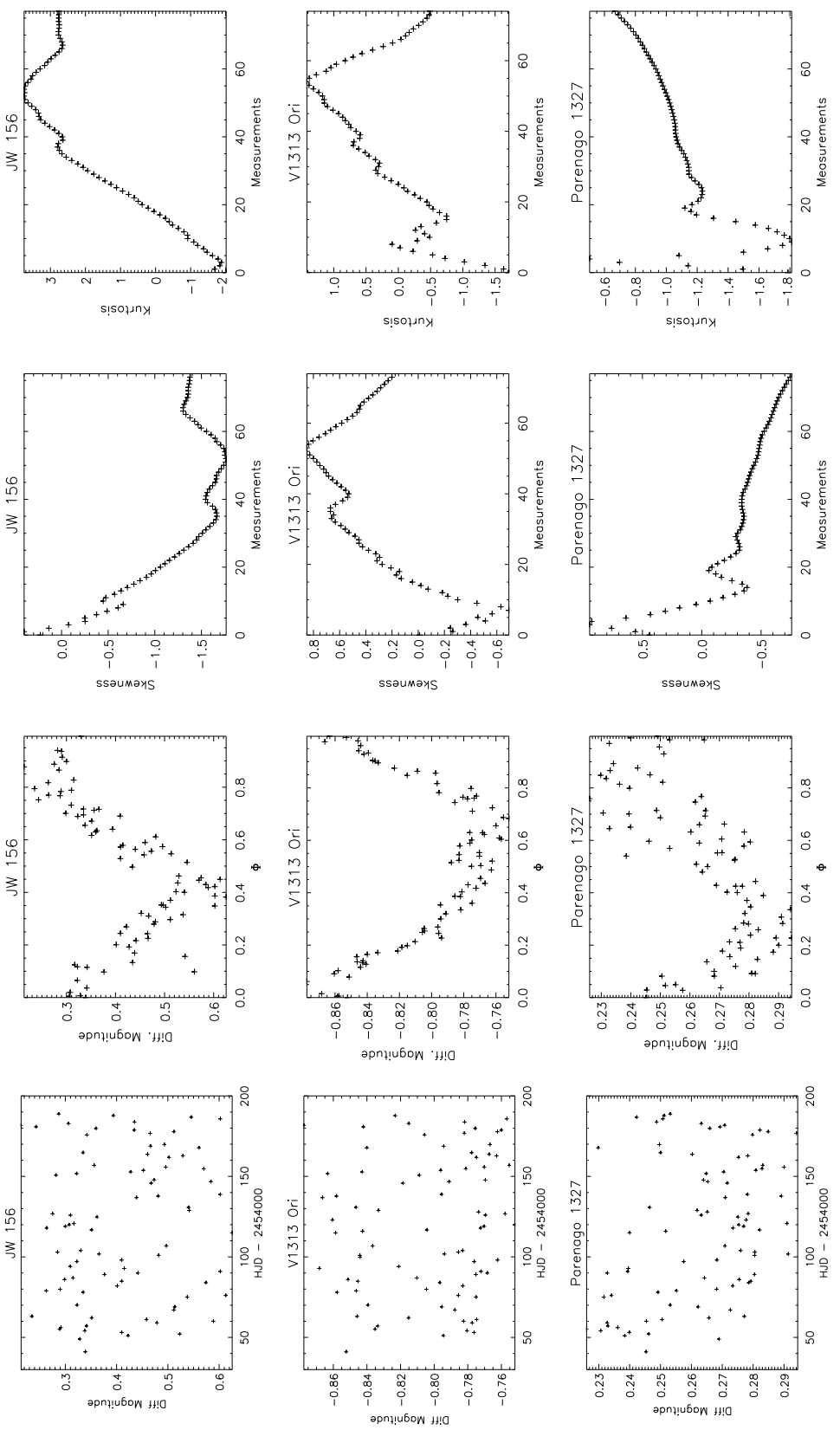

Figure 4.15: Same as in Fig. (4.14).

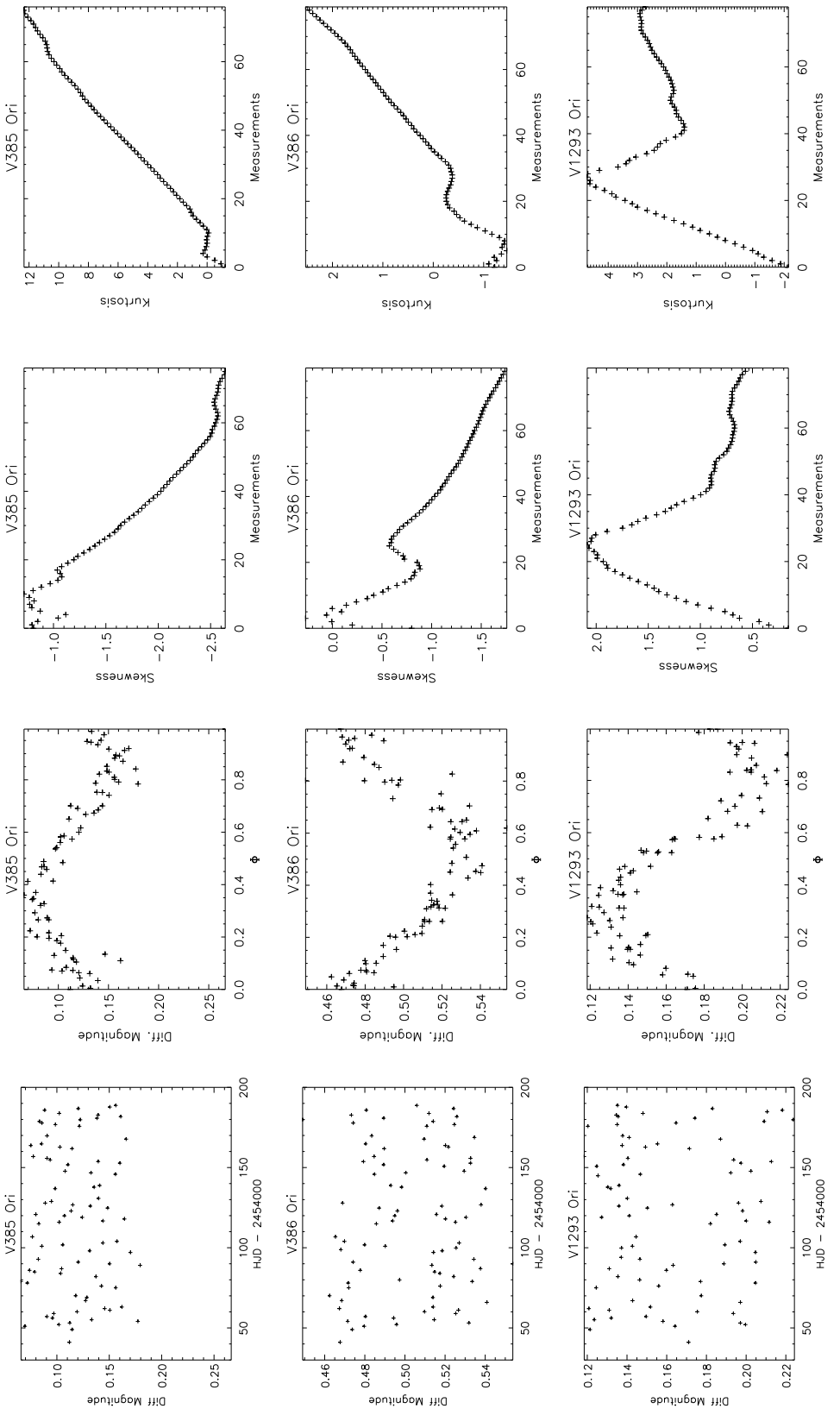

Figure 4.16: Same as in Fig. (4.14).

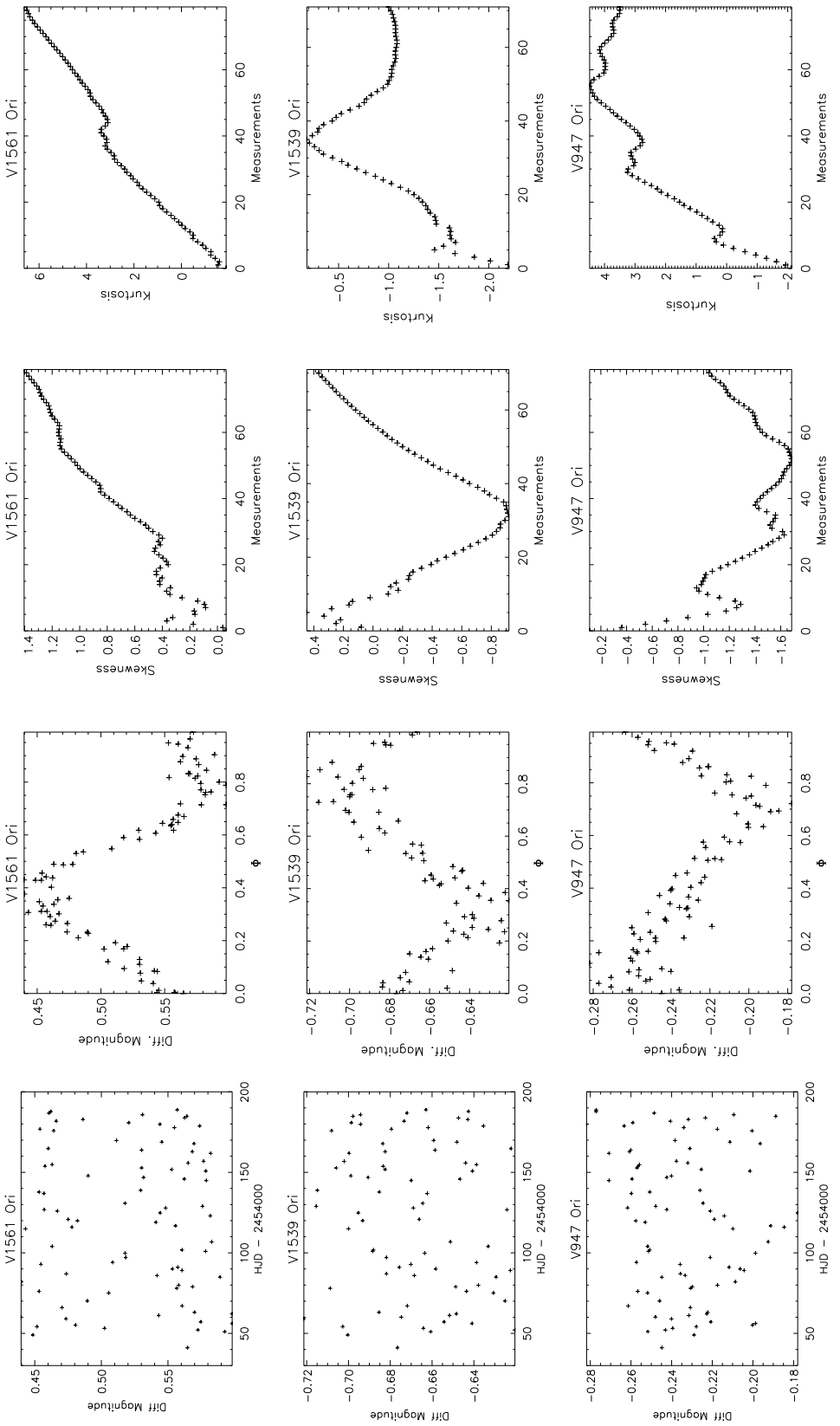

Figure 4.17: Same as in Fig. (4.14).

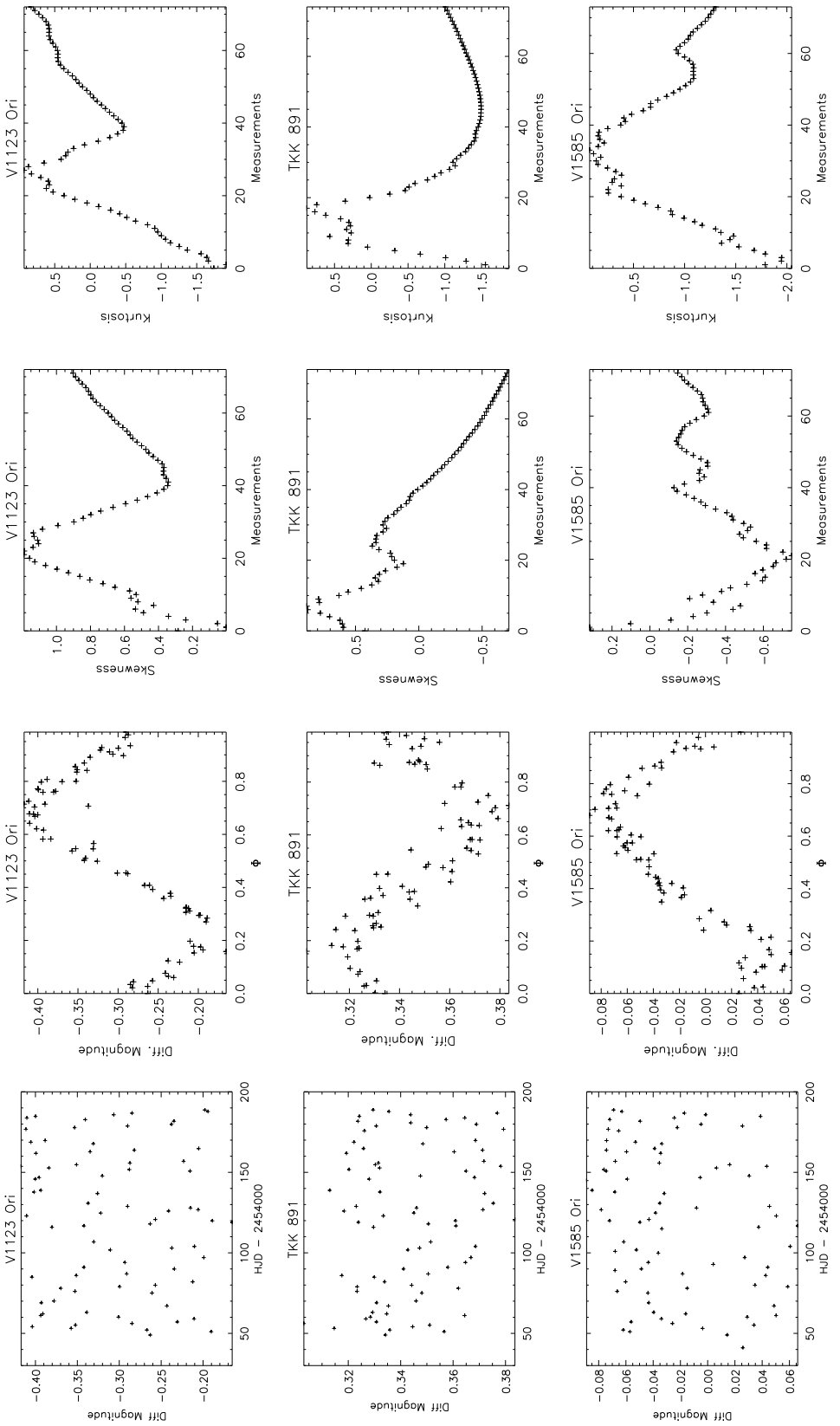

Figure 4.18: Same as in Fig. (4.14).

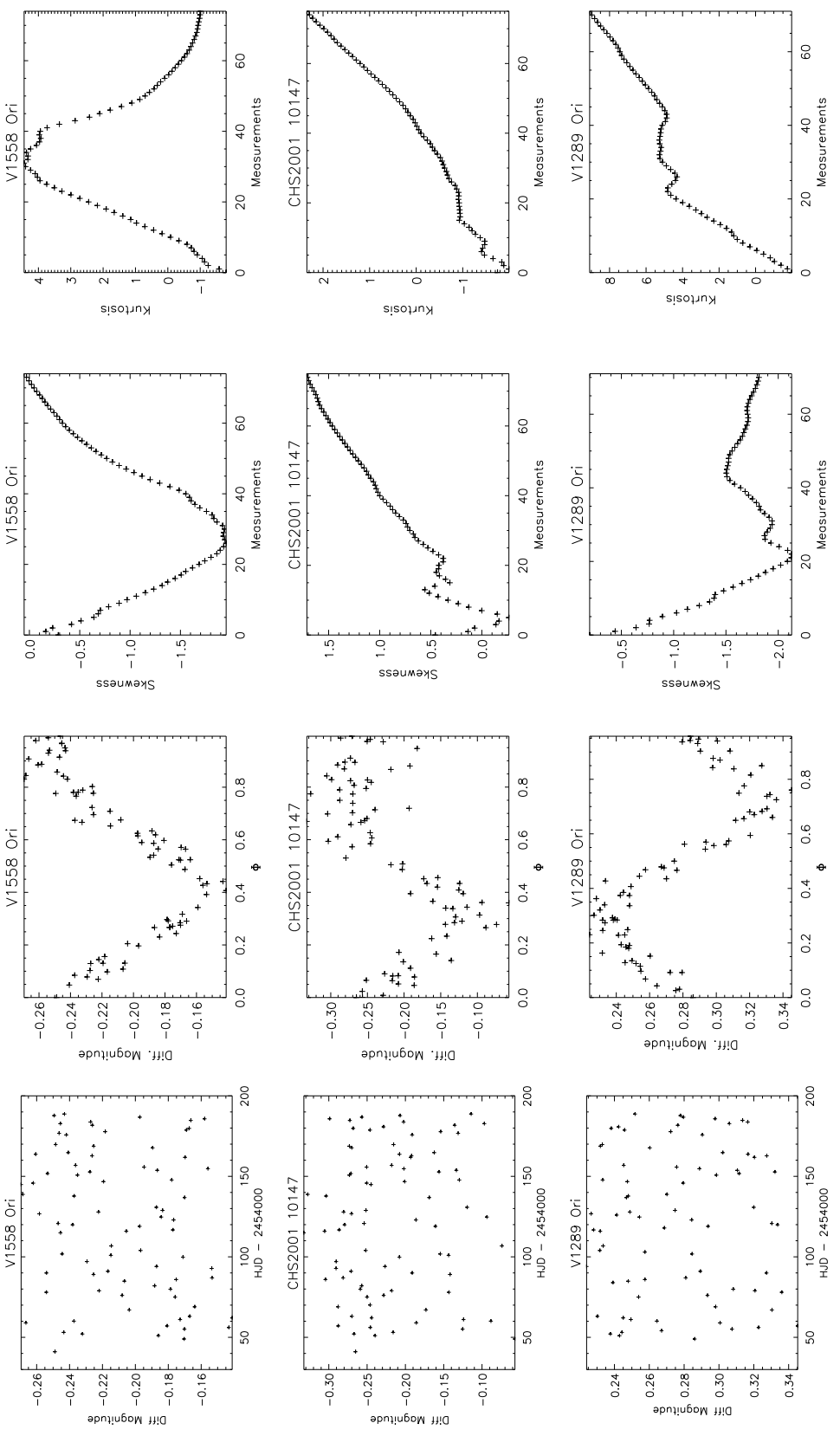

Figure 4.19: Same as in Fig. (4.14).

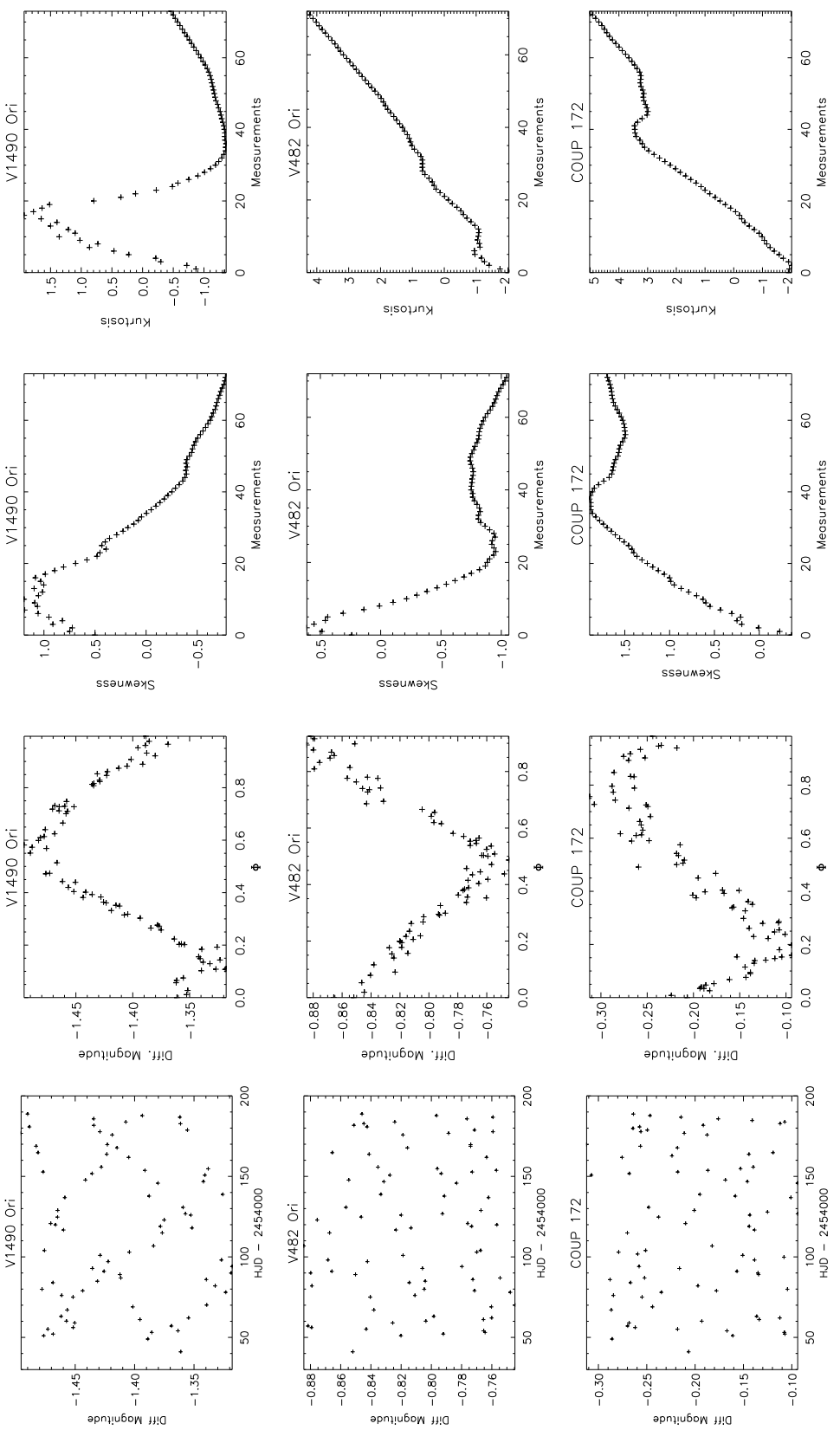

Figure 4.20: Same as in Fig. (4.14).

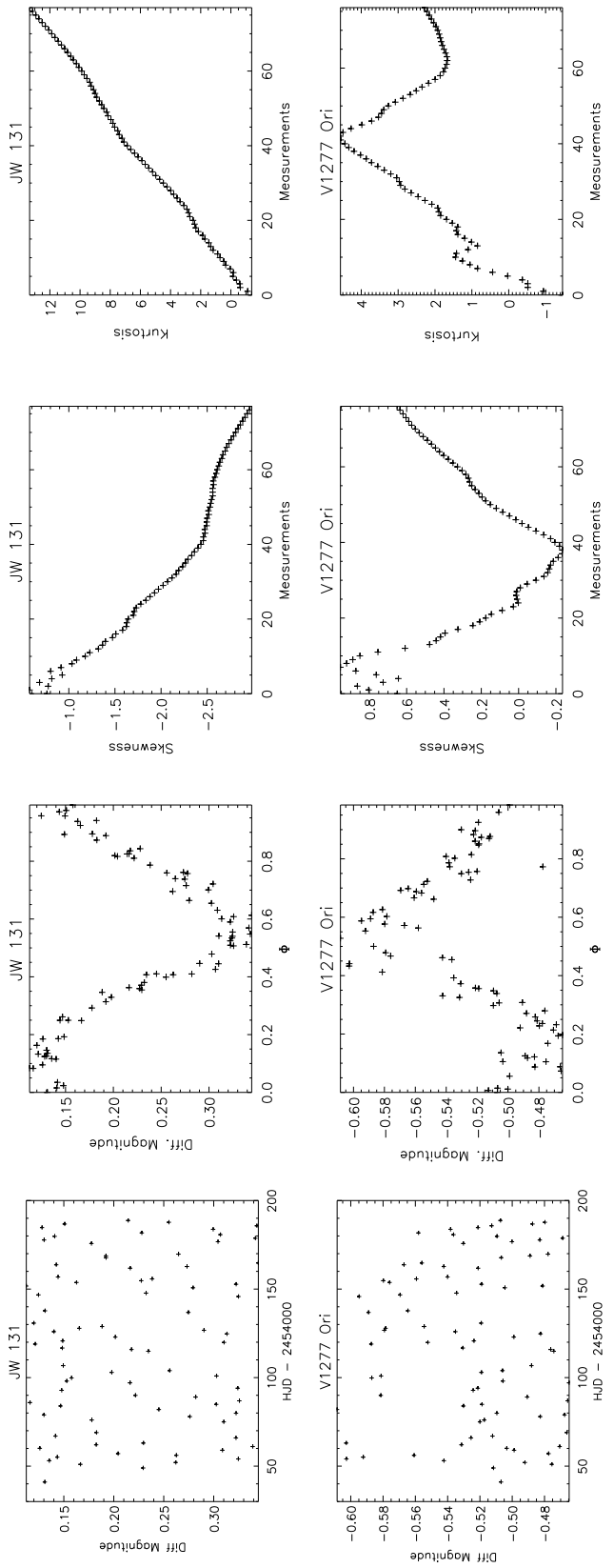

Figure 4.21: Same as in Fig. (4.14).

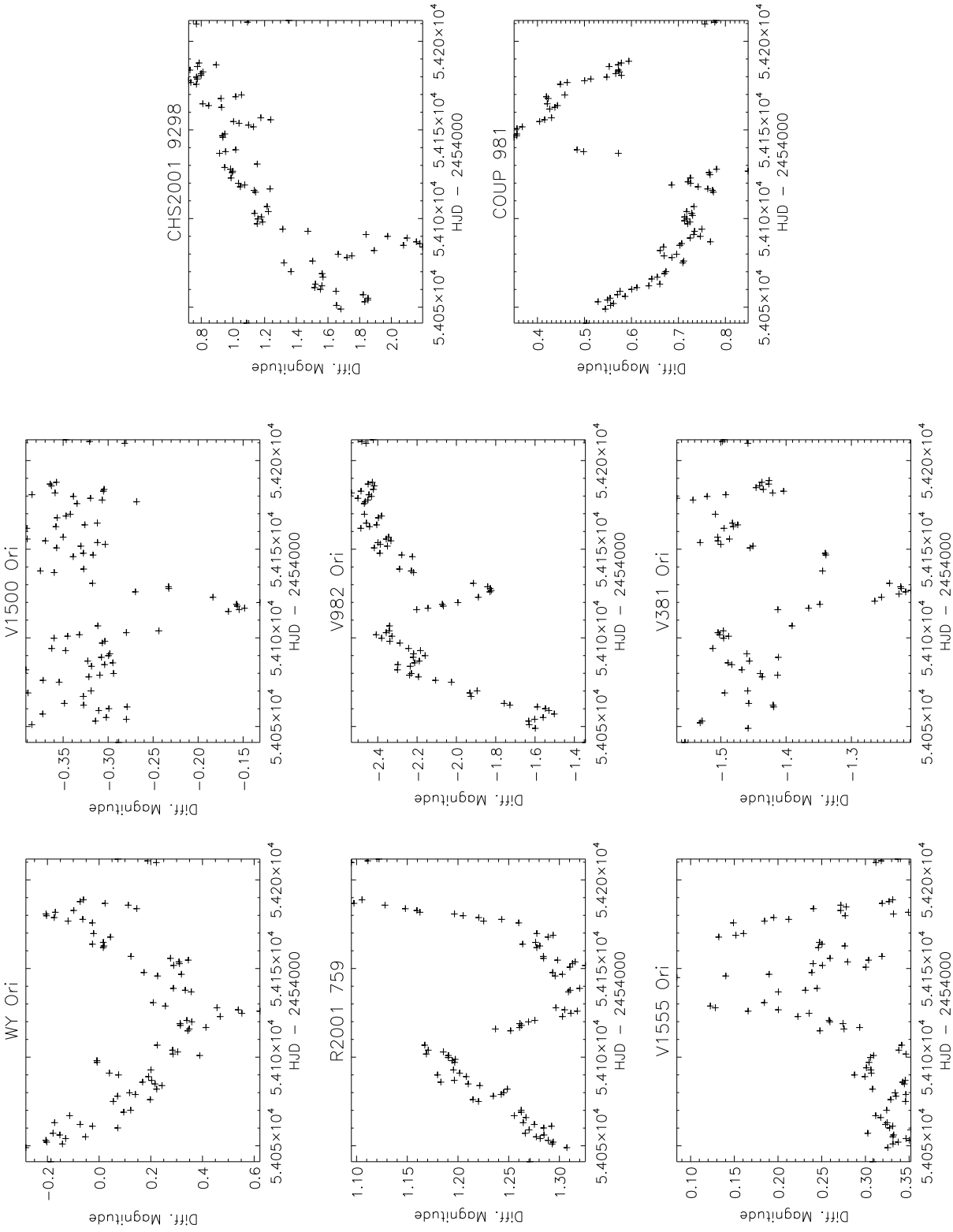

Figure 4.22: We show here examples of interesting light curves present in our sample.

Chapter 5

The Cygnus OB2 Survey

5.1 Introduction

One of the richest known star forming regions in the Galaxy is located in the direction of the Cygnus constellation and is known as Cygnus X. It is also one of the brightest areas of the sky in all wavelengths. When we look in that direction we are looking through the Local Spiral Arm and thus we are deluded by different star forming regions projected in the same area of the sky. Some of these star forming regions are situated at several hundred parsecs away while others are located in the other spiral arm, the Perseus Arm, a few thousand parsecs away. One of the most important regions in this area is the young OB association called Cygnus OB2.

Figure (5.1) shows an Hα image, taken from Schneider et al. (2006), that shows part of the Cygnus X region. The North America Nebula and the Pelican Nebula can be seen in the bottom right corner. The dark feature in the center of the image is the Great Cygnus Rift. The Cygnus OB2 association is located almost in the center of the rift. An extinction map toward this region can be seen in Figure (5.2), also taken from Schneider et al. (2006). In the center of the image we can see a circle delimiting the extent of Cygnus OB2, and also of other OB associations. The white circles with numbers on them are the radio continuum sources reported by Downes & Rinehart (1966). It is possible to see in Fig. (5.2) that the Cygnus OB2 association is located in a region of low extinction compared to its surroundings, although the values for A_V range from 5 to 20 magnitudes.

Cygnus OB2 was discovered by Münch & Morgan (1953), who called attention to this "possible association of blue giant stars". Many studies followed this pioneer work, Johnson & Morgan (1954) identified 14 association members as B1 stars or earlier, and Morgan, Meinel & Johnson (1954) and Schulte (1956a) identified 80 possible members which were later confirmed by Schulte (1956b, 1958) through UBV photometry. All studies pointed to the high extinction towards Cygnus OB2 ($\sim$5$-$20 magnitudes). A more comprehensive study was made by Reddish, Lawrence & Pratt (1966) who identified hundreds of stars, possible members, through the use of color-color diagrams. Torres-Dodgen, Tapia & Carroll (1991) and Massey & Thompson (1991) analyzed in detail the massive population and determined a distance of 1.7 kpc to the Cygnus

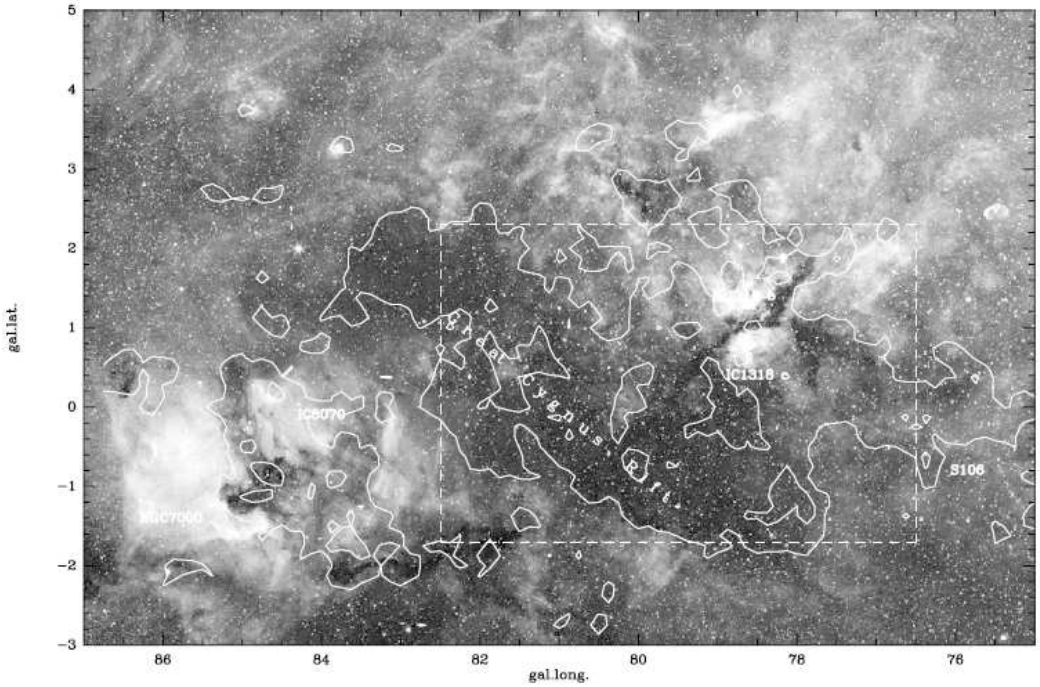

Figure 5.1: The Great Cygnus Rift in Hα, image taken from Schneider et al. (2006).

OB2 association. An age of 1 to 3 Myr was suggested based on the presence of O3 stars in the main sequence and evolved supergiants (Torres-Dodgen, Tapia & Carroll, 1991). Other studies suggest younger ages ($<$ 1 Myr) (e.g. Voelcker, 1974; Hutchings, 1981).

Cygnus X has been the target of many radio surveys: Westerhout (1958) at 1390 MHz, Downes & Rinehart (1966) at 5 GHz, Wendker (1984) and Wendker, Higgs & Landecker (1991) at 408, 1420 and 4 800 MHz, Taylor et al. (1996) at 327 MHz, Taylor et al. (2003) at 1420 MHz. Some of the most massive stars in Cygnus OB2 were detected as non-thermal radio emitters.

Through the use of 2MASS infrared observations, Knödlseder (2000) suggested that Cygnus OB2 should be considered a young globular cluster, based on the number of OB stars ($\sim$2600 $\pm$400 stars, among which $\sim$120$\pm$20 are O stars), its spherical geometry and its youth (1$-$3 Myr). Knödlseder (2000) also suggested that the geometric shape of the association was misinterpreted by Reddish, Lawrence & Pratt (1966) because of the high extinction in the optical band. Knödlseder (2000) argues that CygOB2 is too compact to be an OB association and too massive ($4-10\times10^4 M_\odot$) to be an open cluster. Its spherical morphology and high central density indicate that CygOB2 is a young globular cluster. Later, Knödlseder et al. (2002) reclassified Cygnus OB2 as a supercluster, similar to the Arches and Quintuplet clusters (Figer et al., 1999), NGC 3603 (Moffat, Drissen & Shara, 1994) and W94A (Conti & Blum, 2002). Hanson (2003) made a study of the more massive Cygnus OB2 members and stated that many OB stars do not belong to the association. For these authors the O population is smaller than the one proposed by Knödlseder (2000) and thus Cygnus OB2 would not be a supercluster.

We summarize the properties of this unusual association, following Knödlseder (2000), in Table (5.1). Figure (5.3) shows the stellar density distribution derived from the 2MASS point source catalog (left panel) and from the DSS red plates (right panel) as shown by Knödlseder (2000). Darker regions correspond to higher densities. It is clear in Figure (5.3) why Reddish,

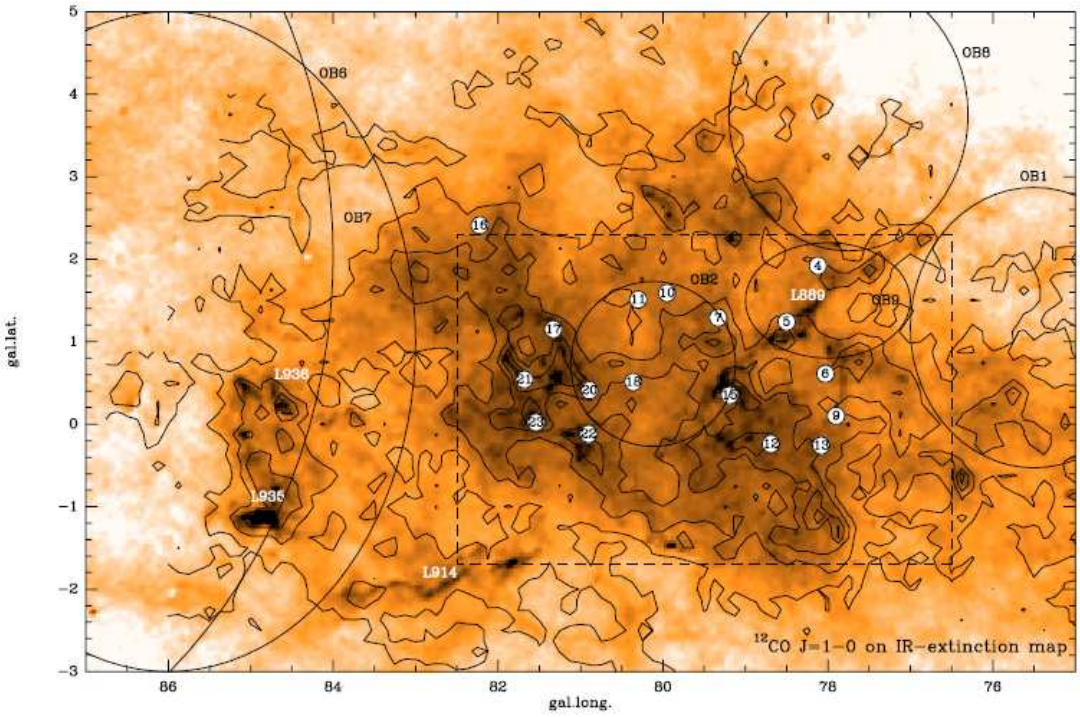

Figure 5.2: The Great Cygnus Rift, extinction map taken from Schneider et al. (2006). The white circles represent the radio continuum sources detected by Downes & Rinehart (1966).

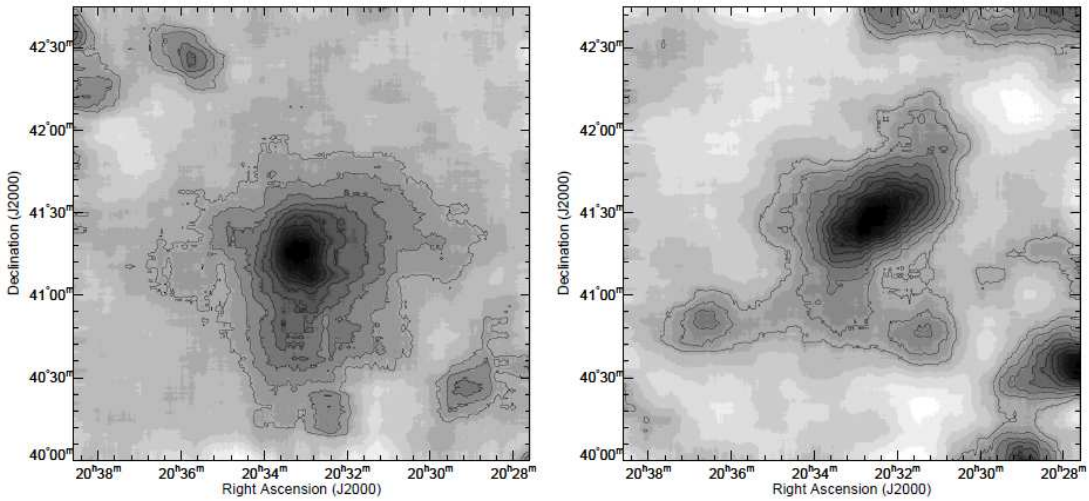

Figure 5.3: Cygnus OB2 star density map. The left panel shows the 2MASS data while the right panel shows the DSS red plates data. The image was taken from Knödlseder (2000).

Lawrence & Pratt (1966) misinterpreted the shape of the Cygnus OB2 region, extinction hides most of the association in the optical bands.

Drew et al. (2008) identified the on-sky distribution of over 1000 A0-A5 stars towards, around, within and beyond Cygnus OB2. They have found a peak in A-star density ($\sim$ 200 stars) roughly centred on RA 20:32:00 DEC +41:00:00, $\sim$ 20 arcmin south of the Cygnus OB2 Trapezium. The Trapezium is composed of four stars named Schulte 8A, Schulte 8B, Schulte 8C and Schulte 8D, there is also a fifth star, named [MT91] 893, which was not catalogued by Münch

Table 5.1: Cygnus OB2 properties, following Knödlseder (2000)

center	RA 20:33:10, DEC +41:12:00
diameter	$\sim 2^{\circ}$ (~ 60 pc at a distance of 1.7 kpc)
half light radius	$13'(6.4pc)$
core radius	$29' \pm 5'(14 \pm 2\mathrm{pc})$
tidal radius	$93' \pm 20'(46 \pm 10\mathrm{pc})$
members earlier F3V	8600 ± 1300
OB star members	2600 ± 400
O star members	120 ± 20
total stellar mass	$(4-10) \times 10^4 \mathrm{M}_{\odot}$
central mass density	$40 - 150 \mathrm{M}_{\odot}\mathrm{pc}^{-3}$
IMF slope	-1.6 ± 0.1

& Morgan (1953); Morgan, Meinel & Johnson (1954); Schulte (1956a,b), but was catalogued by Massey & Thompson (1991). Drew et al. (2008) also identified the on-sky distribution of the reddenings for the same sample. Treating the A stars and OB stars as part of the same cluster, Drew et al. (2008) found a distance of 1.4 kpc, if the A stars are 7 Myr old, or 1.7 kpc if they are 5 Myr old. Either way, these authors find a difference between the age of the A stars and OB stars, the later ones supposedly 1−3 Myr old. Based on the findings of Drew et al. (2008) we can think about the possibility of two bursts of star formation in Cygnus OB2 or a substantial age spread in the association.

Knödlseder et al. (2002) suggest that the gamma-ray and free-free emission in the Cygnus region seems to be dominated by the Cygnus OB2 association. It would be responsible for 75% of the ionization in Cygnus but would account for only 20% of the observed 1.809 Mev photons. Knödlseder et al. (2002) also rose some doubt about the suggested scenario used to explain the anomalous stellar proper motions in the Cygnus area (Comerón & Torra, 1994). In the suggested scenario, the winds and supernovae of the Cygnus OB2 association would be responsible for the formation of the surrounding associations: Cygnus OB1, OB3, OB7 and OB9. However, the age estimated by Knödlseder et al. (2002) is inferior to that of the surrounding associations. Knödlseder et al. (2002) suggested that the runaway stars could be a possible explanation for the anomalous stellar proper motions. However, Kiminki et al. (2007) did not find any runaway star in Cygnus OB2 in their radial velocity survey.

The optical counterparts for the first X-ray sources, found by the Einstein satellite, were massive stars in the Cygnus OB2 association (Schulte 5, Schulte 8A, Schulte 9 and Schulte 12). The same field was also observed by ROSAT, ASCA and Chandra (De Becker et al., 2006). More recently Albacete Colombo et al. (2007) used data from the Chandra satellite to unveil the low mass population. They found that Cygnus OB2 has a very rich population of low-mass X-ray emitting stars, but the circumstellar disks are scarce. The X-ray activity is comparable to the activity in the ONC.

Wendker, Higgs & Landecker (1991) did not detect any evidence of supernova remnants in the area. This evidence implies that the association is still too young, maybe less than 1 Myr. High mass evolved stars are present in the association and could be the first of this area to become supernovas.

There is a lack of an HII region in the center of Cygnus OB2 and an explanation for this fact is still missing. Wendker, Higgs, & Landecker (1996) have found what appears to be two cometary HII regions close to the center of Cygnus OB2.

Table 5.2: Observation dates of the Cygnus OB2 survey.

April	01	03	04	05	06	07	08	09	10	11	12	13	14	15	16	17
	18	19	20	21	22	23	25	26	27	28	29	30				
May	01	02	03	04	05	06	07	08	09	10	11	14	18	19	20	21
August	04	05	06	07	08	09	10	11	12	18	19	20	21	22	23	24
	26	27	28	30	31											
September	12	13	14	15	16	17	18	19	20	21	22	23	24	25	29	30
October	01	02	03	04	06	07	08	09	10	11	12	13	14	15	16	17
	19	20	21	22	24	25	26	27								
November	01	02	03													

Schulte 8A was discovered as a binary by De Becker et al. (2006) and consists of an O6 If star plus an O5.5 III(f) star. It is an eccentric system with e=0.24±0.04 and a period of 21.908±0.040 d. The semi-major axis is 142±6 $R_\odot$. The fact that Schulte 8A is a binary could reconcile the high bolometric luminosity reported by Herrero, Puls & Najarro (2002) with its spectral type (O5.5 I(f)) found at that time, when thought to be a single star.

Nazé et al. (2008) reported the detection of a companion, in an eccentric orbit, to the star Schulte 9, using radial velocity measurements. The period of 2.355 years is consistent with the radio measurements reported by Van Loo et al. (2008), which used VLA data since 1980.

Kiminki et al. (2007) made a radial velocity survey, with a 6 year interval, in search for massive contact binaries. A total of 146 OB stars were observed and 73 were identified as new early-type stars. Using these stars they obtained a distance modulus of 11.3 and an IMF slope ∼-2.2±0.1. Few differences between the spectral classification of previously known members were found, except for the stars Schulte 12 and Schulte 21. Schulte 12 is classified as a B3 Iae with a temperature class variation of B3 – B8 in an interval of one year. Schulte 21 was previously classified as a B1 V and the spectral classification changed to B0 Ib. Kiminki et al. (2007) obtained a massive binary frequency of 30% – 42% and detected no obvious OB runaways.

Most of the observations of Cygnus OB2 concern the high mass population and little attention has been given to the low and intermediate mass population. High resolution deep surveys must be done in order to better determine the total population of this incredible star forming region. We have conducted such survey in the infrared band using the WFCAM. Our survey does not intend to be too deep but has enough resolution to resolve many objects and help us to better determine the real population of Cygnus OB2. The long duration of the survey will allow us to unveil the variable population of this massive association.

5.2 Observations

The observations were performed with the WFCAM (see description in Chapter 4) from April until November 2007. The procedure is identical to the one used in the Orion Nebula. This project also uses only some minutes each night, with expositions lasting only 2 seconds. Table (5.2) presents the dates of observation.

Access to the final pipeline reduction data was granted to us in January 2008. We retrieved the images and catalogs from the CASU server and began analyzing its composition. It became clear to us that the catalogs needed to be reorganized in order to build light curves for the stars. The IDL routines developed to deal with the Orion Nebula data were adapted to deal with the

Cygnus OB2 data. The first problem was the difference in the catalog structure. Because the Orion data was reduced using the summit pipeline, the catalogs have a different structure from those created by the final pipeline. The Cygnus OB2 catalogs are stored in multi-extension FITS files as FITS binary tables which were read using the IDLASTRO routine called *ftab.pro*. Each FITS file has 4 extensions, one for each CCD. Each fits table consists of 80 columns with the relevant parameters (described below) for each object.

N	Name	Description
1	Sequence number	running number for ease of reference, in strict order of image detections
2	Isophotal flux	standard definition of summed flux within detection isophote, apart from detection filter is used to define pixel connectivity and hence which pixels to include. This helps to reduce edge effects for all isophotally derived parameters
3	X coordinate	intensity-weighted isophotal centre-of-gravity in X
4	X coordinate err	estimate of centroid error
5	Y coordinate	intensity-weighted isophotal centre-of-gravity in Y
6	Y coordinate err	estimate of centroid error
7	Gaussian sigma	these are derived from the three general intensity-weighted second moments
8	Ellipticity	the equivalence between them and a generalised elliptical Gaussian
9	Position angle	distribution is used to derive Gaussian sigma = $(\sigma_a^2 + \sigma_b^2)^{1/2}$ ellipcity = $1.0 - \sigma_a/\sigma_b$ position angle = angle of ellipse major axis wrt x axis
10	Areal 1 profile	number of pixels above a series of threshold levels relative to local sky.
11	Areal 2 profile	levels are set as T, 2T, 4T, 8T ... 128T where T is the threshold.
12	Areal 3 profile	
13	Areal 4 profile	
14	Areal 5 profile	
15	Areal 6 profile	
16	Areal 7 profile	
17	Areal 8 profile	
18	Peak height	in counts relative to local value of sky - also zeroth order aperture flux
19	Peak height err	estimate error of peak height
20	Aper flux 1	Fitted flux within 1/2* core radius
21	Aper flux 1 err	Error in fitted flux within 1/2* core radius
22	Aper flux 2	Fitted flux within 1/sqrt(2)* core radius
23	Aper flux 2 err	Error in fitted flux within 1/sqrt(2)* core rad
24	Aper flux 3	Fitted flux within 1* core radiu
25	Aper flux 3 err	Error in fitted flux within 1* core radiu
26	Aper flux 4	Fitted flux within sqrt(2)* core radius
27	Aper flux 4 err	Error in fitted flux within sqrt(2)* core rad
28	Aper flux 5	Fitted flux within 2* core radius
29	Aper flux 5 err	Error in fitted flux within 2* core radius
30	Aper flux 6	Fitted flux within 2*sqrt(2)* core radius
31	Aper flux 6 err	Error in fitted flux within 2*sqrt(2)* core rad
32	Aper flux 7	Fitted flux within 4* core radius
33	Aper flux 7 err	Error in fitted flux within 4* core radius
34	Aper flux 8	Fitted flux within 5* core radius
35	Aper flux 8 err	Error in fitted flux within 5* core radius
36	Aper flux 9	Fitted flux within 6* core radius
37	Aper flux 9 err	Error in fitted flux within 6* core radius
38	Aper flux 10	Fitted flux within 7* core radius
39	Aper flux 10 err	Error in fitted flux within 7* core radius
40	Aper flux 11	Fitted flux within 8* core radius
41	Aper flux 11 err	Error in fitted flux within 8* core radius
42	Aper flux 12	Fitted flux within 10* core radius
43	Aper flux 12 err	Error in fitted flux within 10* core radius
44	Aper flux 13	Fitted flux within 12* core radius
45	Aper flux 13 err	Error in fitted flux within 12* core radius
46	Petr radius	
47	Kron radius	
48	Hall radius	
49	Petr flux	
50	Petr flux err	
51	Kron flux	
52	Kron flux err	
53	Hall flux	
54	Hall flux err	
55	Error bit flag	bit pattern listing various processing error flags
56	Sky level	local interpolated sky level from background tracker
57	Sky rms	local estimate of variation in sky around image
58	Parent or child	flag for parent or part of deblended deconstruct
59	RA	Right ascension
60	DEC	Declination
61	Classification	flag indicating most probable morphological classification: -1 stellar, +1 non-stellar, 0 noise, -2 borderline stellar, -9 saturated
62	Statistic	An equivalent N(0,1) measure of how stellar-like an image is, used in deriving 61 in a necessary but not

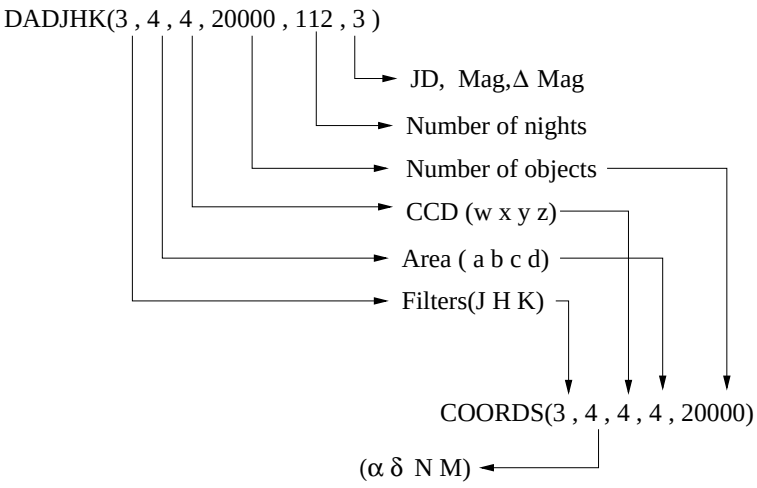

Figure 5.4: DADJHK and COORDS, layout of the tables containing all the astrometric and photometric information.

```
                    sufficient sense.
From column 63 to 80 our fields are blank.
```

Right at the beginning of our work with the tables it became clear to us that we should deal with the catalogs for the Cygnus OB2 region in a different way than the one used for Orion. The main reason was the amount of data present in each CCD exposure. While we had $\sim$ 500 detections per CCD in the Orion survey, for Cygnus OB2 the average number is $\sim$ 10 000. Such a huge amount of data required an enormous amount of time, both computational and personal, to be organized. Usually, one observation requires approximatelly 40 hours of work to be processed.

The tables were organized in two different catalogs, one called *coords* which contains the coordinates and another called *dadjhk* which contains the photometry. Figure (5.4) shows the internal structure of the catalogs.

We decided to separate the tables into two catalogs because the process of detection in the pipeline does not create a unique ID for each object. The pipeline procedure reads the mosaic starting in filter J, Area 'a', and CCD 'w', the procedure ends in Area 'd', CCD 'z', after that the next filter is H and the last is K. The first object detected in the first filter, first area, first CCD, does not coincide with the first object detected in the second filter, first area, first CCD. Actually, the first object detected in each of the filters, areas and CCDs does not coincide with the first object of the same filters, areas and CCDs of the next night. To find each object detected in one night in the subsequent night it is necessary to search through the whole respective table of that filter, that area, that CCD. Figure (5.5) shows the layout of the WFCAM mosaic and the reading steps through the CCDs and Areas.

We used the Classification Flag (ID 61 in the FITS header) to help us with the classification of the objects. We noticed that they are not perfect, as one would expect. Some objects with flag '0' (noise) were actually stellar objects while some objects with flag '-1' (stellar) were noise or defects. At the beginning of the procedure we checked every point source and as we learned the behavior of the objects we decided to restrain some parameters and make the procedure a bit more automatic. Given a magnitude interval and a given error, if the object presents the '-1' flag it was automatically accepted. Objects inside this interval but with different flags were

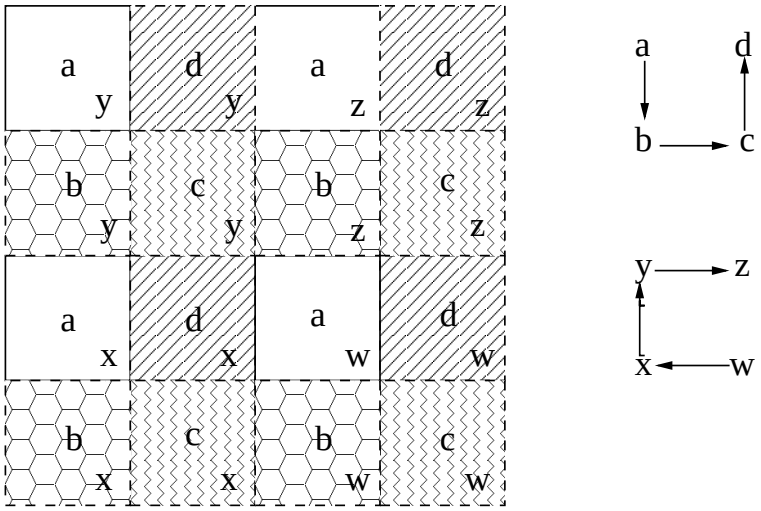

Figure 5.5: WFCAM layout and reading scheme

checked everytime.

The IDL procedure evolved during our work with the tables. Because of the huge amount of data per CCD it was necessary to develop control loops for each CCD, each area, each filter and each night. We ended with a procedure that allows us to stop and save the data almost anytime we want. These cautions were necessary because of energy blackouts that would sometimes occur in the middle of an unsaved 10 000 star loop.

The process became faster when we started the second night, because objects that matched an already catalogued source were accepted automatically. New objects went through the same process as in the first night.

The third night was the best night concerning seeing and sky transparency. We achieved very good resolution and many new objects were catalogued, which slowed down the cataloging process. Five days were necessary to finish the third night.

The fourth night catalogation was slower than the third night because of the increase in the number of objects catalogued. Also, since the third night has better resolution it resolved objects that were previously seen as single stars. Every time the procedure finds catalogued object inside a circle of $1''$ from the object being analyzed, it asks which entry is the correct one. Five days were also necessary to finish the fourth night. Our estimate is that this process will take an average of five days of work per observed night.

One step used in the Orion survey was not necessary for Cygnus OB2 because of the efficiency of the final pipeline. Because the Orion data was reduced using the summit pipeline, it was necessary to shift the coordinates for each CCD in order to correct the distortions, explained in Chapter 4. The final pipeline already corrected these distortions and no shifts were necessary. This was a major evolution in the procedure because the time required to shift $\sim$10 000 coordinates was huge. We tested the shifts in the beginning of the second night and they took almost half an hour on the fastest computer we have available. Assuming 30 minutes for each shift and 48 shifts per night, we would spend 24 hours only calculating the shifts.

Since the process was slow, even without the shifts, we decided to postpone the variability analysis to a near future. We will concentrate here on the analysis of the Cygnus OB2 region which is poorly studied so far, compared to a region like the ONC. We have found evidences

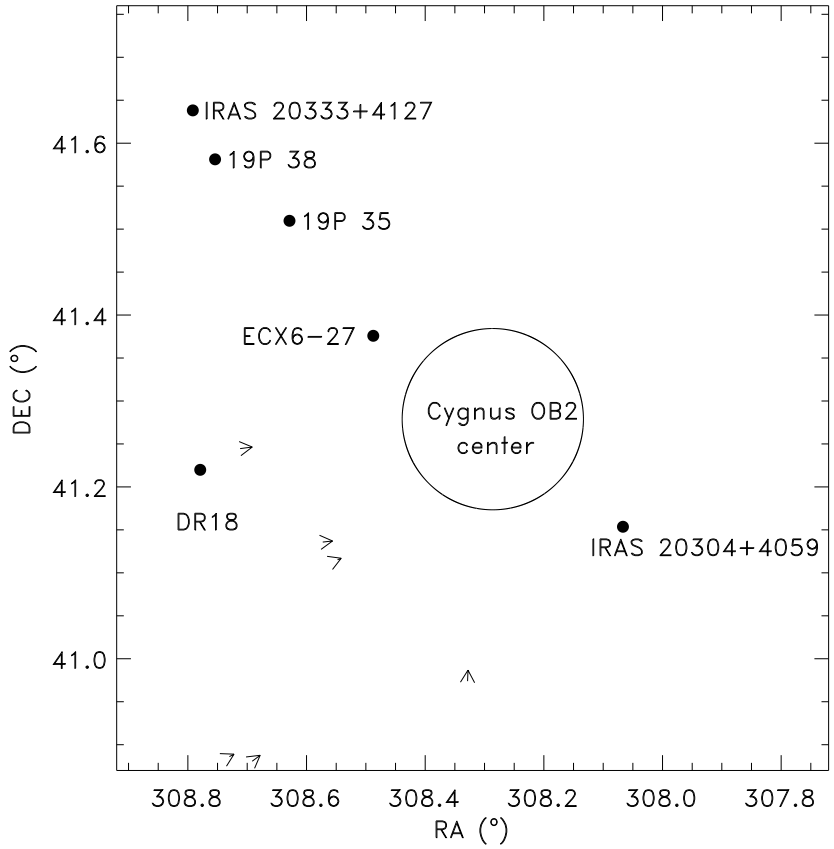

Figure 5.6: The infrared sources revealed in our survey are displayed in this figure as filled circles. The sources are labeled using IDs found in the literature. The arrows in the bottom of the image represent the cometary globules we have found in our survey, the size of the arrow bodies correspond to the size measured from the head to the tail of the globule.

that corroborate the youth status of the association. Our goal in this chapter is to show that there are many regions in this area where star formation is still happening. Also, Cygnus OB2 harbors some of the most massive stars in the Galaxy. If we want to understand the upper part of the initial mass function, we need to study in detail the stars in this region.

We would like to point out, however, that the results presented in this chapter are preliminary, though they give us a glimpse of the importance of this survey. Figure (5.6) shows the distribution of the infrared sources and small scale cometary globules we have found during our study.

5.3 Cometary Globules

We have found six small scale cometary globules in our K-band images. The existence of such objects is definitive evidence that star formation happened not so long ago in Cygnus OB2. The cometary globules' tails point radially away from the center of the OB association, as shown in Figure (5.6). We named them using the coordinates of their heads in sexagesimal format: CGhhmmss+ddmmss. Table (5.3) presents their names, the angle between their head and tail, measured in the same way as the position angle (vide position angle in Chapter 2) and their

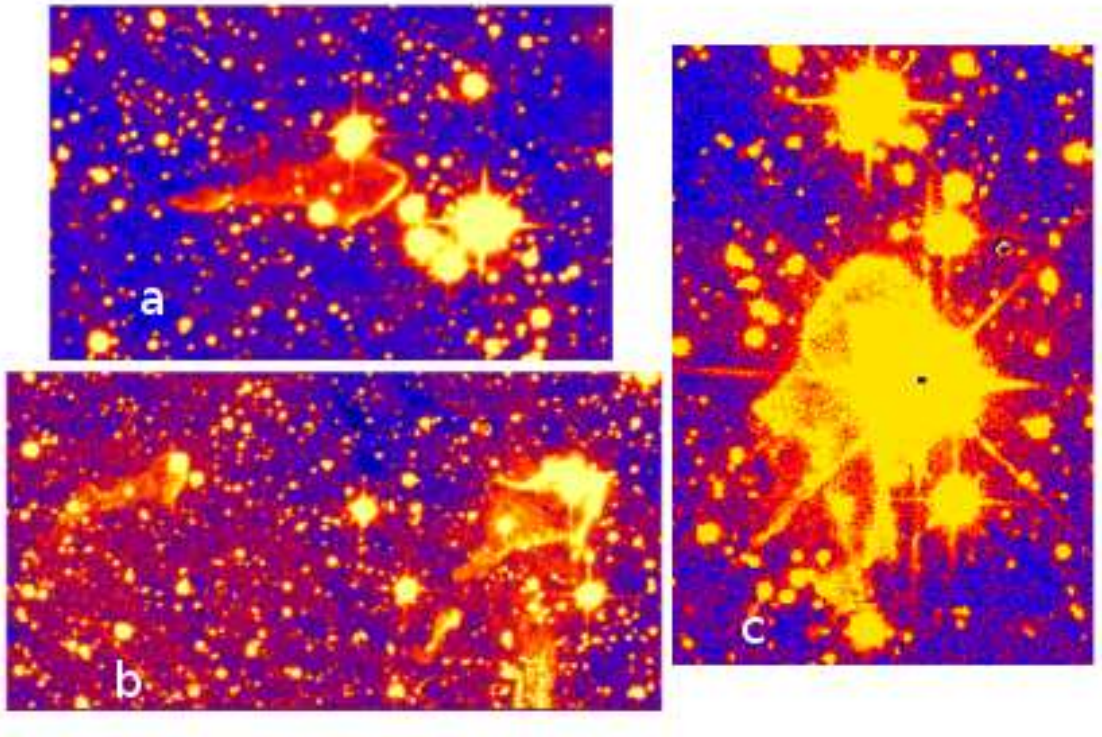

Figure 5.7: Cometary globules CG203446+411446 (panel a), CG203453+405320 and CG203442+405115 (left and right on panel b) and CG203318+405911 (panel c).

extent in arcseconds and parsecs. To calculate the extent in parsecs we used a distance of 1.7 kpc, meaning that we associate the cometary globules with the Cygnus OB2 association.

Table 5.3: Cometary globule ID, coordinates, position angle and assumed size.

ID	α(J2000)	δ(J2000)	PA	Extent($''$)	Extent(pc)
CG203318+405911	20:33:18.7	+40:59:11.8	177°.6	46.14	0.38
CG203410+410700	20:34:10	+41:07:00	110°.6	17.82	0.15
CG203413+410813	20:34:13.3	+41:08:13.9	95°.8	44.83	0.37
CG203446+411446	20:34:46	+41:14:46.6	96°.7	55.60	0.46
CG203442+405115	20:34:42.6	+40:51:15.9	124°.4	44.20	0.36
CG203453+405320	20:34:53.3	+40:53:20.3	115°.7	23.78	0.20

We show here the K-band images with a false color scale which helps us to see the cometary globules. Figure (5.7) presents four cometary globules. The cometary globule shown in panel (a) (CG203446+411446) was found close to the beautiful nebulosity associated to the DR18 radio source, which is presented in Figure (5.14). We will discuss this nebulosity in a specific subsection.

Panel (b) presents two globules whose tails point in the same direction (CG203453+405320, left; CG203442+405115, right). Both globules have a very reddened star in their heads, which are probably associated with them.

Panel (c) presents a globule (CG203318+405911) with a very bright star in front of it. They are likely not associated since we cannot detect any kind of ionization or reflection in the globule. The bright star is probably associated with Cygnus OB2, but its alignment with the globule is just a projection in the plane of the sky.

Figure (5.8) shows two globules, whose tails also point in the same direction, although the tail of the bottom one (CG203410+410700) is less pronounced. The top one (CG203413+410813) seems to be associated with some very reddened stars in its head and it is possible to see some curvature in its tail.

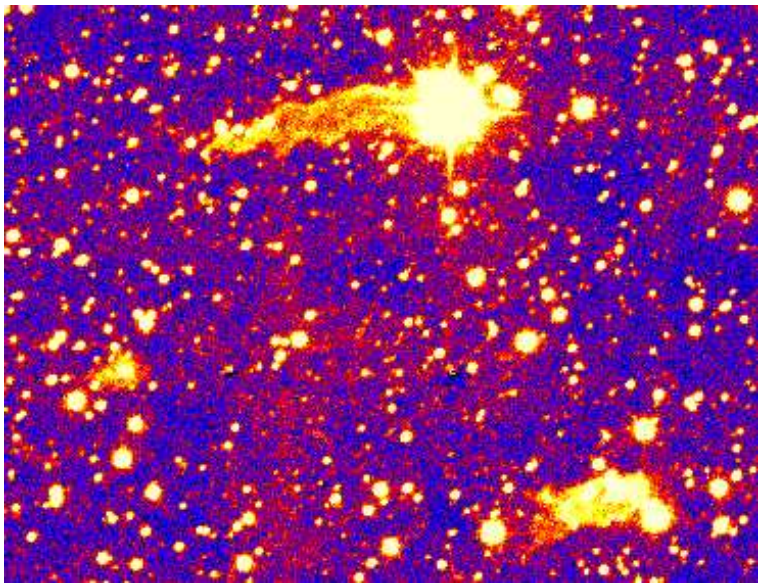

Figure 5.8: Cometary globules CG203410+410700 (bottom) and CG203413+410813 (top). Both globules are associated with red stars in their heads.

5.4 The Cygnus OB2 Center

We show in Figure (5.9) a composite color picture of the center of the Cygnus OB2 association, where it is possible to see the large number of blue stars that characterize the region.

Bica, Bonatto & Dutra (2003) suggested that the center of the Cygnus OB2 association harbors two new open clusters, one centred in coordinates RA 20:33:10 DEC +41:13:07 and the other at RA 20:33:15 DEC +41:18:45. In Fig. (5.9) the first cluster corresponds to the dense concentration of blue stars in the bottom-center part and the second cluster corresponds to the less dense concentration of blue stars in the top-center. It is possible to see a line of very bright saturated stars in the center of the picture. These stars are members of the association, but they were not considered by Bica, Bonatto & Dutra (2003).

Bica, Bonatto & Dutra (2003) used DSS images and 2MASS photometry to characterize these clusters. They also used the available spectroscopy and optical photometry of the stars in the area to help constrain the reddening and distance to the clusters. They concluded that both objects have the same distance and age.

It is possible to detect these concentrations of stars, considered by Bica, Bonatto & Dutra as two open clusters, in our infrared images. We will use our photometry to study the stars in these two regions and try to determine their association with Cygnus OB2. Our survey seems to corroborate the work done by Bica, Bonatto & Dutra.

Figure 5.9: Center region of the Cygnus OB2 association. The first cluster proposed by Bica, Bonatto & Dutra (2003) corresponds to the concentration of blue stars in the bottom-center of the figure. The second cluster corresponds to the top-center concentration. The very bright blue stars in the center, which are members of the association, were not taken into account by the authors.

5.5 Infrared Sources

The K band images allowed us to observe infrared (IR) sources within the Cygnus OB2 region. As said previously, because of the projection of this region in the direction of the Local Arm, some of these sources may not be associated with Cygnus OB2.

Figure (5.6) presents the distribution of these IR sources in the surveyed area. We determined the center of these regions based on the extent of the bright nebulosities associated to them. We will describe these IR sources in the next subsections, where we use their IRAS identification, although we also list other IDs found in the literature.

5.5.1 IRAS 20321+4112

IRAS 20321+4112 is the IR source (radio source at 4 800MHz, Wendker, Higgs & Landecker, 1991) is the IR source closest to the center of the Cygnus OB2 association. In Figure (5.10) we can see that it is divided into two structures; to the right we have a spherical glow with dark stripes on it, while to the left we can see a myriad of faint reddened stars. Other identifications in the literature are: [TGC96] 2032+4112 (radio source, Taylor et al., 1996), ECX6-27 (radio source at 4 800MHz, Wendker, Higgs & Landecker, 1991), 18P 61 (radio source at 408MHz, Wendker, Higgs & Landecker, 1991), 19P 31 (radio source at 1 420MHz, Wendker, Higgs & Landecker, 1991), WSRTGP 2032+4112 (radio source at 327 MHz, Taylor et al., 1996), 40P 37 (radio source at 408MHz, Higgs et al., 1991), MOL 128 (radio source at NH_3(1,1) and (2,2) lines, Molinaris et al., 1996), [L89b] 80.346+00.721 (HII region, Lockman, 1989) and [KC97c] G080.3+00.7 (radio source at 4.85GHz, Kuchar & Clark, 1997).

Palla et al. (1991) report the detection of this IR source in the HCO^+ maser but not in the H_2O maser survey. Odenwald (1989) classified this IR source as type "O", from "obscured field with no stellar object apparent". Parthasarathy, Jain & Bhatt (1992) suggested that the absence of ultracompact HII regions in the Cygnus OB2 region could imply that IR sources with far infrared luminosities of the order of 10^4 $L_\odot$ are younger than ultracompact HII regions. IRAS 20321+4112 has a far infrared luminosity $\simeq 10^4$ $L_\odot$ and its flux distribution matches that of massive young stellar objects.

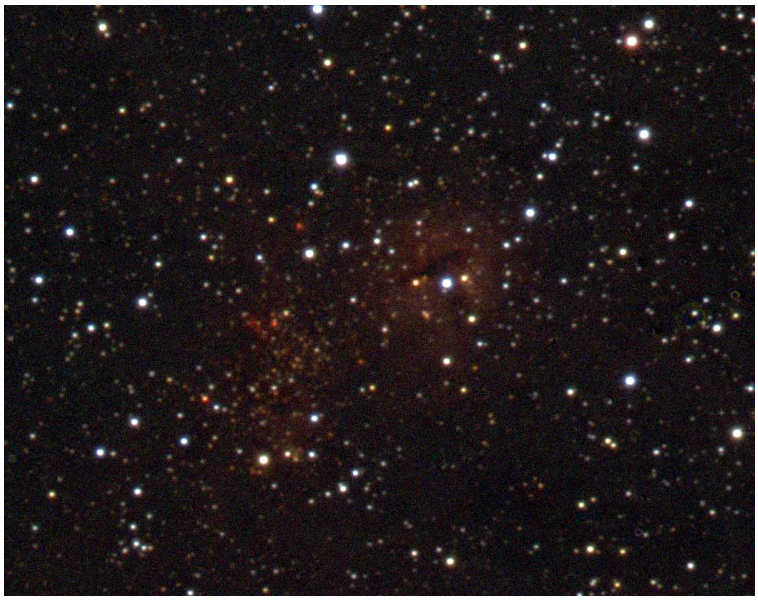

Figure 5.10: IRAS 20321+4112

Comerón & Torra (2001) determined a distance of 3.3 kpc for this region and suggest it is located behind Cygnus OB2. They also suggest that their distance is underestimated given the number of foreground stars in the studied sample. The radial velocities found by Lockman (1989) and Bronfman, Nyman & May (1996), respectively -62.4 km s^{-1} and -66.4 km s^{-1}, exclude the possibility of a physical connection between this IR source and Cygnus OB2. Following Comerón

& Torra (2001) and Bica, Bonatto & Dutra (2003) IRAS 20321+4112 lies at $\sim$ 10 kpc, at the Outer Arm. Scalise, Rodriguez & Mendonza-Torres (1989) detected a maser counterpart for this IR source and determined a kinematic distance of 6.5 kpc.

When finished, our database will be used to characterize the stars in this region. The presence of variable stars like Cepheids, RR Lyrae and Luminous Blue Variables, can help us to constrain the distance to this region. We defined its center as the coordinates RA 20:33:57 and DEC +41:22:33.

5.5.2 IRAS 20327+4120

Figure (5.11) presents an IR source with a very bright and reddened star associated with it. Patches of dark clouds can also be seen in this region. IDs in the literature include: WSRTGP 2032+4120 (radio source at 327 MHz, Taylor et al., 1996), 19P 35 (radio source at 1 420 MHz, Wendker, Higgs & Landecker, 1991) and [TGC96] 2032+4120 (radio source, Taylor et al., 1996). The detection of this region dates back to 1989 by Odenwald (1989), where it can be seen that this IR source received an Optical Type "O", which stands for "obscured field with no stellar objects apparent". The failure to detect any stellar object is understandable since the observations were done in the optical domain.

Figure 5.11: IRAS 20327+4120

Palla et al. (1991) did not detect this source in their H_2O maser survey. Parthasarathy, Jain & Bhatt (1992) suggested that this IR source could have a mass of 2×10^4 M$\odot$ and a distance of 2 kpc, based on the CO survey conducted by Congo M., (PhD thesis, 1980, Columbia University). Taylor et al. (1996) reported a ratio between the far infrared flux and the radio flux at 327 MHz ($R = S_{60\mu m}/S_{327MHz}$) of R = 7 362, which means that this source is a radio thermal emitter.

Also, the value $\log(S_{60}/S_{25}) \simeq 1.13$ is consistent with values of compact HII regions. Setia Gunawan et al. (2003) detected a source (SBHW125, table 1 of the referred work) in their radio survey at 1 400MHz, $30''$ away from the center of our IR source, with a flux density peak of 3.6 mJy, but did not detect it at 350MHz. In Fig. (5.11) the SBHW125 source coordinates correspond to the bright blue star at the top. We defined the coordinates of the center of the cluster as RA 20:34:31 and DEC +41:30:35.

The detection of IRAS 20327+4120 in radio surveys, its far infrared color and flux ratios imply that it is a site where star formation is still happening. Deeper observations would be necessary to detect, for example, outflows coming from the young stellar objects embedded in the nebula. Our photometry allied to spectral observations would help us to determine the distance and reddening for this region. The nature of IRAS 20327+4120 is still to be determined.

5.5.3 IRAS 20332+4124

Figure (5.12) presents the IR source called IRAS 20332+4124, whose coordinates correspond to the region at the right with the brightest star of the region and dark stripes. IDs associated to this object include: 19P 38 (radio source at 1 420 MHz, Wendker, Higgs & Landecker, 1991), WFS 97 (submillimetric source, Williams, Fuller & Sridharan, 2004), [HLB98] Onsala 140 (maser source, Harju et al., 1998), WSRTGP 2033+4124 (radio source, Taylor et al., 1996).

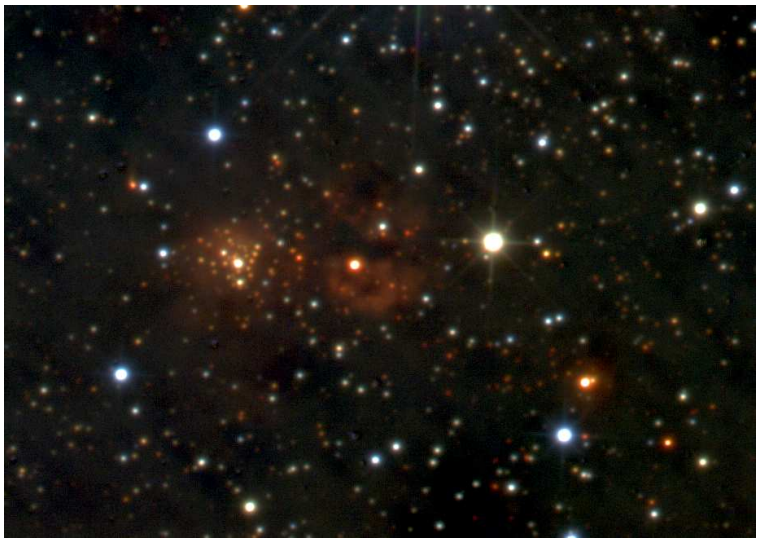

Figure 5.12: IRAS 20332+4124

IRAS 20332+4124 is similar to IRAS 20321+4112, both present two distinct regions, one with dark stripes and the other with faint red stars. We assumed the center of IRAS 20332+4124 to be RA 20:35:01 and DEC +41:34:52, based on the extent of the bright nebulosity.

Harju et al. (1998) determined a distance of 3.2 kpc for the maser source associated to this IR source. Scalise, Rodriguez & Mendonza-Torres (1989) and Palla et al. (1991) did not detect it in their H_2O maser survey and Te Lintel Hekkert (1991) also did not find it in his OH survey. Schutte et al. (1993) did not detect any methanol maser associated with this IR source. Chan, Henning & Schreyer (1996) summarized some information about this object, it has a distance of

2 kpc (Casoli et al., 1986), it is detected in CS (2-1 transition line, Bronfman, Nyman & May, 1996) and CO (1-0 transition at 110.201 MHz, Casoli et al., 1986). Sridharan et al. (2002); Beuther et al. (2002) reported a detection of this source in 1.2 mm and CS emission and a distance of 3.9 kpc. Setia Gunawan et al. (2003) detected this source in their 1 400 MHz and 350 MHz continuum survey. Edris, Fuller & Cohen (2007) reported this source as an IRAS source with thermal absorption and/or thermal emission, based on the non-detection in their OH maser observations.

The study of the population of this IR source can put constraints to its distance and age. Our survey can be used, mainly in the K band, to search for eclipsing binaries and other variable stars that can be used as distance markers.

5.5.4 IRAS 20333+4127

Figure (5.13) presents the IRAS 20333+4127 infrared source, which is permeated by a thin nebulosity. The coordinates of the center of the source are RA 20:35:10 and DEC +41:38:18.

Figure 5.13: The IRAS 20333+4127 source.

IRAS 20333+4127 is a low luminosity source, Parthasarathy, Jain & Bhatt (1992) list this source with a flux density of 3.22 Jy in 12 μm. It does not have any measurements in the other IRAS bands.

From all the IR sources in our field it is the faintest one, but as can be seen in Figure (5.13), there are many low luminosity stars associated to it. Whether these stars are located behind a denser region or belong to a loose association, remains an open question, which can be solved with our photometry and new spectroscopic observations.

5.5.5 DR18

Figure (5.14) presents the nebulosity associated with the radio source DR18. We can see a great cavity illuminated by a bright star. It is also possible to see very reddened objects embedded in, or behind, the cloud. Schneider et al. (2006) reported a velocity range of +7.7 to +10.3 km s^{-1} based on the ^{13}CO 2 - 1 emission line. This velocity range puts DR18 in the near edge of

the Cygnus OB2 region. Another characteristic that links DR18 and Cygnus OB2 is its globular shape and filaments pointing away from the OB2 region, which were probably created by the ionizing winds from the hot massive stars in the center of the OB2 association.

Other IDs found in the literature related to this object are: 18P 64, 19P 40 and ECX6-28 (radio sources respectively at 408 MHz, 1 420 MHz and 4 800 MHz, Wendker, Higgs & Landecker, 1991). We adopted the DR nomenclature (Downes & Rinehart, 1966) because it is the oldest one and furthermore because it is the most cited one for this region.

Figure 5.14: JHK composite color of DR18.

Comerón & Torra (1999) describe DR18 as an arc-shaped nebula with a central star of V = 15.6 obscured by $A_V \simeq 8$ magnitudes and spectral type around B0.5V. The arc nebula was interpreted by these authors as the interface between a molecular cloud, that is being eroded by the central star, and the resulting HII region. Usually the IRAS 20333+4102 infrared source is considered to be associated to this structure but Comerón & Torra (1999) suggest that this IRAS source is not associated to any of the structures found in their study (which uses Hα and JHK filters). They suggest that IRAS 20333+4102 could be an intermediate mass protostar embedded deeper in the molecular cloud. The winds and UV photons from the central star were not yet capable of uncovering this source. The fact that the central star is responsible for the ionization of the molecular cloud puts it at the same distance as DR18. Comerón & Torra (1999) determined a distance of 1.6 $\pm$ 0.4 kpc to the central star, which means that we can assume a distance of 1.6 kpc to the DR18 complex. At this distance we can also assume that DR18 is associated with the Cygnus OB2 region. This assumption is also supported by Schneider et al. (2006) using their ^{13}CO emission line velocities.

Because our survey covers a large area centred in the Cygnus OB2 region, we have access to a larger area around DR18, along with a better resolution and deeper photometry than Comerón & Torra (1999). We intend to use our data to study the population of this region.

Figure 5.15: Composite color image of the IRAS 20304+4059 infrared source.

5.5.6 IRAS 20304+4059

Another interesting object, close to the center of the Cygnus OB2 association, is the IRAS 20304+4059 infrared source. There is not much information about this source in the literature. Odenwald (1989) reports this source in his IRAS survey of young stellar objects towards the Cygnus X region. Parthasarathy, Jain & Bhatt (1992) report an α index of +1.48, meaning that IRAS 20304+4059 has an energy distribution broader than a blackbody, with rising flux longward of 2μm. Such index value is associated to Class I objects (protostars), in the classification scheme of Lada & Wilking (1984) and Lada (1987).

Figure (5.15) shows a composite color picture, made with our JHK images, of the IRAS 20304+4059 source. The coordinates of the IRAS source point to the red double object in the center of Fig. (5.15). A close up centered on the object can be seen in Figure (5.16). Our images have enough resolution to resolve the IRAS source into two objects, clearly visible in the center of Fig. (5.16). The high extinction of the nebulosity, where the objects are embedded, hides most of the other stars in the field.

These are very embedded objects and in order to show the relevance of our survey, we show in Figure (5.17) the same area around the IRAS source, but for different surveys. North is up and East is left in all panels. The first panel shows our K-band image, where the nebulosity responsible for the high extinction is easily seen. The second panel shows the Digital Sky Survey (red plate) image, where no object is visible. The third and fourth panels show the 2MASS J and K bands, respectively. It is possible to see that our survey goes deeper in the region, and also has a better resolution.

The coordinates and magnitudes for both objects are shown in Table (5.4). The coordinates are mean values, obtained using the coordinates for each filter and the magnitudes were taken only from the third night. We call the left star 'Source A' and the right one 'Source B'. Because we do not have any clue about the spectral type of these objects, we cannot calculate their reddening, although the J-H and H-K colors, obtained using the magnitudes listed in Table (5.4), indicate that reddening is very high. As a matter of comparison we also list in Table (5.4)

Figure 5.16: Central area close up of the previous image. The red double object is associated to the IRAS source.

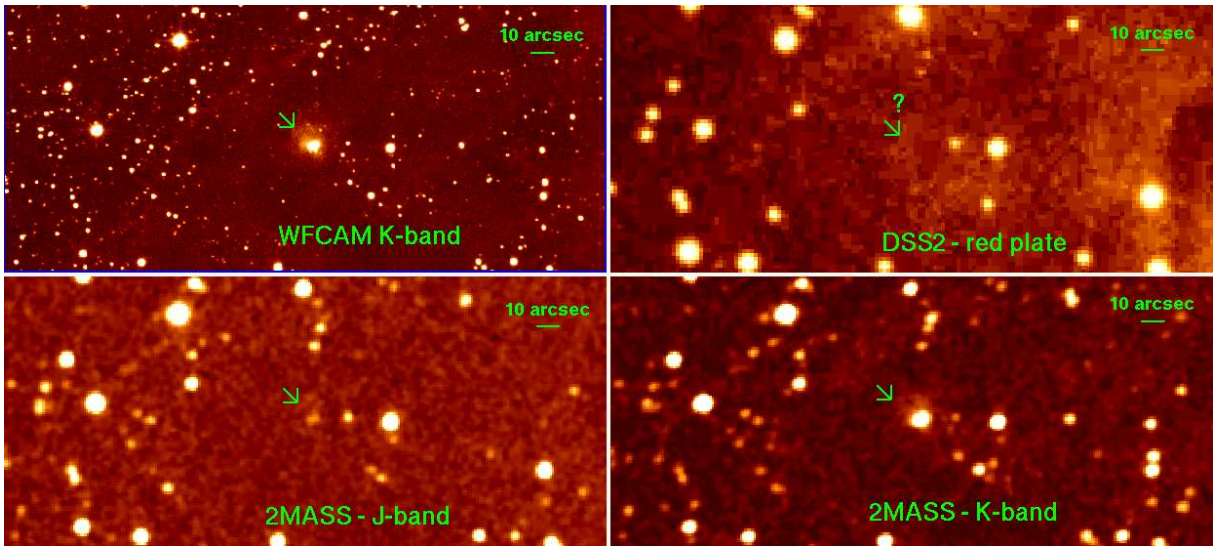

Figure 5.17: Panels showing the same area around the IRAS source for different surveys. The area of each panel is approximately the same. North is up and East is left, in all panels. The arrow indicates the position of the IRAS 20304+4059 source.

the coordinates and magnitudes of the brightest blue star close to the IRAS source. In Figure (5.16) we can see this bright blue star in the right part of the image. Its K magnitude is similar to the value found for Source A, but the J-H color is much redder for the IRAS sources. While the difference between J and K, for the comparison object, amounts to ∼0.7 magnitudes, the same difference for Sources A and B amounts to ∼4 and 5 magnitudes, respectively.

The fact that IRAS 20304+4059 is classified as a Class I source (protostar) by Parthasarathy, Jain & Bhatt (1992), along with the fact that we report it as a double source, and also the fact that it could be possibly associated to Cygnus OB2, strengthens the youth status of the Cygnus OB2 association. Spectroscopic observations of these objects are necessary to better characterize

Table 5.4: Coordinates and magnitudes of IRAS 20304+4059.

ID	α(J2000)	δ(J2000)	J	H	K
Source A	20:32:16.34	+41:09:12.60	16.708	14.295	12.706
Source B	20:32:16.17	+41:09:13.30	16.606	13.716	11.648
Comparison	20:32:13.25	+41:09:11.7	12.073	11.628	11.352

their evolutionary status.

5.6 Summary of Results

Our preliminary results indicate that star formation took place recently (a few million years ago) in Cygnus OB2, based on the existence of cometary globules, whose tails point radially away from the Cygnus OB2 center. These objects are small scale counterparts of other cometary globules found in other star forming regions. These globules must harbor massive protostars in their centers in order to sustain such sizes and resist the winds coming from the O stars of the Cygnus OB2 association.

Another important evidence of recent star formation is the detection of the embedded sources associated to the IRAS 20304+4059 infrared source. These sources are deeply embedded in nebulosity, detected in our K-band images, and spectroscopic studies are necessary to determine their true nature.

Because we are looking through a spiral arm when we observe the Cygnus X region, we were able to detect IR sources, in the same area of Cygnus OB2. Some of these IR sources have been catalogued previously using IRAS and 2MASS observations. However, only with our better resolution and sensitivity will a more detailed study be possible.

Our images of the center of the Cygnus OB2 region seems to corroborate the results found by Bica, Bonatto & Dutra (2003). However, more study is necessary to proper establish the membership of the stars.

We do not agree with Drew et al. (2008) on the position of the center of Cygnus OB2. In their work it is not clear if the center of Cygnus OB2 has coordinates RA 20:33:06 DEC +41:22:30 (J2000) or if in fact these are the coordinates of the Schulte 8 Trapezium. Either way these coordinates are wrong. The authors themselves say that the center is located NE of the Trapezium, but these coordinates place it NW of the Trapezium.

We observed only the central region of the association and still we were able to detect more than 250 000 objects, some of them background objects and many are probably foreground objects. We are still working on the final database, which will be used to analyse the variability of the stars in this region.

Chapter 6

Conclusions

Our Hα imaging survey of the Orion Nebula Cluster allowed us to discover 55 new visual binaries, among 75 binaries and 3 triples detected in the separation range of $0\farcs15$ – $1\farcs5$, corresponding to 67.5 – 675 AU. We have found a binary fraction of (8.8±1.1)% for the ONC, which corroborates previous results showing that the field binary fraction is 1.5 times larger, and that the T associations' binary fraction is 2.2 times larger than the value for the ONC. The number of stars used in the analysis is bigger than in other studies, meaning that our study has better statistics.

We detected a dramatic decrease in the number of binaries with angular separations larger than $0\farcs5$. We then used this value to distinguish between two populations, the close binaries with separation $\leq 0\farcs5$ and the wide binaries with separation $> 0\farcs5$. We detected an increase in the ratio between wide to close binaries out to a distance of $460''$ (from the center of the ONC). After this distance the ratio levels out. This effect was interpreted by us as clear observational evidence of the dynamical evolution of multiple systems as a result of passages through the potential well of the ONC.

At the beginning of this work we asked two questions: 1) Does the fact that the ONC's binary frequency is lower than the frequency of the Galactic field, have something to do with the dynamical evolution of the binary properties? and 2) Can we distinguish between the fast decay mechanism (FDM) and dynamical destruction mechanism (DDM), responsible for the dynamical evolution of the binary properties? The answer to the first question is yes. We have shown observational evidence that due to dynamical interactions between the binaries and the cluster's potential well, the wide binaries are destroyed after only a few passages through the center of the cluster. This statement also answers the second question since the dynamical interaction is explained by the DDM hypothesis.

A byproduct of our survey is the creation of a list of brown dwarf candidates in the ONC. We used the limited spectral information of the primary stars, available in the literature, to try to determine the spectral type of the secondaries, based on the flux ratios between primaries and secondaries. Although our approach is simple and may present uncertainties, it seems that as many as 50% of the binaries in our sample have companions with spectral types later than

M5 and from one-sixth to one-third may have substellar companions. Some of the companions which we classified as brown dwarf candidates were confirmed as so in observations conducted by other authors. The correct classification of these systems, as brown dwarfs or very low mass stars, is important for the study of the initial mass function of the Orion Nebula Cluster. These systems can also be used as constraints to the formation and evolution scenario of low mass stars. Low resolution infrared spectroscopy, can be used to confirm the nature of these substellar candidates.

The environment of loose T associations seems to favor the survival of the wide binary population, while the dense environment of star forming regions, like the ONC, seems to be responsible for the disruption of these wide binaries. It is reasonable to suppose that the wide binaries (mainly the late-type ones, which are less massive and hence easier to disrupt) that populate the field were born in loose T associations and therefore survived, while the single late-type field stars were born in multiple systems in dense star forming regions, which were disrupted after some close encounters in their dense environment. Thus the field population would be a mixture of single stars coming from a dense environment such as the ONC and binary stars (or multiple systems) coming from T associations such as Taurus-Auriga, Lupus, Ophiuchus, etc.

The visual binaries we have discovered in the ONC are also important for astrometric studies, which are able to determine precise stellar parameters based on the solution of the projected orbit of these systems.

Our first infrared survey, towards the Orion Nebula, was able to detect many variable stars. With the use of statistical indices we were able to separate some of the variable stars in different classes. Most important however was the capability to detect eclipsing binary candidates, which will be very important to be used as constraints to formation and evolutionary models. Stars with rotational and pulsational modulation were also detected with the use of statistical indices. The variable star population in the Orion Nebula seems to be huge. It was difficult to find constant stars in our sample, most of the objects are variable.

Our second infrared survey allowed us to study the center of the Cygnus OB2 association. We observed it during 112 nights in a time interval of 217 days. Although our final database is not complete yet we were able to use our images to detect infrared sources and cometary globules in the Cygnus OB2 region.

The cometary globules were probably created by the winds of the myriad of O-type stars in the center of the association. The discovery of such objects in the Cygnus OB2 region is strong evidence in favor of the youth of this association. Because there has to be a high concentration of mass in order to produce a cometary globule, we assume that star formation is still happening in the association.

We were able to detect four infrared sources in our surveyed area. Some of these sources were previously reported in other works, which suggest that these sources are probably not associated with Cygnus OB2. They are probably background objects situated in the Perseus Arm. The indications come from radio surveys and maser emission.

We also observed the loose association DR18, which is illuminated and eroded by a bright blue star. The IRAS source associated to DR18 seems to be a protostar still embedded in its cloud.

Another observational evidence that corroborates the youth status of Cygnus OB2 is the

double source associated to the IRAS 20304+4059 source. The double source is deeply embedded in (or hidden behind) a nebulosity that also hides many stars in the field. Spectroscopic observations, along with our photometry, are necessary to determine the nature of these objects.

Our near infrared images suggest that the center of the Cygnus OB2 region is a single structure with two separate open clusters as suggested by Bica, Bonatto & Dutra (2003).

Chapter 7

Resumo da Tese em Português

7.1 Introdução

Um dos principais ramos da astronomia atual é aquele que estuda a formação estelar. Tudo começou com a primeira observação de estrelas de baixa massa de tipo espectral tardio, na região de Taurus-Auriga, por Joy (1945). Mais tarde foi proposto por Ambartsumian (1957) que essas estrelas seriam estrelas jovens e foram denominadas estrelas T Tauri, tomando o nome do objeto que se pensou ser o protótipo da classe de estrelas do tipo solar em formação. Herbig (1960) observou as estrelas que correspoderiam às estrelas T Tauri, mas com massas intermediárias, as estrelas Ae/Be de Herbig. Desde esses trabalhos pioneiros temos visto um aumento impressionante de observações, tanto em quantidade quanto em qualidade, que dão suporte ao estabelecimento de diferentes modelos de formação, evolução e estrutura estelar. Estudamos esses sistemas estelares jovens na esperança que eles nos dêem pistas sobre a história do nosso próprio Sistema Solar. Tentamos entender como as estrelas e planetas se formam para que possamos compreender como a Terra e os outros planetas do Sistema Solar se formaram, quando o Sol tinha apenas alguns milhões de anos de idade.

Uma das coisas que aprendemos, durante o estudo de estrelas jovens, é que a maioria se forma em sistemas múltiplos. Se isso é verdade, então porque o Sol é uma estrela singular? Um sistema múltiplo pode ser destruído por diferentes mecanismos, tais como: o decaimento rápido de sistemas de poucos corpos (Sterzik & Durisen, 1998; Reipurth & Clarke, 2001; Sterzik & Durisen, 2003; Durisen, Sterzik & Pickett, 2001; Hubber & Whitworth, 2005; Goodwin & Kroupa, 2005; Umbreit et al., 2005) e a destruição dinâmica causada por múltiplas interações em ambientes densamente populados (Kroupa, 1995a,b; Kroupa et al., 2003). O primeiro mecanismo age no início da formação estelar, enquanto o núcleo da nuvem molecular termina seu colapso. Sistemas não-hierárquicos com poucos corpos (N<3) decaem em objetos singulares, binárias e sistemas múltiplos hierárquicos. O último mecanismo atua durante toda a vida do aglomerado. Ele consiste na interação de sistemas múltiplos com o poço de potencial do aglomerado e com o ambiente densamente populado que o cerca. Essa interação vai destruir os sistemas múltiplos que são fracamente ligados. Alguns modelos também prevêem que influências ambientais, tais como a temperatura do núcleo da nuvem molecular, poderiam ser importantes para definir a

fração inicial de binárias (Durisen & Sterzik, 1994; Sterzik, Durisen & Zinnecker, 2003).

As implicações da multiplicidade para o cenário de formação de planetas e também para a evolução das estrelas são ainda desconhecidas. Recentemente, Stassun et al. (2008) notificaram a descoberta de um par de "estrelas gêmeas" em um sistema binário. Cada estrela tem uma massa de $0.41\pm0.01\,M_{\odot}$, idêntica em 2%. O que faz esse par ser tão especial é o fato de que, apesar de serem similares em massa, elas têm temperaturas que diferem em $\sim$10% e luminosidades que diferem em $\sim$50%, com nível de confiança alto. Esse sistema binário, com componentes muito similares, embora não idênticas como anunciado pelos autores, é um claro exemplo da influência que a multiplicidade pode exercer durante a formação das estrelas.

Sistemas múltiplos desempenham um papel importante na astronomia. Eles são importantes para a calibração dos modelos evolutivos e não é exagero dizer que as binárias eclipsantes espectroscópicas atuam na astronomia como "balanças e réguas". Esses sistemas em particular, podem nos dar parâmetros absolutos (massa, raio, razão de teperaturas, etc) muito precisos ($\lesssim$1%), que podem ser usados como vínculos para os modelos teóricos. Apesar dos sistemas múltiplos parecerem ser muito comuns nos estágios iniciais da formação estelar, apenas 22 estrelas, na pré-sequência principal, têm parâmetros absolutos medidos através de técnicas dinâmicas (Mathieu et al., 2007; Stassun et al., 2008). Para descobrir mais binárias eclipsantes é necessário realizar levantamentos precisos e completos com uma base temporal longa.

Desde o início do estudo de estrelas jovens ficou claro que elas são objetos extremamente variáveis. Na verdade, variabilidade fotométrica era um dos critérios usados para classificá-las. Estrelas jovens apresentam variabilidade fotométrica e espectroscópica em todos os comprimentos de onda, desde o rádio até os raios-x. A maior parte da variabilidade é causada, de formas distintas, pelo material circunstelar. Esse material pode causar extinção variável quando cruza a nossa linha de visada em direção à estrela, causando quedas no brilho. O processo de acresção, através do qual a estrela aumenta sua massa, pode ainda estar ativo, causando variações no brilho da estrela. Em estrelas T Tauri, a zona de convecção cria campos magnéticos fortes o suficiente para produzir manchas frias de larga escala em sua fotosfera, aliado com a rotação da estrela isso produz modulações periódicas na curva de luz da estrela. 'Flares' em estrelas jovens, similares aos 'flares' solares, podem produzir variabilidade fotométrica irregular. Os processos de acresção e ejeção de matéria podem também mudar o perfil de linha de várias espécies atômicas presentes na fotosfera da estrela, dando origem à variabilidade espectroscópica em estrelas jovens. Pulsação também foi observada em estrelas jovens (e.g. Kurtz & Marang, 1995) situadas na faixa de instabilidade do diagrama HR.

Dito tudo isso, nos deparamos com dois importantes tópicos: estrelas jovens múltiplas e estrelas jovens variáveis. Ambos são importantes e estão diretamente associados, já que estrelas em sistemas múltiplos podem ser (e, na maior parte do tempo, são) variáveis. Só teremos um quadro claro do cenário da formação estelar se estudarmos sistemas individuais em detalhe. Alta precisão na determinação de parâmetros absolutos, de estrelas individuais, é essencial se queremos construir modelos que realmente reproduzem os processos que ocorrem na natureza. Mas para selecionar bons candidatos para estudo, primeiro precisamos descobri-los. Essa é a importância de levantamentos de larga escala. Uma vez que os astrônomos estão presos à Terra e portanto não têm acesso ao seus experimentos, é necessário mapear todo o céu em busca do "bom experimento". Existem muitas dificuldades em se realizar levantamentos de larga escala, por exemplo, disponibilidade de tempo em telescópios para fazer observações em áreas específicas do céu, instrumentação correta, capacidade de armazenamento de grandes quantidades de dados,

recursos computacionais para processar toda a informação coletada, recursos humanos para analisar os dados, etc. Muitos levantamentos foram feitos recentemente com a intenção de mapear todo o céu, em diferentes comprimentos de onda, tais como: o Two Micron All Sky Survey (2MASS, Skrutskie et al., 2006) nas bandas JHK do infravermelho próximo, o Sloan Digital Sky Survey (SDSS, Fukugita et al., 1996) nas bandas óticas Sloan (u', g', r', i', z'), o All Sky Automated Survey (ASAS, Pojmanski, 1997) nas bandas óticas V e I, o Variable Young Stars Optical Survey (VYSOS), que quando estiver em funcionamento vai monitorar os céus do norte e do sul nas bandas Sloan, o UKIRT Infrared Deep Sky Survey (UKIDSS) considerado o sucessor do 2MASS, apenas para citar alguns deles. Nossa intenção é diferente, não queremos monitorar todo o céu, queremos focar nossa atenção em regiões específicas de formação estelar, com o intuito de construir uma base de dados completa, cobrindo longos períodos, usualmente centenas de dias. Em vez de olhar para o céu todo, vamos olhar para regiões específicas por um longo intervalo de tempo.

Na nossa tentativa de melhor entender as estrelas jovens múltiplas, notificamos aqui a realização de um imageamento usando a Advanced Camera for Surveys, a bordo do telescópio espacial Hubble, da Nebulosa de Órion. O principal objetivo desse levantamento é descobrir novas binárias visuais em uma ampla região ao redor do Aglomerado da Nebulosa de Órion. Estudos anteriores mostraram que a frequência de binárias nesse aglomerado é menor do que a frequência de binárias do campo Galáctico. Esse fato tem alguma relação com a evolução dinâmica do aglomerado? Podemos distinguir entre os dois mecanismos responsáveis pela evolução dinâmica das propriedades das binárias? Tentamos responder essas questões no Capítulo 2.

Nossa segunda incursão no domínio da formação estelar está relacionada com dois levantamentos de larga escala no infravermelho, de duas regiões de formação estelar. Nosso principal objetivo é descobrir a população de estrelas jovens variáveis da Nebulosa de Órion e da jovem associação de estrelas OB Cygnus OB2. Para essa tarefa usamos a Wide Field Camera do United Kingdom Infrared Telescope, o instrumento infravermelho destinado a levantamentos mais eficiente no mundo atualmente, instalado no alto do Observatório Mauna Kea. Apresentamos no Capítulo 3 algumas técnicas estatísticas que podem ser usadas para separar a população de estrelas variáveis nesses campos. Curvas de luz do ASAS foram usadas como testes para melhor entender o comportamento desses índices estatísticos.

No Capítulo 4 apresentamos as observações, procedimentos e resultados do levantamento realizado na Nebulosa de Órion. Construímos uma base de dados usando 98 noites, das 101 noites observadas cobrindo 178 dias, que é até esse momento o levantamento infravermelho mais longo realizado para a Nebulosa de Órion. Muitos objetos variáveis interessantes foram encontrados após a aplicação dos índices estatísticos.

Cygnus OB2 é analisada no Capítulo 5. É uma associação OB gigante, que chegou a ser considerado um aglomerado globular jovem, dado o grande número de estrelas do tipo O nessa região ($\sim$100 estrelas). Cygnus OB2 está situada na região de formação estelar Cygnus X, atrás da região conhecida como "Great Cygnus Rift". Quando olhamos nessa direção estamos olhando através do Braço Espiral Local e do Braço Espiral de Perseu e portanto podemos ver várias regiões de formação estelar projetadas na mesma área do céu. Uma análse mais cuidadosa da sua população de estrelas de massa baixa e intermediária, é necessária para se colocar limites na sua massa total e extensão. Observamos o centro dessa associação durante 112 noites, cobrindo um intervalo de 217 dias, mas dada a enorme quantidade de dados, ainda

não foi possível terminar a base de dados. Entretanto, quatro noites foram usadas para construir um catálogo preliminar, que foi usado para estudar as propriedades desse interessante região de formação estelar. Esse é o levantamento infravermelho mais rico já feito para essa região e dada a resolução angular obtida, seremos capazes de dobrar o número de objetos associados a ela.

7.2 Binárias Visuais no Aglomerado da Nebulosa de Órion

7.2.1 Introdução

O Aglomerado da Nebulosa de Órion é responsável pela ionização da região HII conhecida como Nebulosa de Órion (M42+M43 = NGC 1976), uma das mais estudadas regiões do céu. Ele chama tanta atenção porque é a região de formação estelar gigante mais próxima ao Sol (situado a $\sim$450 pc). Suas estrelas mais massivas, conhecidas como estrelas do Trapézio, estão localizadas em seu centro. Pensava-se que elas eram uma entidade distinta (e.g. Herbig & Terndrup, 1986) mas tem se sugerido que elas são na verdade o núcleo desse aglomerado (Hillenbrand & Hartmann, 1998).

O Aglomerado da Nebulosa de Órion não é somente a região de formação estelar de alta massa mais próxima, mas também é muito jovem, com uma idade de $\sim$1 milhão de anos. Sua juventude é sustentada por:

- estrelas localizadas acima da Sequência Principal de Idade Zero (Herbig & Terndrup, 1986; Prosser et al., 1994);
- variabilidade fotométrica de mais de 50% das suas estrelas (Jones & Walker, 1988; Choi & Herbst, 1996);
- existência de linhas de emissão no ótico;
- alta polarização;
- excesso no infravermelho;
- 'proplyds' apontando na direção de θ^1 Ori C (a estrela mais massiva das estrelas do Trapézio).

Um resultado intrigante, que vem do estudo da formação e evolução de sistemas binários, é que binárias são mais comuns em associações T (associações com estrelas de baixa massa e que são fracamente ligadas) do que no campo (e.g. Reipurth & Zinnecker, 1993; Simon et al., 1995; Duchêne, 1999; Ratzka, Köhler & Leinert, 2005). Um resultado ainda mais intrigante é que o Aglomerado da Nebulosa de Órion tem uma frequência de binárias menor do que associações T e do que o campo (e.g. Prosser et al., 1994; Padgett, Strom & Ghez, 1997; Petr et al., 1998; Simon, Close & Beck, 1999; Köhler et al., 2006).

O estudo das propriedades dos sistemas binários é marcado pelo trabalho detalhado de Duquennoy & Mayor (1991, daqui em diante DM91). As propriedades da população de binárias do campo serve como referência para o trabalho com populações mais jovens. Mas podemos confiar na população de binárias do campo? Como ela é formada? Ela vem de uma mistura de populações de outros aglomerados?

Atualmente existem dois modelos principais para a evolução das propriedades das binárias: 1) decaimento dinâmico rápido de sistemas de poucos corpos (e.g. Reipurth & Clarke, 2001; Sterzik & Durisen, 1998, 2003; Durisen, Sterzik & Pickett, 2001; Hubber & Whitworth, 2005;

Goodwin & Kroupa, 2005; Umbreit et al., 2005) e 2) destruição dinâmica através de múltiplas interações em um ambiente densamente populado (e.g. Kroupa, 1995a,b; Kroupa et al., 2003). O primeiro atua nos estágios iniciais da formação estelar, enquanto o segundo mecanismo precisa de mais tempo para agir e o faz por mais tempo.

Até esse momento, as estatísticas sobre a frequência de binárias no Aglomerado da Nebulosa de Órion eram pobres e concentradas em regiões ao redor das estrelas do Trapézio. Mostramos aqui, usando números significativos, que realmente esse aglomerado tem uma fração de binárias menor do que as associações T e do que o campo.

7.2.2 Resultados

1. Um total de 75 sistemas binários e 3 sistemas triplos foram detectados, dos quais 55 são novas descobertas;
2. Dentro do nosso intervalo limitado de separação angular, $0\farcs15$ – $1\farcs5$, que corresponde a 67.5 – 675 UA, encontramos uma fração de binárias de (8.8±1.1)% após a correção de contaminção por pares falsos;
3. A fração de binárias do tipo solar no campo, no mesmo intervalo, é 1.5 vezes maior e para associações T é 2.2 vezes maior do que no Aglomerado da Nebulosa de Órion. O que confirma, com dados estatisticamente significantes, resultados anteriores de que esse aglomerado é deficiente em binárias;
4. A função distribuição de separação para as binárias jovens nesse aglomerado apresenta uma diminuição dramática em binárias para separações angulares maiores que $0\farcs5$, correspondendo a 225 UA;
5. A razão entre as distribuições cumulativas de binárias com grande separação e binárias cerradas aumenta até uma distância de $460''$ do centro do aglomerado, depois da qual a razão fica constante. Interpretamos esse resultado como uma evidência observacional clara da evolução dinâmica da população de binárias, como resultado de passagens através do poço de potencial do aglomerado. Esses resultados são consistentes com uma idade de 1 milhão de anos para o Aglomerado da Nebulosa de Órion;
6. Parece que, ao menos em parte, a deficiência de binárias em Órion, quando comparado com a população do campo, pode ser entendida em termos da destruição das binárias com grande separação combinado com um efeito secundário da evolução orbital de binárias em direção a separações menores, que não podem ser observadas através de imageamentos diretos;
7. Informação espectral limitada sobre as estrelas primárias da nossa amostra indicam que elas são estrelas T Tauri de baixa massa, com exceção de uma estrela que é uma Ae/Be de Herbig. Supondo que a maioria das binárias não são afetadas por extinção diferencial, encontramos que possivelmente 50% das binárias têm companheiras com tipo espectral mais frio que M5 e de um sexto até um terço das binárias podem ter companheiras subestelares (anãs marrons). Esse grande número de companheiras subestelares é de interesse para as teorias sobre formação de anãs marrons.

O ambiente mais calmo das associações de estrelas T Tauri parece favorecer a sobrevivência de binárias com grande separação, enquanto ambientes densos como Órion parecem ser responsáveis pela destruição de parte dessas binárias. É razoável supor que binárias separadas (principalmente

de tipo espectral frio) que populam o campo estelar, nasceram em associações pouco massivas e portanto sobreviveram, enquanto as estrelas singulares do campo nasceram em sistemas múltiplos em regiões densas, que foram destruídas após alguns encontros nesse ambiente denso. A população do campo seria uma mistura de estrelas singulares vindas dessas regiões mais densas, como Órion, e sistemas binários (ou múltiplos) vindos de associações como Taurus-Auriga, Lupus, Ophiuchus, etc.

A descoberta de binárias visuais em regiões de formação estelar, como Órion, é muito importante. Apesar de estar a uma distância de ∼450 pc, observações astrométricas dessas binárias, com a Advanced Camera for Surveys, por exemplo, podem ser usadas para determinar órbitas projetadas e dessa forma obter parâmetros estelares precisos. Alguns estudos nesse sentido foram feitos em outra regiões (e.g. Chauvin et al., 2005; Neuhäuser et al., 2008).

7.3 Índices Estatísticos

Variabilidade é uma característica inerente das estrelas. Podemos dizer que todas as estrelas são variáveis, em diferentes estágios de suas vidas, com diferentes amplitudes e escalas de tempo. Durante sua vida, uma estrela viaja ao longo de diferentes caminhos em um diagrama HR e portanto apresenta diferentes características. Entretanto, é impossível observar uma estrela ao longo de sua evolução, desde sua nuvem natal, através da sequência principal, em direção a seus momentos finais como uma anã branca, uma estrela de neutrôns ou um buraco negro. O que podemos fazer é estudar diferentes estrelas, em diferentes estágios evolutivos e tentar colocar esse quebra-cabeça junto em um quadro coerente.

Chamaremos de estrelas variáveis aquelas que apresentam variabilidade no brilho em uma escala de tempo que podemos medir, seja em segundos, dias, anos, ou décadas, com amplitudes que podemos medir usando CCDs, fotômetros ou até mesmo placas fotográficas. A escala de tempo, a forma da curva de luz e a amplitude da variação de brilho podem ser usadas para classificar as estrelas variáveis. Tipo espectral, classe de luminosidade e composição química também são parâmetros importantes que nos ajudam a classificar as estrelas de acordo com a origem das variações.

Estrelas variáveis podem ser divididas em dois grandes grupos: variáveis intrínsecas e extrínsecas. Variáveis intrínsecas são aquelas que variam devido a um processo físico na própria estrela, enquanto variáveis extrínsecas são aquelas que variam devido a um processo externo à estrela.

Exemplos de variáveis intrínsecas são as estrelas pulsantes e as estrelas eruptivas (ou explosivas). Variáveis extrínsecas são, por exemplo, sistemas eclipsantes e variações ocasionadas por rotação. Deve ficar claro que um tipo de variabilidade não exclui o outro. Podemos ter, por exemplo, uma estrela pré-sequência principal eclipsante em que uma das componentes (ou até mesmo ambas) apresenta pulsações.

A fim de distinguir entre diversos tipos de variabilidade é necessário usar alguns índices estatísticos. Alguns podem ser aplicados diretamente à curva de luz de uma estrelas, outros são ideais se aplicados a curvas de resíduos ou mesmo a curvas de valores médios. Nesse trabalho usamos os seguintes índices:

1. magnitude média;
2. desvio padrão;

3. desvio geométrico;
4. desvio absoluto médio;
5. valor absoluto da amplitude máxima de variação;
6. desvio máximo da magnitude média;
7. estatística-R;
8. obliquidade;
9. curtose.

Para testar esses índices estatísticos usamos curvas de luz reais, obtidas do banco de dados do All Sky Automated Survey[1]. Utilizamos curvas de luz dos seguintes tipos de estrelas variáveis: α^2 Canum Venaticorum, Ceféidas, δ-Scuti, binárias eclipsantes, RR-Lirae e variáveis de tipo desconhecido.

Além de aplicar os índices estatísticos descritos acima, calculamos também como esses índices variam ao longo das observações. Isso serve para simular o comportamento dos índices à medida que mais medidas são adicionadas a um banco de dados. Isso será de muita importância para projetos que visam monitorar regiões de formação estelar durante um longo intervalo de tempo. Dessa forma, construímos curvas para esses índices e os nomeamos índices estatísticos dinâmicos.

O uso dos índices estatísticos finais e dinâmicos nos permitiu concluir que é possível usar um conjunto deles para separar diferentes tipos de estrelas variáveis dentro de um grande conjunto de dados. Isso será de vital importância para projetos que monitoram grandes áreas do céu, como fizemos para a Nebulosa de Órion e para Cygnus OB2.

As estrelas binárias eclipsantes podem ser separadas dos demais objetos se observarmos que as curvas dos índices dinâmicos são segmentadas, devido às repentinas mudaças de brilho.

Estrelas do tipo Cefeida, δ-Scuti e RR-Lira, que apresentam pulsações, também apresentam curvas para a obliquidade e curtose (calculadas a partir das magnitudes médias) que são bem características. Estrelas do tipo α^2 Canis Venaticorum, que são estrelas que apresentam variabilidade devido à rotação, apresentam comportamento contrário ao das estrelas pulsantes.

De posse dessas informações, podemos aplicar nossos índices estatísticos à nossa base de dados em Órion e em Cygnus OB2.

7.4 Levantamento Fotométrico da Nebulosa de Órion

7.4.1 Introdução

Desde o início do estudo de estrelas jovens (e.g. Joy, 1945; Herbig, 1960, 1962) a variabilidade fotométrica serviu como uma das características que definiam as estrelas na pré-sequência principal. Variabilidade foi primeiramente detectada e estudada na região de comprimentos de onda visíveis, mas logo ficou claro que as estrelas jovens são variáveis em todos os comprimentos de onda. Muito estudos fotométricos, em diferentes comprimentos de onda, já foram feitos na Nebulosa de Órion (e.g. Rebull, 2001; Carpenter, Hillenbrand & Skrutskie, 2001; Getman et al., 2005; Flaccomio et al., 2005; Stassun et al., 1999, 2006).

Nosso propósito é observar a Nebulosa de Órion e seus arredores, na região do infravermelho (JHK), durante um longo intervalo de tempo, para detectar estrelas variáveis em escalas de

[1] http://www.astrouw.edu.pl/asas/

tempo de alguns dias até alguns meses. Um dos produtos desse levantamento é a detecção de binárias eclipsantes, cujos parâmetros estelares são muito importantes para se colocar vínculos nos modelos de formação e evolução estelar.

Para realizar esse levantamento utilizamos a Wide Field Camera (WFCAM), instalada no United Kingdom Infrared Telescope. Infelizmente, devido a problemas na subtração do céu, não poderemos usar os dados reduzidos pelo pipeline final. Usaremos entretanto os dados reduzidos pelo pipeline do telescópio, o que dará aos nossos resultados um status de "resultados preliminares".

Foram observadas 101 noites, mas apenas 98 foram reduzidas pelo pipeline. Desenvolvemos rotinas para lidar com diversos problemas que não foram resolvidos durante a redução do pipeline e para organizar as observações. Conseguimos estabelecer um banco de dados com as 98 noites observadas.

7.4.2 Resultados

Após aplicarmos os índices estatísticos à nossa amostra de estrelas, que consiste em aproximadamente 8 000 estrelas, conseguimos descobrir novas estrelas binárias eclipsantes, estrelas com pulsações e com curvas de luz criadas devido à combinação de manchas estelares e rotação. Nossos índices estatísticos se mostraram úteis para a separação de diferentes tipos de estrelas variáveis.

7.5 Levantamento Fotométrico em Cygnus OB2

7.5.1 Introdução

Umas das regiões de formação estelar mais ricas da Galáxia está na direção da constelação do Cisne e é conhecida como Cygnus X. Essa é também uma das regiões mais brilhantes do céu em todos os comprimentos de onda. Quando olhamos nessa direção estamos olhando através do Braço Espiral Local e do Braço de Perseu, de forma que somos iludidos por diferentes regiões de formação estelar sobrepostas na mesma região do céu. Algumas dessas regiões estão localizadas a algumas centenas de parsecs, enquanto outras estão a alguns milhares de parsecs de distância. Uma das regiões mais importantes nessa área é a jovem associação OB chamada Cygnus OB2.

Essa região foi descoberta por Münch & Morgan (1953), que chamaram a atenção para uma "possível associação de estrelas azuis gigantes". Muitos estudos se seguiram a esse trabalho, com o intuito de melhor definir a população de estrelas massivas dessa associação. Diversos estudos apontam para uma distância de 1.7 kpc até Cygnus OB2 e também para um alta extinção (5 – 20 magnitudes). A idade dessa associação ainda é incerta, mas estima-se que esteja entre 1 e 3 milhões de anos.

Através de observações feitas com o 2MASS, Knödlseder (2000) sugeriu que Cygnus OB2 fosse considerado um aglomerado globular jovem, dado o alto número de estrelas do tipo OB ($\sim$2600$\pm$400 estrelas, dentre as quais $\sim$120$\pm$20 são estrelas O), sua geometria esférica e sua juventude. Mais tarde, Knödlseder et al. (2002) reclassificou Cygnus OB2 como um super-aglomerado. A população de estrelas de alta massa de Cygnus OB2 contém algumas das estrelas mais brilhantes da nossa Galáxia e o estudo desses objetos é muito importante para aumentar nosso conhecimento sobre essa parte da função inicial de massa.

Observamos Cygnus OB2 durante 112 noites, cobrindo um intervalo de 217 dias. Ainda não foi possível terminar a catalogação de todos os objetos e todas as noites observadas, devido ao enorme volume de informação.

7.5.2 Resultados

Utilizando nossas imagens na banda K descobrimos 6 glóbulos cometários na região de Cygnus OB2. Todos têm suas caudas apontando radialmente opostas ao centro da associação. Esses glóbulos, se associados à Cygnus OB2, são mais uma prova da juventude dessa associação. Muitos desses glóbulos têm estrelas bem avermelhadas em suas cabeças, prova de que a formação estelar ainda está acontecendo nessa região.

Nossas imagens também nos permitiram observar 4 fontes infravermelhas, que graças a outros estudos, parecem estar localizadas a distâncias maiores do que Cygnus OB2. O estudo da população estelar dessas regiões é muito importante para melhorar nosso entendimento sobre suas idades e melhorar suas determinações de distância.

Determinamos a natureza múltipla da fonte infravermelha IRAS 20304+4059, que tem características de um objeto protoestelar.

7.6 Conclusões

Nosso imageamento em Hα do Aglomerado da Nebulosa de Órion nos permitiu descobrir 55 novas binárias visuais, dentre 75 binárias e 3 sistemas triplos no intervalo de separação $0\farcs15$ – $1\farcs5$. Isso nos levou a obter uma fração de binárias de (8.8±1.1)% para esse aglomerado, corroborando resultados anteriores que indicam que a fração de binárias do campo é 1.5 vezes maior e das associações T é cerca de 2.2 vezes maior que a do Aglomerado da Nebulosa de Órion. O número de estrelas usadas nessa análise é maior do que em outros estudos, o que implica que nossa estatística é mais significativa.

Detectamos uma diminuição dramática no número de binárias com separação angular maior que $0\farcs5$. Usamos esse valor para separar nossa amostra em dois grupos: binárias cerradas com separação $\leq 0\farcs5$ e binárias com separação $>0\farcs5$. Detectamos um aumento na razão entre binárias com grande separação e cerradas até uma distância de $460''$ (do centro do aglomerado). Após essa distância essa razão se nivela. Interpretamos esse efeito como uma clara evidência observacional da evolução dinâmica dos sistemas múltiplos, como um resultado de passagens através do poço de potencial do Aglomerado da Nebulosa de Órion.

No início desse trabalho fizemos duas perguntas: 1) O fato da frequência de binárias do Aglomerado da Nebulosa de Órion ser menor que a frequência do campo galático, está relacionado com a evolução dinâmica das propriedades das binárias? e 2) Podemos distinguir entre o mecanismo de decaimento rápido e o mecanismo de destruição dinâmica, responsáveis pela evolução dinâmica das propriedades das binárias? A resposta para a primeira pergunta é: sim. Nós mostramos evidências observacionais que, graças a interações dinâmicas entre as binárias e o poço de potencial do aglomerado, as binárias com grandes separações são destruídas após algumas passagens pelo centro do aglomerado. Isso também responde a segunda pergunta, uma vez que a interação dinâmica é explicada pela hipótese do mecanismo de destruição dinâmica.

Um subproduto do nosso imageamento é a criação de uma lista de candidatas a anãs marrons

no Aglomerado da Nebulosa de Órion. Usamos a informção espectral disponível sobre as estrelas primárias para tentar determinar o tipo espectral das secundárias. Nos baseamos na razão de fluxos entre as primárias e secundárias. Apesar de nossa tentativa ser simples e apresentar incertezas, parece que 50% das binárias em nossa amostra têm companheiras com tipo espectral mais frio que M5 e entre um sexto e um terço podem ter companheiras subestelares. Algumas dessas companheiras, que classificamos como anãs marrons, foram confirmadas como tais por observações feitas por outros autores. A classificação correta desses sistemas, como anãs marrons ou estrelas com massa muito baixa, é importante para o estudo da função de massa inicial do Aglomerado da Nebulosa de Órion. Esses sistemas podem também ser usados como vínculos para os modelos de formação e evolução de estrelas de baixa massa. Espectroscopia de baixa resolução no infravermelho pode ser usada para confirmar a natureza dessas candidatas subestelares.

O ambiente das associações T parece favorecer a sobrevivência de binárias com grandes separações, enquanto ambientes mais densos e populosos, como Órion, parecem ser responsáveis pela destruição dessas binárias. É razoável supor que essas binárias com grandes separações (principalmente as de tipo espectral mais tardio, que são menos massivas e portanto mais fáceis de serem destruídas) que populam o campo, nasceram em associações T e portanto sobreviveram, enquanto as estrelas singulares, do mesmo tipo espectral, nasceram em regiões mais densas e foram destruídas após alguns encontros nesse ambiente denso. Logo, a população do campo seria uma mistura de estrelas singulares vindas de ambientes densos, tais como Órion, e binárias (ou sistemas múltiplos) vindas de associações T, como Taurus-Auriga, Lupus, Ophiuchus, etc.

As binárias que descobrimos no Aglomerado da Nebulosa de Órion são também importantes para estudos astrométricos, que são capazes de fornecer parâmetros estelares precisos, baseados na solução das órbitas projetadas desses sistemas.

Nosso primeiro levantamento infravermelho, na direção da Nebulosa de Órion, foi capaz de detectar muitas estrelas variáveis. Através do uso de índices estatísticos fomos capazes de separar algumas estrelas variáveis em diferentes classes. O mais importante, contudo, foi a capacidade de detectar candidatas a binárias eclipsantes, que são muito importantes quando usadas como vínculos para os modelos de formação e evolução estelar. Estrelas com pulsações e com modulação causada por rotação também foram detectadas com os índices estatísticos. A população de estrelas variáveis da Nebulosa de Órion parece ser grande. Foi difícil encontrar estrelas constantes em nossa amostra.

Nosso segundo levantamento infravermelho nos permitiu estudar o centro da associação Cygnus OB2. Observamos essa associação durante 112 noites em um intervalo de 217 dias. Apesar de nosso banco de dados não ter sido finalizado, fomos capazes de usar nossas imagens para detectar fontes infravermelhas e glóbulos cometários na região de Cygnus OB2.

Os glóbulos cometários foram provavelmente criados pelos ventos da miríade de estrelas do tipo O que se encontram no centro dessa associação. A descoberta de tais objetos na região de Cygnus OB2 é uma forte evidência em favor da juventude dessa associação. Devido ao fato de que é necessária uma alta concentração de massa para produzir um glóbulo cometário, supomos que a formação de estrelas pode ainda estar acontecendo nessas regiões.

Fomos capazes de detectar quatro fontes infravermelhas na região de Cygnus OB2. Algumas dessas fontes já foram observadas por estudos anteriores, os quais sugerem que essas fontes não estão associadas à Cygnus OB2. Elas são provavelmente objetos localizados no Braço de Perseu, segundo indicações vindas de levantamentos em rádio e emissão maser.

Também observamos a fonte de rádio DR18, que consiste em uma nebulosidade iluminada e erodida por uma estrela azul bem brilhante. Uma distância de 1.6 kpc foi determinada para essa estrela por Comerón & Torra (1999) e com isso ela foi associada com Cygnus OB2. A fonte IRAS associada a essa fonte de rádio pode ser uma protoestrela ainda embebida na nuvem.

Outra evidência observacional que corrobora o status de juventude de Cygnus OB2 é a fonte dupla associada a fonte IRAS 20304+4059. Essa fonte dupla está embebida (ou escondida) em uma nebulosidade que também esconde muitas estrelas no mesmo campo. Observações espectroscópicas, em conjunto com nossa fotometria, são necessárias para determinar a verdadeira natureza desses objetos.

Nossas imagens infravermelhas sugerem que o centro de Cygnus OB2 é uma estrutura única e não dois aglomerados abertos distintos, como suposto por Bica, Bonatto & Dutra (2003).

References

Albacete Colombo, J.F., Flaccomio, E., Micela, G., Sciortino, S., & Damiani, F., 2007, A&A , 464, 211

Ambartsumian, V. A., 1957, IAUS, 3, 177

Audard, M., Güdel, M., Skinner, S. L., Briggs, K. R., Walter, F. M., Stringfellow, G., Hamilton, R. T., & Guinan, E. F., 2005, ApJ , 635, L81

Bally, J., Licht, d., Smith, N., & Walawender, J., 2006, AJ, 131, 473

Bally, J., & Reipurth, B., 2001, ApJ , 546, 299

Baraffe, I., Chabrier, G., Allard, F., & Hauschildt, P. H., 1998, A&A , 337, 403

Bate, M. R., Bonnell, I. A., & Bromm, V., 2002, MNRAS , 336, 705

Baptista R., Steiner J.E., 1993, A&A , 277, 331

Bessell, M., & Brett, J. M., 1988, PASP , 100, 1134

Beuther, H., Schilke, P., Menten, K. M., Motte, F., Sridharan, T. K., & Wyrowski, F., 2002, ApJ , 566, 945

Bica, E., Bonatto, Ch., & Dutra, C. M., 2003, A&A , 405, 991

Blanco, V. M., 1963, ApJ , 137, 513

Bodenheimer, P., Burket, A., Klein, R. I., & Boss, A. P., 2000, Protostars and Planets IV, p. 675

Brandeker, A., Jayawardhana, R., Khavari, P., Haisch, K. E., & Mardones, D., 2006, ApJ , 652, 1572

Bronfman, L., Nyman, L.-Å, & May, J., 1996, A&AS , 115, 81

Bruch A., 1999, AJ, 117, 3031

Carpenter, J. M., Hillenbrand, L. A., & Skrutskie, M. F., 2001, AJ, 121, 3160

Cash, W., Charles, P., Bowyer, S., Walter, F., Garmire, G., & Riegler, G., 1980, ApJ , 238, L71

Casoli, F., Dupraz, C., Gerin M., Combes, F., Boulanger, F., 1986, A&A , 169, 281

Chabrier, G., Baraffe, I., Allard, F., & Hauschildt, P. H., 2000, ApJ , 542, 464

Chan, S. J., Henning, T., & Schreyer, K., 1996, A&AS , 115, 285

Chauvin, G., Lagrange, A.-M., Lacombe, F., Dumas, C., Mouillet, D., Zuckerman, B., et al., 2005, A&A , 430, 1027

Choi, P., & Herbst, W., 1996, AJ, 111, 283

Comerón, F., Pasquali, A., Rodighiero, G., Stanishev,V., De Filippis, E., López Martí, B., Gálvez Ortiz, M.C., Stankov, A., & Gredel, R., 2002, A&A , 389, 874

Comerón, F. & Torra, J., 1994, ApJ , 423, 652

Comerón, F. & Torra, J., 1999, A&A , 349, 605

Comerón, F. & Torra, J., 2001, A&A , 375, 539

Conti, P.S. & Blum, R.D., 2002, ApJ , 564, 827

Correia, S., Zinnecker, H., Ratzka, Th., & Sterzik, M. F., 2006, A&A , 459, 909

Dahn, C. C., Harris, H.C., Vrba, F.J., Guetter, H.H., Canzian,B., Henden, A.A., Levine, S.E., Luginbuhl, C.B., Monet, D.G., Pier, J.R., Stone, R.C., & Walker, R.L., 2002, AJ, 124, 1170
De Becker, M., Rauw, G., Sana, H., Pollock, A.M.T., Pittard, J.M., Blomme, R., Stevens, I.R., & Van Loo, S., 2006, MNRAS , 371, 1280
De Becker, M., Rauw, Pittard, J.M., Sana, H., Stevens, I.R., & Romero, G.E., 2007, A&A , 472, 905
Downes, D., & Rinehart, R., 1966, ApJ , 144, 937
Drew, J.E., Greimel, R., Irwin, M.J., & Sale, S.E., 2008, MNRAS , 386, 1761
Duchêne, G., 1999, A&A , 341, 547
Duchêne, G., Bouvier, J., Bontemps, S., André, P., & Motte, F., 2004, A&A , 427, 651
Duncan, D. K., 1993, ApJ , 406, 172
Duquennoy, A., & Mayor, M., 1991, A&A , 248, 485
Durisen, R. H., & Sterzik, M .F., 1994, A&A , 286, 84
Durisen, R. H., Sterzik, M. F., & Pickett, B. K., 2001, A&A , 371, 952
Edris, K. A., Fuller, G. A., & Cohen, R. J., 2007, A&A , 465, 865
Edwards, S., et al., achar resto, 1993, AJ, 106, 372
Figer, D.F., Kim, S.S., Morris, M., Serabyn, E., Rich, R.M., McLean, I.S., 1999, ApJ , 525, 750
Flaccomio, E., Micela, G., Sciortino, S., Feigelson, E. D., Herbst, W., Favata, F., Harnden, F. R., Jr., & Vrtilek, S. D., 2005, ApJS , 160, 450
Fukugita, M., Ichikawa, T., Gunn, J. E., Doi, M., Shimasaku, K., Schneider, & D. P., 1996, AJ, 111, 1748
Getman, K. V., Feigelson, E. D., Grosso, N., McCaughrean, M. J., Micela, G., Broos, P., Garmire, G., & Townsley, L., 2005, ApJS , 160, 353
Goodwin, S. P., & Kroupa, P., 2005, A&A , 439, 565
Goodwin, S. P., Kroupa, P., Goodman, A., & Burkert, A., 2007, Protostars and Planets V, p. 133
Guimarães, M. M., Alencar, S. H. P., Vieira, S. L. A., & Corradi, W. J. B., 2006, A&A , 457, 581
Haisch, K. E., Jr., Greene, T. P., Barsony, M., & Stahler, S. W., 2004, AJ, 127, 1747
Hanson, M.M., 2003, ApJ , 597, 957
Harju, J., Lehtinen, K., Booth, R. S., & Zinchenko, I., 1998, A&AS , 132, 211
Heggie, D. C., 1975, MNRAS , 173, 729
Herbig, G. H., 1960, ApJS , 4, 337
Herbig, G. H., 1962, Adv. Astr. Astrophys., 1, 47
Herbig, G. H., 1989, in Proc. ESO Workshop on Low Mass Star Formation and Pre-Main Sequence Objects, ed. B. Reipurth (Garching: ESO), 233
Herbig, G. H., 2008, AJ, 135, 637
Herbig, G. H., & Bell, K., R., 1988, Lick Obser. Bulletin, 1111
Herbig, G. H., & Terndrup, D. M., 1986, ApJ , 307, 609
Herrero, A., Corral, L.J., Villamariz, M.R., & Martín, E.L., 1999, A&A , 348, 542
Herrero, A., Puls, J., & Najarro, F., 2002, A&A , 396, 949
Higgs, L. A., Landecker, T. L., Israel, F. P. & Bally, J., 1991, J. R. Astron. Soc. Can., 85, 24
Hillenbrand, L. A., 1997, AJ, 113, 1733
Hillenbrand, L. A., & Hartmann, L. W., 1998, ApJ , 492, 540
Hills, J. G., 1975, AJ, 80, 809
Hoffmeister C., Richter G., Wenzel W., 1985, Variable Stars, Springer-Verlag, p.253

Hubber, D. A., & Whitworth, A. P., 2005, A&A , 437, 113
Hutchings, J. B., 1981, PASP , 93, 50
Johnson H.L. & Morgan W.W., 1954, ApJ 119, 344
Jones, B. F., & Walker, M. F., 1988, AJ, 95, 1755
Joy, A.H., 1945, ApJ , 102, 168
Kiminki, D.C., Kobulnicky, A., Kinemuchi, K., Irwin, J.S., Fryer, C.L., Berrington, R.C., Uzpen, B., Monson, A.J., Pierce, M.J., & Woosley, S.E., 2007, ApJ , 664, 1120
Knödlseder, J., 2000, A&A , 360, 539
Knödlseder, J., Cerviño, M., Le Duigou, J.-M., Meynet, G., Schaerer, D., & von Ballmoos, P., 2002, A&A , 390, 945
Köhler, R., Petr-Gotzens, M. G., McCaughrean, M. J., Bouvier, J., Duchêne, G., Quirrenbach, A., & Zinnecker, H., 2006, A&A , 458, 461
Kroupa, P., 1995a, MNRAS , 277, 1491
Kroupa, P., 1995b, MNRAS , 277, 1507
Kroupa, P., 2000, NewA, 4, 615
Kroupa, P., Aarseth, S., & Hurley, J., 2001, MNRAS , 321, 699
Kroupa, P., Bouvier, J., Duchêne, G., Moraux, E., 2003, MNRAS , 346, 354
Kroupa, P., & Bouvier, J., 2003, MNRAS , 346, 369
Kroupa, P., Petr, M. G., & McCauhrean, M. J., 1999, NewA, 4, 495
Kuchar, T. A., & Clark, F. O., 1997, ApJ , 488, 224
Kurtz, D. W., & Marang, F., 1995, Delta Scuti Star Newsletter, 8, 2
Lada, C. J., 1987, Star Forming Regions, IAUS, No. 115, 1
Lada, C. J., 2006, ApJ , 640, L63
Lada, C. J. & Wilking, B.A., 1984, ApJ , 287, 610
Lafler, J., & Kinman T.D. 1965, ApJS , 11, 216
Leinert, C., Zinnecker, H., Weitzel, N., et al., 1993, A&A , 278, 129
Lima, G. H. R. A., 2002, Dissertação de Mestrado, DF-ICEx-UFMG
Lockman, F. J., 1989, ApJS , 71, 469
Lorenzetti, D., Giannini, T., Calzoletti, L., Puccetti, S., Antoniucci, S., Arkharov, A. A., Di Paola, A., Larionov, V. M., & Nisini, B., 2006, A&A , 453, 579
Lucas, P. W., Roche, P. F., & Tamura, M., 2005, MNRAS , 361, 211
Luhman, K. L., Stauffer, J. R., Muench, A. A., Rieke, G. H., Lada, E. A., Bouvier, J., & Lada, C., 2003, ApJ , 593, 1093
Luhman, K. L., Whitney, B. A., Meade, M. R., Babler, B. L., Indebetouw, R., Bracker, S., & Churchwell, E. B., 2006, ApJ , 647, 1180
Massey, P., & Thompson, A.B., 1991, AJ, 101, 1408
Mathieu, R. D., 1994, ARA&A, 32, 465
Mathieu, R. D., Baraffe, I., Simon, M., Stassun, K. G., & White, R., 2007, Protostars and Planets V, p. 411
Meeus, G., & McCaughrean, M. J., 2005, Astron. Nachr., 326, 977
Moffat, A.F.J., Drissen, L., Shara, M.M., 1994, ApJ , 436, 183
Molinaris, S., Brand, J., Cesaroni, R., & Palla, F., 1996, A&A , 308, 573
Morgan W.W., Meinel A.B. & Johnson H.M., 1954, ApJ, 120, 506
Münch L. & Morgan W.W., 1953, ApJ, 118, 161
Nazé, Y., De Becker, M., Rauw, G., & Barbieri, C., 2008, A&A , 483, 543

Neuhäuser, R., Mugrauer, M., Seifahrt, A., Schmidt, T. O. B., & Vogt, N., 2008, A&A , 484, 281
O'Dell, C. R., 2001, AJ, 122, 2662
O'Dell, C. R., & Wong, K., 1996, AJ, 111, 846
Odenwald, S. F., 1989, AJ, 97, 801
Padgett, D. L., Strom, S. E., & Ghez, A., 1997, ApJ , 477, 705
Palla, F., Brand, J., Cesaroni, R., Comoretto, G., & Felli, M., 1991, A&A , 246, 249
Parsamian, E. S., Mujica, R., & Corral, L., 2002, Astrophysics, 45, 393
Parthasarathy, M., Jain, S. K., & Bhatt, H. C., 1992, A&A , 266, 202
Patience, J., Ghez, A. M., Reid, I. N., & Matthews, K., 2002, AJ, 123, 1570
Petr, M. G., Coudé du Foresto, V., Beckwithm S., Richichi, A., & McCaughrean, M. J., 1998, ApJ , 500, 825
Pojmanski, G., 1997, Acta Astronomica, 47, 467
Prosser, C. F., Stauffer, J. R., Hartmann, L., Soderblom, D. R., Jones, B. F., Werner, M. W., & McCaughrean, M. J., 1994, ApJ , 421, 517
Ratzka, T., Köhler, R., & Leinert, Ch., 2005, A&A , 437, 611
Rebull, L. M., 2001, AJ, 121, 1676
Reddish V.C., Lawrence L.C. & Pratt N.M., 1966, Publ. R. Obser. Edinburgh, 5, 111
Reipurth, B., 2000, AJ, 120, 3177
Reipurth, B., & Zinnecker, H., 1993, A&A , 278, 81
Reipurth, B., & Clarke, C. J., 2001, AJ, 122, 432
Reipurth, B., Guimarães, M. M., Connelley, M. S., & Bally, J., 2007, AJ, 134, 2272
Rutman J., 1978, Proc. IEEE, **66**, 1048
Scalise, E., Jr., Rodriguez, L. F., & Mendonza-Torres, E., 1989, A&A , 221, 105
Schneider, N., Bontemps, S., Simon, R., Jakob, H., Motte, F., Miller, M., Kramer, C., & Stutzki, J., 2006, A&A , 458, 855
Scholz, R.-D., Meusinger, H., Irwin, M. 1997, A&A, 325, 457
Schulte D.H., 1956a, ApJ, 123, 250
Schulte D.H., 1956b, ApJ, 124, 530
Schulte D.H., 1958, ApJ, 128, 41
Schutte, A. J., van der Walt, D. J., Gaylard, M. J., & MacLeod, G. C., 1993, MNRAS , 1993, 261, 783
Setia Gunawan, D. Y. A., De Bruyn, A. G., vann der Hucht, K. A., & Williams, P. M., 2003, ApJS , 149, 123
Sicilia-Aguilar, A., et al., achar resto, 2005, AJ, 129, 363
Simon, M., Ghez, A. M., Leinert, Ch., Cassar, L., Chen, W. P., Howell, R. R., Jameson, R. F., Matthews, K., Neugebauer, G., & Richichi, A., 1995, ApJ , 443, 625
Simon, M., Close, L. M., & Beck, T. L., 1999, AJ, 117, 1375
Simonetti J.H., Cordes J.M., Heeschen D.S., 1985, ApJ , 296, 46
Skrutskie, M. F., Cutri, R. M., Stiening, R., Weinberg, M. D., Schenieder, S., Carpenter, J. M., Beuchman, C., Capps, R., Chester, T., et al., 2006, AJ, 131, 1163
Sridharan T. K., Beuther, H., Schilke, P., Menten, K. M., & Wyrowski, F., 2002, ApJ , 566, 931
Stassun, K. G., Mathieu, R. D., Mazeh, T., & Vrba, F. J., 1999, AJ, 117, 2941
Stassun, K. G., van den Berg, M., Feigelson, E., & Flaccomio, E., 2006, ApJ , 649, 914
Stassun, K. G., Mathieu, R. D., Cargile, P. A., Aarnio, A. N., Stemple, E., & Geller, A., 2008, Nature, 453, 1079

Sterzik, M. F., & Durisen, R. H., 1998, A&A , 339, 95
Sterzik, M. F., & Durisen, R. H., 2003, A&A , 400, 1031
Sterzik, M. F., Durisen, R. H., & Zinnecker, H., 2003, A&A , 411, 91
Taylor, A. R., Gross, W. M., Coleman, P. H., van Leeuwen, J., & Wallace, B. J., 1996, ApJS , 107, 239
Taylor, A. R., Gibson, S. J., Peracaula, M., Martin, P. G., Landecker, T. L., et al.., 2003, AJ, 125, 3145
Te Lintel Hekkert, P., 1991, A&A , 248, 209
Torres-Dodgen A.V., Tapia M. & Carroll M., 1991, MNRAS, 249, 1
Umbreit, S., Burkert, A., Henning, T., Mikkola, S., & Spurzem, R., 2005, ApJ , 623, 940
Van Loo, S., Blomme, R., Dougherty, S.M., & Runacres, M.C., 2008, A&A , 483, 585
Vink, J.S., Drew, J.E., Steeghs, D., Wright, N.J., Martin, E.L., Gänsicke, B.T., Greimel,R., & Drake, J., 2008, MNRAS , 387, 308
Voelcker, K. P. J., 1974, unpublished PhD thesis, Univ. Heidelberg
Wendker, H. J., 1984, A&AS , 58, 291
Wendker, H. J., Higgs, L. A., & Landecker, T. L., 1991, A&A , 241, 55
Wendker, H. J., Higgs, L. A., & Landecker, T. L., 1996, Astro. Nachr., 317, 35
Westerhout, G., 1958, Bull. Astron. Inst. Netherlands, 14, 215
Williams, S. J., Fuller, G. A., & Sridharan, T. K., 2004, A&A , 417, 115